PERFORMANCE AND FIRST DEPLOYMENT OF NOVEL 3D NUCLEAR RECOIL DETECTORS

A DISSERTATION SUBMITTED TO THE GRADUATE DIVISION OF THE
UNIVERSITY OF HAWAI‘I AT MĀNOA IN PARTIAL FULFILLMENT OF THE REQUIREMENTS FOR THE DEGREE OF

DOCTOR OF PHILOSOPHY

IN

PHYSICS

DECEMBER 2018

By

Michael T. Hedges

Dissertation Committee:

Sven Vahsen, Chairperson
Thomas E. Browder
Jason Kumar
Jelena Maricic
R. Brent Tully

ACKNOWLEDGMENTS

First and foremost, I wrote this dissertation using “we” instead of “I.” This is for the simple reason that there is no way I could have completed this without the countless insights and patience of my colleagues in Hawaii and my BEAST II colleagues during Phase 1. I would especially like to recognize my advisor, Sven Vahsen, as being instrumentally helpful during the entirety of my time as his student. His insights, extreme patience, and his willingness to make himself available for me in addition to his other students have been nothing short of extraordinary. Last but not least, he took a chance on me and took me as one of his graduate students, and for that, I thank him.

I would also like to acknowledge my endless list of amazing friends and family for their limitless support and encouragement. You all never doubted I would make it this far, even when I doubted myself.

And finally, I wish to express my deepest appreciation and thanks to Jackie for a depth of love and support I could have never imagined to be true if not for you. Thank you.

ABSTRACT

We present the performance and first deployment of a system of Time Projection Chambers (TPCs) using GEMs and pixel readouts for the purpose of providing 3D charge measurements of neutron recoils during the Phase 1 beam commissioning of SuperKEKB.

We find that the high-definition 3D images of ionization clouds provided by the TPCs enable 3D vector tracking of nuclear recoils, nuclear recoil species identification, and excellent electron background rejection for recoil energies down to 50 keVr, i.e. at energies relevant to WIMP dark matter searches. These existing detectors thus represent a stepping stone towards larger detectors fully optimized for directional dark matter searches.

In analyzing the neutron recoils at SuperKEKB, we find that measured rates of detected neutron events created by off-orbit beam particles, due to Touschek and beam-gas scattering, are underestimated in the High Energy Ring (HER) simulations by as much as an order of magnitude. In the Low Energy Ring (LER) simulations, we find that the simulations overestimate the measured rates in the horizontal plane of the beam, whereas the LER beam-background simulations are accurate in the vertical plane of the beam. Furthermore, the vector tracking capability of the detectors allows us to separate the neutron flux into primary neutrons from the beam pipe, and reflected neutrons originating from larger radii. We find that the experimentally measured fractional composition of reflected events is in agreement with the simulated predictions in the horizontal plane at a value of 25% of events. However, we find disagreement with simulation at a significance of 2.44σ in the vertical plane, where we observe 50% of the events are reflected, prompting us to recommend further and more detailed future analyses with more experimental and simulated data.

Finally, we present a novel analysis method for decoupling beam-gas and Touschek background processes using full 3D vector information of nuclear recoils by utilizing a fit of fractional composition of background templates to detected recoil rates along the angle of the beam-line axis, θ. Using this method, we find agreement, within errors, with the results from the traditional heuristic method. This heuristic method traditionally requires time-consuming, dedicated experimental runs while varying accelerator parameters. While the results of this novel analysis are limited by significant statistical uncertainties, it has the potential to be validated by future experiments. If validated, this method can provide detailed decoupling analyses of beam-backgrounds that can be done symbiotically in later phases of Belle II operation, even with a single TPC, without the need for dedicated experimental runs.

TABLE OF CONTENTS

Acknowledgments . . . . **ii**

Abstract . . . . **iii**

List of Tables . . . . **vii**

List of Figures . . . . **x**

1 Introduction **1**

2 Physics of Nuclear Recoils **2**

2.1 Interactions of recoil nuclei with matter 2

2.2 Energy deposition of nuclear recoils in matter 3

2.2.1 Radiative losses 4

2.2.2 Bethe formulation 6

2.3 SRIM 9

2.3.1 LSS formulation 10

3 Nuclear recoils from fast neutrons **11**

3.1 The neutron 11

3.2 Interaction of fast neutrons with matter 12

4 Nuclear recoils from Dark Matter **16**

4.1 Recoil nuclei from dark matter 16

4.2 Recoil nuclei from dark matter 18

4.2.1 Expected recoil signal of particulate dark matter 18

5 BEAST µTPCs **19**

5.1 Principle of operation 19

5.2 Track fitting 22

5.3 Energy calibration 25

5.3.1 Pixel chip calibration 25

5.3.2 Measurement of GEM effective gain 25

5.4 Background rejection 45

5.5 Directionality 68

5.5.1 Axial directionality 68

5.5.2 Head/tail recognition 69

6 Analysis of fast neutron backgrounds at SuperKEKB **76**

6.1 Introduction 76

6.2 Single-beam loss processes 79

6.2.1 Beam-gas losses 79

6.2.2 Touschek losses 81

6.2.3 Synchrotron radiation 82

6.3 Neutron production from beam backgrounds 83

6.3.1 Analysis of fast neutrons at SuperKEKB 84

6.3.2 Simulation of BEAST II Phase 1 TPCs 86

6.4 Simulation reweighting procedure 86

6.5 Event selections 87

6.6 Experimental runs for fast neutron analysis 89

6.7 Nuclear recoil energy spectra 90

6.8 Analysis of fast neutron rates versus beam size 98

6.9 Directional analysis of fast neutron backgrounds 103

6.10 Conclusions 112

LIST OF TABLES

3.1 Ratio of maximum energy transferred of recoil nucleus to neutron energy for various isotopes of interest [12]. 15

5.1 Fit parameters obtained from fitting detected charge in calibration alpha events in TPC H, shown in 5.6, to a line. 28

5.2 Fit parameters obtained from fitting detected charge in calibration alpha events in TPC V, shown in 5.7, to a line. 29

5.3 Parameter values returned by the fourth order polynomial fit shown in Figure 5.13. Here c_i corresponds to the coefficient of the i^{th} power of x in the polynomial function.
38

5.4 Parameter values returned by the fifth order polynomial fit shown in Figure 5.16. Here c_i corresponds to the coefficient of the i^{th} power of x in the polynomial function.
41

5.5 Table of values of corrected dQ/dx in TPC H, TPC V, and Monte Carlo simulation and resulting conversion factors. A mean value of dQ/dx obtained from averaging the dQ/dx of each of the two ^{210}Po calibration sources in Monte Carlo, TPC H, and TPC V, shown in Figure 5.17, is calculated separately and shown in the second column of the table. The third column shows the ratio of the obtained mean in each TPC to the mean calculated from the Monte Carlo simulation. This ratio is then used as a multiplicative correction to the detected recoil energies presented in Chapter 6.
42

6.1 SuperKEKB design parameters [28]. 78

6.2 BEAST II Phase 1 detector system names, detector types, and unique measurement or capability provided of each system. 84

6.3 Machine parameters used for the BEAST II Phase 1 Monte Carlo simulation data [25]. 87

6.4 Full event selections to be used for selecting signal events, along with each selection's cumulative efficiency in MC Touschek, MC beam-gas, and experimental data in TPC H. 88

6.5 Full event selections to be used for selecting signal events, along with each selection's cumulative efficiency in MC Touschek, MC beam-gas, and experimental data in TPC V. 88

6.6 Number of total events detected compared to the Monte Carlo prediction for the HER run. 89

6.7 Number of total events detected compared to the Monte Carlo prediction for the LER run. 89

6.8 Results of fitting the recoil energy spectra for TPCs 3 and 4 for Monte Carlo and experimental data for the LER runs. 90

6.9 Table of values of corrected dQ/dx in TPC H, TPC V, and Monte Carlo simulation and resulting conversion factors. A mean value of dQ/dx, obtained from averaging the dQ/dx of each of the two ^{210}Po calibration sources in Monte Carlo, TPC H, and TPC V, shown in Figure 5.17, is calculated separately and shown in the second column of the table. The third column shows the ratio of the obtained mean in each TPC to the mean calculated from the Monte Carlo simulation. This ratio is then used as a multiplicative correction to the detected recoil energies presented in Chapter 6. 93

6.10 Results of fitting the recoil energy spectra for TPCs H and V for Monte Carlo and experimental data for the HER run. 97

6.11 Calculated yield from the measured rates of nuclear recoils from beam-gas and Touschek backgrounds shown in Figure 6.13 for both experimental data and Monte Carlo in each TPC. 99

6.12 Fraction of outgoing and incoming events predicted in simulation and from fitting yields to simulated and experimental data in TPC H. N_{out} corresponds to the fraction of outgoing events and N_{in} corresponds to the fraction of incoming events. Errors on the truth values correspond to the square-root of the number of events, whereas remaining errors are the errors obtained from the log-likelihood fit.
107

6.13 Fraction of outgoing and incoming events predicted in simulation and from fitting yields to simulated and experimental data in TPC V. N_{out} corresponds to the fraction of outgoing events and N_{in} corresponds to the fraction of incoming events. Errors on the truth values correspond to the square-root of the number of events, whereas remaining errors are the errors obtained from the log-likelihood fit.
107

6.14 Calculated yield from the fits of $cos\theta$ both TPCs, as shown in Figures 6.16 and 6.17, compared to the results of the Touschek and beam-gas backgrounds measured in each TPC using the heuristic method in Sectin 6.8. N_{bg} corresponds to the fractional composition of Touschek events, and N_T corresponds to the fractional composition of beam-gas events. The uncertainties are those returned by the fitter. We note that in the $cos\theta$ analysis, the total yields have an upper limit of the number of detected events in the data samples, whereas no such constraint was imposed on the results in the heuristic analysis.
111

LIST OF FIGURES

2.1 Stopping power for positive muons in copper over nine orders of magnitude in momentum, corresponding to 12 orders of magnitude in kinetic energy, as shown by the Particle Data Group [1]. 5

2.2 Example Bragg curve: Energy loss of alpha particles of energy 5.49 MeV in air. 8

3.1 Feynman diagram for beta decay of a free neutron 12

3.2 Total neutron interaction cross section for He^4 versus neutron energy. The cross section is to first order exclusively elastic. 13

3.3 Diagrams illustrating the lab frame (left) and center-of-mass frame (right) of a neutron scattering elastically with a target nucleus. 14

4.1 Simplified diagram of Dark Matter (DM) interactions with Standard Model (SM) particles. The circle at the center represents unknown processes that would mediate such interactions 17

5.1 One of the 5 × 5 cm GEMs used to amplify charge in the TPCs. 20

5.2 Circuit diagram for the TPC high voltage system consisting of a drift volume with a field cage and the GEM amplification region [18]. 21

5.3 Top-down view of the ATLAS FE-I4 pixel chip layout. The origin for row and column number is at the top left, with column number increasing to the right and row number increasing downwards. 23

5.4 single column 24

5.5 A photo of the inside of a TPC showing the ^{210}Po calibration sources. The white containers with the yellow centers in the upper half of the photo hold source holders. The source holder at the top of the photo is the "top" source—the source at largest drift distance—and the source holder towards the bottom of the photo, closest to the green wires, is the "bottom" source—the source at smallest drift distance. 30

5.6 Detected charge of alpha particle calibration events in TPC H versus time. The dark blue triangles in each plot correspond to the bottom ^{210}Po source, corresponding to the source at smaller drift distance, and the light blue circles correspond to the top calibration source at larger drift distance. The fitted lines represent the change of energy over time of events from each internal calibration source. The fit results are shown in Table 5.1. 31

5.7 Detected charge of alpha particle calibration events in TPC V versus time. The dark green triangles in each plot correspond to the bottom ^{210}Po source, corresponding to the source at smaller drift distance, and the light green circles correspond to the top calibration source at larger drift distance. The fitted lines represent the change of energy over time of events from each internal calibration source. The fit results are shown in Table 5.2. 32

5.8 Histograms of the reconstructed detected charge divided by track length before calibrations for events from internal ^{210}Po calibration alpha sources in experimental and Monte Carlo data before application of any energy-scale corrections. The vertical axis shows the total number of events from both sources, normalized to 1, for two TPCs and Monte Carlo separately. 33

5.9 TOT distributions of simulated events from the top and bottom calibration sources in a TPC at a gain of 1500. 34

5.10 Ratio of reconstructed to true recoil energy versus the number of pixels with saturated TOT in simulated helium recoils. 35

5.11 Ratio of reconstructed to true recoil energy versus the number of pixels with saturated TOT in simulated carbon and oxygen recoils. 36

5.12 Ratio of reconstructed to true recoil energy versus the number of pixels with saturated TOT in all simulated recoils. 37

5.13 Ratio of reconstructed to true energy versus fraction of saturated pixels per event in all simulated recoils, binned and fit to a fourth order polynomial. . . 38

5.14 Histograms of the reconstructed detected charge divided by track length after correcting for pixel saturation via the fitted function shown in Figure 5.13, for events from internal ^{210}Po calibration alpha sources in experimental and Monte Carlo data. The vertical axis shows the total number of events from both sources, normalized to 1, for two TPCs, and Monte Carlo separately. . 39

5.15 Ratio of reconstructed to true recoil versus average TOT per pixel in in all simulated recoils. 40

5.16 Ratio of reconstructed to true energy versus the average TOT in a single pixel per event binned and fit to a fifth order polynomial. 41

5.17 Histograms of the reconstructed detected charge divided by track length after correcting for pixel saturation and charge below the pixel threshold, via the fitted unction shown in Figures 5.13 and 5.16, respectively, for events from internal ^{210}Po calibration alpha sources in experimental and Monte Carlo data. The vertical axis shows the total number of events from both sources, normalized to 1, for TPC H, TPC V, and Monte Carlo separately. 43

5.18 Histograms of the reconstructed energy compared to the true energy of helium recoils in simulated data. The line of darkest color corresponds to the corrected energy values, and the line of lightest color corresponds to the true energy. The last shade corresponds to the uncorrected energy values. 44

5.19 Recorded edge code in events in Monte Carlo signal and background data. An edge code of zero corresponds to the applied fiducialization selection, indicated by the vertical line. All other codes represent one or more edges of the pixel chip triggered in an event and are vetoed. 46

5.20 TPC recoil charge versus recoil length for fiducially selected events in TPCs H and V, for both Monte Carlo and experimental data, combined. This includes applying the gain correction factors in Table 5.5 to each TPC. The blue, orange, and green filled circles represent helium recoils, carbon/oxygen recoils, and proton backgrounds in Monte Carlo, respectively. The open black circles represent the events in experimental data that pass the fiducialization selection. 48

5.21 TPC recoil energy versus recoil length, as shown in Figure 5.20, with a focus on low energy and short length events. 49

5.22 TPC recoil charge versus recoil length for fiducially selected events in TPCs H and V, for both Monte Carlo and experimental data, combined. This includes applying the gain correction factors in Table 5.5 to each TPC and an additional correction factor of 1.2 in order to align the helium bands in Monte Carlo and experimental data. The blue, orange, and green filled circles represent helium recoils, carbon/oxygen recoils, and proton backgrounds in Monte Carlo, respectively. The open black circles represent the events in experimental data that pass the fiducialization selection. 50

5.23 Corrected TPC recoil energy versus recoil length, as shown in Figure 5.22, with a focus on low energy and short length events. 51

5.24 Efficiency versus purity of various values for the lower bound on the dE/dx selection for helium recoils. Each point corresponds to the purity and efficiency of nuclear recoils for a given minimum dE/dx (indicated by color) and above a minimum energy. The optimal selection corresponds to dE/dx greater than 20.0 eV/µm and detected recoil energy greater than 20 keV. 53

5.25 A tighter view of Figure 5.24 near the point of maximal efficiency and purity for the lower bound on the dE/dx selection for nuclear recoils. 54

5.26 Efficiency versus energy of various values for the lower bound on the dE/dx selection for helium recoils. Each point corresponds to the purity and efficiency of nuclear recoils for a given minimum dE/dx (indicated by color) and above a minimum energy. The optimal selection corresponds to dE/dx greater than 20.0 eV/µm and detected recoil energy greater than 20 keV. 55

5.27 Efficiency versus energy of various values for the lower bound on the dE/dx selection for helium recoils, as shown in Figure 5.26, with axes limits to focus in where the efficiency gets nearest to unity. 56

5.28 Purity versus energy of various values for the lower bound on the dE/dx selection for nuclear recoils. Each point corresponds to the purity and efficiency of helium recoils for a given minimum dE/dx (indicated by color) and above a minimum energy. The optimal selection corresponds to dE/dx greater than 20.0 eV/µm and detected recoil energy greater than 20 keV. 57

5.29 Efficiency versus energy of various values for the lower bound on the dE/dx selection for nuclear recoils, as shown in Figure 5.28, with axes limits to focus in where the efficiency gets nearest to unity. 58

5.30 Energy versus length for all events that pass the fiducialization selection in TPC H. The green line shows the boundary of a selection of $dE/dx > 0.04$ keV/µm. 59

5.31 Energy versus length for all events that pass the fiducialization selection in TPC V. The green line shows the boundary of a selection of $dE/dx > 0.04$ keV/µm. 60

5.32 Efficiency versus energy of various values for the upper bound on the dE/dx selection for helium recoils. Each point corresponds to the purity and efficiency of helium recoils for a given minimum dE/dx (indicated by color) and above a minimum energy. The optimal selection corresponds to dE/dx less than 162 eV/µm and detected recoil energy greater than 28 keV. 62

5.33 Purity versus energy of various values for the upper bound on the dE/dx selection for helium recoils. Each point corresponds to the purity and efficiency of helium recoils for a given minimum dE/dx (indicated by color) and above a minimum energy. The optimal selection corresponds to dE/dx less than 162 eV/µm and detected recoil energy greater than 28 keV. 63

5.34 Efficiency versus purity of various values for the upper bound on the dE/dx selection for helium recoils. Each point corresponds to the purity and efficiency of helium recoils for a given maximum dE/dx (indicated by color) and above a minimum energy. The optimal selection corresponds to dE/dx less than 162 eV/µm and detected recoil energy greater than 28 keV. 64

5.35 A zero-suppressed view of Figure 5.34 near the point of maximal efficiency and purity for the upper bound on the dE/dx selection for helium recoils. . . 65

5.36 Efficiency of TPC neutron selections described in Section 5.4 versus detected energy in experimental data. Efficiency of 50% occurs at approximately 30 keV. The unequal spacing between adjacent points is due to nonuniform bin sizing so that all bins have relatively similar statistical uncertainties. There are no bins with zero entries. 66

5.37 Fractional energy resolution versus energy in helium recoils. 67

5.38 Angular resolution measured with true values in simulation and using the split-track method in experimental data versus track length. 69

5.39 Angular resolution measured with true values in simulation and using the split-track method in experimental data versus detected energy. 70

5.40 Fractional charge in the true head of helium events (green) and its mirrored distribution in TPC H. 72

5.41 Fractional charge in the true head of carbon and oxygen events in TPC H. . 73

5.42 Head charge fraction in helium recoils (blue) and combining carbon and oxygen recoils (pink) versus track length in TPC H. 74

5.43 Head charge fraction in helium recoils (blue) and combining carbon and oxygen recoils (pink) versus detected recoil energy in TPC H. 75

6.1 Schematic drawing of the SuperKEKB/Belle II facility [27]. 77

6.2 Graphic demonstrating a simplified model of beam loss due to beam-gas scattering. A single beam particle (green), originally contained within the beam orbit—represented by the ellipse—scatters with a residual gas atom (blue) after the atom desorbs from the inner beam-pipe surface. After the scattering, the beam particle is lost from the beam orbit and will eventually produce showers that leave the beam-pipe. 79

6.3 Graphic demonstrating a simplified model of beam loss due to Touschek scattering. Two particles within the same beam bunch scatter off of each other, causing one to leave the beam orbit and eventually producing showers that leave the beam-pipe volume. 81

6.4 Illustration of a synchrotron radiation created from an electron beam traversing through a bending dipole magnet. 83

6.5 A photograph (top) of, with a CAD rendering (bottom) from the same perspective of the BEAST II Phase 1 detector system [25]. 85

6.6 Detected energy distribution for nuclear recoil candidates in TPC H for the LER run. The blue and orange bar histograms show the expectations for Touschek and beam-gas (Coulomb and bremsstrahlung) contributions obtained via the reweighted simulation, respectively, and the black points show the measured values in experimental data. The distributions are fit to a decaying exponential. The dashed lines show the returned fit functions for the Monte Carlo and experimental data. The parameters of the fit are shown in Table 6.8. 91

6.7 Detected energy distribution for nuclear recoil candidates in TPC V for the LER run. The blue and orange bar histograms show the expectations for Touschek and beam-gas (Coulomb and bremsstrahlung) contributions obtained via the reweighted simulation, respectively, and the black points show the measured values in experimental data. The distributions are fit to a decaying exponential. The dashed lines show the returned fit functions for the Monte Carlo and experimental data. The parameters of the fit are shown in Table 6.8. 92

6.8 Histograms of the reconstructed detected charge divided by track length during the time of the HER run, after correcting for pixel saturation and charge below the pixel threshold, shown in Figures 5.13 and 5.16, respectively, for events from internal ^{210}Po calibration alpha sources in experimental and Monte Carlo data. The vertical axis shows the total number of events from both sources, normalized to 1, for TPC H, TPC V, and Monte Carlo separately. The mean value of each peak is then used as an input in calculating the correction factor. 94

6.9 Detected energy distribution for nuclear recoil candidates in TPC H for the HER run. The blue and orange bar histograms show the expectations for Touschek and beam-gas (Coulomb and bremsstrahlung) contributions obtained via the reweighted simulation, respectively, and the black points show the measured values in experimental data. The distributions are fit to a decaying exponential. The dashed lines show the returned fit functions for the Monte Carlo and experimental data. The parameters of the fit are shown in Table 6.10. 95

6.10 Detected energy distribution for nuclear recoil candidates in TPC V for the HER run. The blue and orange bar histograms show the expectations for Touschek and beam-gas (Coulomb and bremsstrahlung) contributions obtained via the reweighted simulation, respectively, and the black points show the measured values in experimental data. The distributions are fit to a decaying exponential. The dashed lines show the returned fit functions for the Monte Carlo and experimental data. The parameters of the fit are shown in Table 6.10. 96

6.11 Plot of the LER beam-gas and Touschek fast neutron rates in TPC H. The dark pink circles correspond to the results from experimental data, and the light pink triangles correspond to the results from Monte Carlo. 100

6.12 Plot of the LER beam-gas and Touschek fast neutron rates in TPC V. The light orange circles correspond to the results from experimental data, and the dark orange triangles correspond to the results from Monte Carlo. 101

6.13 Plot of the LER beam-gas and Touschek fast neutron rates in the TPC detector system. The blue circles correspond to the results from experimental data, and the blue triangles correspond to the results from Monte Carlo. . . 102

6.14 Distribution of fractional charge for simulated (top) and experimental (bottom) data in TPC H. The black points correspond to the HCF distribution of the reconstructed events in simulated and experimental data with an assumed outgoing-directionality that are within the ϕ acceptance. The blue and orange bars correspond to the yields from fitted templates of the true HCF for outgoing and incoming recoils within the ϕ acceptance, as given by the simulated data. The green line represents the sum of the two templates and the corresponding number of events of each bin. 105

6.15 Distribution of fractional charge for true incoming and outgoing recoils in the Monte Carlo simulation of TPC V (top), which are in turn used as templates to obtain fractional yield in TPC H experimental data (bottom). 106

6.16 (Top) Distribution of $cos\theta$ in experimental data in TPC H (black points) with fractional yields of Touschek (blue) and beam-gas (orange) events in simulated data. The green line corresponds to the sum of the templates. This fit uses the TFractionFitter class in order to account for Poisson statistical fluctuations in individual bins in the histogram templates [37]. The bottom plot shows the normalized templates used for fitting to the black points by the TFractionFitter algorithm. 109

6.17 (Top) Distribution of $cos\theta$ in experimental data in TPC V (black points) with fractional yields of Touschek (blue) and beam-gas (orange) events in simulated data. The green line corresponds to the sum of the templates. This fit uses the TFractionFitter class in order to account for Poisson statistical fluctuations in individual bins in the histogram templates [37]. The bottom plot shows the normalized templates used for fitting to the black points by the TFractionFitter algorithm. 110

CHAPTER 1
INTRODUCTION

Detection of electrically neutral particles remains a vital and rich subject in high-energy physics research. One promising avenue with potential of broad application is detection and measurement of neutral particles via scattering with atomic nuclei, producing nuclear recoils. The ultimate goal of this endeavor is full 3-dimensional and high-precision measurement and analysis of these recoil nuclei. This dissertation presents the introductory physics of nuclear recoil production and the stopping of recoil nuclei in matter and subsequently deposited energy into an absorber material. This is then discussed within the context of neutron and dark matter detection using nuclear recoils.

Furthermore, we present the performance of a system of novel Time Projection Chambers (TPCs) using GEMs and pixel readouts for detecting nuclear recoils. We then present the first deployment of these TPCs for Phase 1 of SuperKEKB commissioning, therein providing directional and energy measurements of fast neutron backgrounds produced by beam-loss processes. We conclude with our findings and comparisons between measurements and the predictions from dedicated simulations, thereby providing direct measurement of the accuracy of the beam-loss simulations.

CHAPTER 2
PHYSICS OF NUCLEAR RECOILS

A nuclear recoil is the resulting product of an atomic interaction in which energy from an incoming particle is transferred directly to the nucleus. In general, the description of the maximum energy transfer of a particle with mass M to a particle of mass m is expressed as [1]:

$$W_{max} = \frac{2mc^2\beta^2\gamma^2}{1 + \gamma m/M + (m/M)^2} \tag{2.1}$$

where:

- c is the speed of light
- $\beta = v/c$, where v is the incoming particle velocity
- $\gamma = \frac{1}{\sqrt{1-\beta^2}}$

This describes the maximum energy that can be transferred to an atomic nucleus as well as the subsequent energy that a recoiling nucleus will exchange with other particles as it travels through material. This chapter discusses the general physics of the interactions of recoil nuclei traversing in matter.

2.1 Interactions of recoil nuclei with matter

Due to their positive charge, recoil nuclei participate in Coulomb interactions with charged particles present in neighboring atoms inside of an absorber material. As such, recoil nuclei can interact with orbital electrons as well as nuclei of absorber atoms.

Given the strength and distance of the coulomb interaction, recoil nuclei interact very strongly with the orbital electrons present in absorber atoms. There are two types of these interactions that can take place. The first type occurs when the energy exchange is large enough that the electron is excited to a higher level energy state but too small to create an ion pair. This process is known as *excitation* [2]. The second type of interaction occurs when the energy transferred to the electron is large enough to free the electron from the atom, creating a free electron and a positive ion, known as an ion pair. This process is known as *ionization* [2]. Each of these processes results in a loss of kinetic energy in the recoil nucleus.

Due to energy and momentum conservation, the maximum energy that can be transferred from a recoil nucleus of mass m and kinetic energy of E to an electron of mass m_e in a single interaction is $4Em_e/m$, given that $m >> m_e$. Considering that the mass of one nucleon is approximately 200 times larger than m_e and m is the sum of all constituent nucleons, each individual interaction between a recoil nucleus and an orbital electron results in a relatively small fraction of energy lost by the nucleus. This requires many such *electronic interactions* to create a significant amount of energy loss.

Secondly, a free nucleus can also scatter with other atomic nuclei in the absorber. The scattering can either be elastic, known as *Rutherford Scattering*, or inelastic. Unlike electron interactions, a single interaction with an atomic nucleus can result in a significant change of both magnitude and direction of the momentum of the recoil nucleus. The resulting effect depends on the energy of the recoil nucleus at the moment of scattering and the mass of the target nucleus. At levels of energy transfer above the binding energy of the nucleus in the target atom, the initial recoil nucleus can free the target nucleus via inelastic scattering, thus creating another free recoil nucleus that traverses through the absorber. At lower energies, elastic scattering is more common than inelastic scattering.

As a recoil nucleus traverses through an absorber, it will undergo many interactions before all of its kinetic energy is deposited into the absorber and the nucleus is stopped. For a given absorber, these interactions will result in specific amount of loss of kinetic energy in a given distance. This represents a rate of energy loss per unit length. This is known as an absorber's *stopping power* and forms the basis of understanding how charged particles, such as recoil nuclei, deposit energy in matter, which is the focus of discussion in the next section.

2.2 Energy deposition of nuclear recoils in matter

The linear stopping power S, also known as *specific energy loss*, for charged particles in an absorber is defined as the differential energy lost by the particle per unit length traveled in the absorber and can be described as:

$$S = -\frac{dE}{dx} \tag{2.2}$$

The total stopping power of an absorber is further categorized by *electronic stopping power* and *nuclear stopping power*, corresponding to the stopping power of absorber on an incoming particle interacting with atomic electrons and nuclei, respectively. There is currently not a single framework for describing the stopping power of particles over all momenta. Instead, a collection of frameworks for specific energy loss are used at various ranges of monenta. The collection of frameworks, in order of decreasing momentum, are the following:

- Radiative losses
- Bethe*
- SRIM†
- LSS

The explicit specific energy loss for muons in copper versus momentum—covering a broad range of momenta to show the regimes corresponding to the aforementioned frameworks—is shown in Figure 2.1 [1]. As can be seen, the applicable framework of specific energy loss of a muon will change as it loses energy. This energy loss will continue until it is stopped or exits the absorber volume. Thus, if a sufficiently energetic particle is traveling through a sufficient amount of absorber material, the specific energy loss of the particle will transition across the boundaries of multiple frameworks. While an arbitrary particle—especially a recoiling nucleus—will, in general, exhibit a different behavior from that of a muon, it may still be necessary to use more than one framework to describe its specific energy loss. For this reason, we will discuss the frameworks in the order they are listed above—in order of decreasing momentum.

2.2.1 Radiative losses

At large momenta, a particle traveling through matter loses energy almost entirely by *radiative processes*. These processes cause energy loss through emission of radiation via deceleration of the particle as it interacts with the coulomb fields generated by atomic electrons. These emission processes include *Bremsstrahlung* and *Cherenkov* radiation. The momentum threshold where radiative losses dominate—known as the *critical momentum*—shown in Figure 2.1 as E_{μ_c}—is defined as the energy where energy loss from radiative effects are equal to all other energy losses. The value of E_{μ_c} varies largely with particle type. However,

*Historically, this has also been referred to as *Bethe-Bloch*. However, this dissertation will use the naming convention presented in the 2018 Particle Data Group report, which uses the single name *Bethe* [1].

†This regime is labeled as *Anderson-Ziegler* by the PDG [1]. However, their discussion does not include charged particles with $Z > 1$, thereby excluding recoil nuclei. The standard for modeling the specific energy loss of these types of particles is the SRIM package [3].

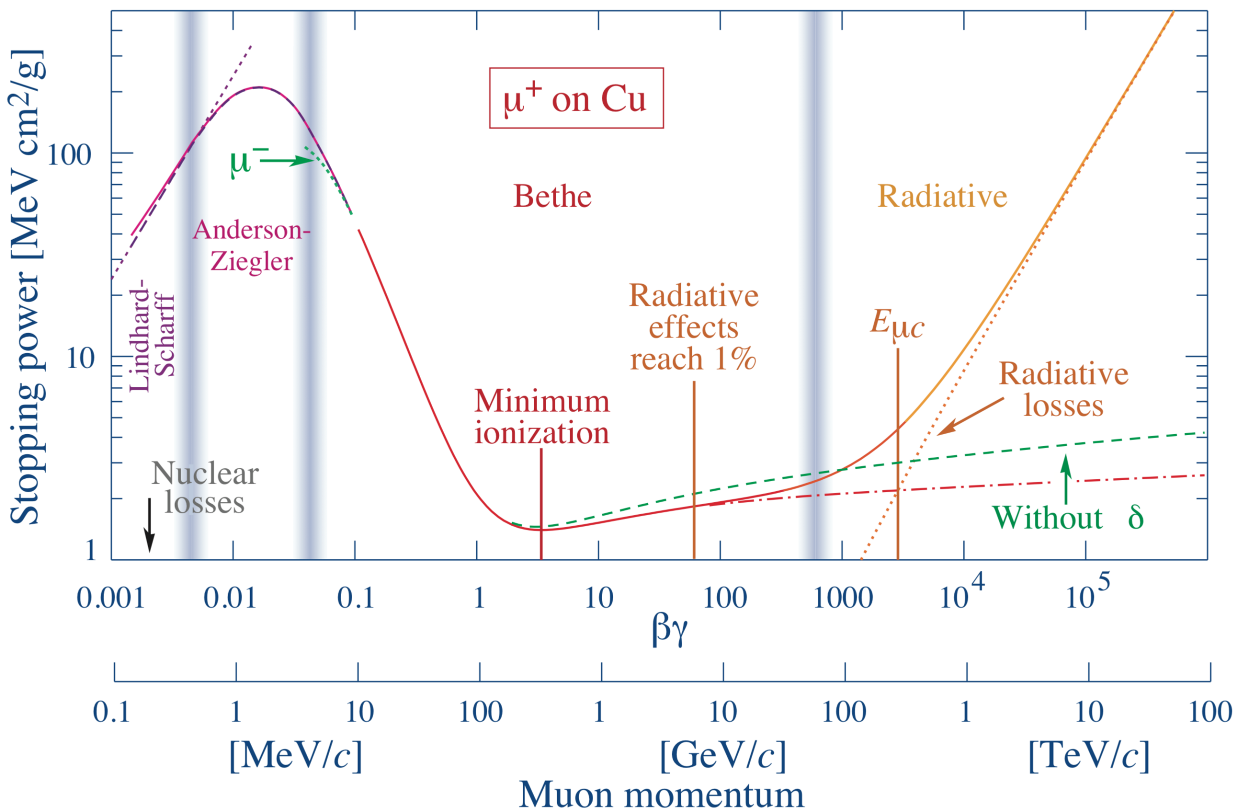

Figure 2.1: Stopping power for positive muons in copper over nine orders of magnitude in momentum, corresponding to 12 orders of magnitude in kinetic energy, as shown by the Particle Data Group [1].

in general the critical momentum occurs at highly relativistic speeds—specifically when the relativistic factor $\beta = v/c \sim 1$. This critical momentum occurs in muons at several hundred GeV/c. The critical momentum rises to much larger values for protons [1] and even larger still for atomic nuclei. Thus, while there is no simple scaling with particle mass [1], particles of larger masses have significantly larger critical momenta. As such, it is exceedingly unlikely that the energy loss of any recoil nucleus can be described by radiative losses.

2.2.2 Bethe formulation

In the region where radiative effects become a sub-dominant—and eventually negligible—contribution to energy loss, the specific energy loss can be described by [4]:

$$-\frac{dE}{dx} = \frac{4\pi e^4 z^2}{m_0 v^2} NB \tag{2.3}$$

where

$$B \equiv Z \left[\ln \frac{2m_0 v^2}{I} - \ln\left(1 - \frac{v^2}{c^2}\right) - \frac{v^2}{c^2} \right] \tag{2.4}$$

Here, e represents the electron charge, m_0 represents the electron mass, v and z represent the velocity and charge of the incoming particle, Z and N represent the atomic number and number density of the atomic absorber composition, and I represents the experimentally determined mean excitation potential of orbital electrons in the absorber. In general, this description is valid for all types of charged particles in a monoatomic absorber under the following assumptions:

- The velocity of the particle is much larger than that of the orbital electrons ($v_e/v \ll 1$).
- All interactions are due to electronic stopping.

Equations 2.2 and 2.4 show that the amount of energy deposited by any charged particle into any absorber is primarily characterized by the particle's squared-charge and squared-velocity, and the density and atomic number of the absorber. As such, at a given velocity, recoil nuclei with $z > 1$ experience a much larger rate of specific energy loss than particles with unity charge, such as protons, electrons, and muons. However, in consideration of a specific particle in a specific absorber, an important consideration for designing particle detectors is that all terms of dE/dx depend, to varying orders, on the particle velocity v. B increases logarithmically with the square of the velocity, whereas the multiplicative coefficient changes with the inverse square of the velocity. This results in an asymptotic minimum of the magnitude of specific energy loss for a charged particle as its velocity approaches c, wherein the description of its specific energy loss would follow the radiative losses described in the previous section. Highly relativistic charged particles with $z = 1$ are, therefore, frequently referred to as *minimum ionizing particles*. In the case of a non-relativistic charged particle, namely that $v^2/c^2 << 1$, B can be described accurately by its first term only. At decreasing velocities, namely that the velocity of the charged particle and orbital electrons become more similar, charge exchange between the charged particle and the absorber atoms begins to take place, resulting in sudden changes in z.

The behavior of these different stages of velocity of the charged particle in a medium is best visualized in a plot of specific energy loss along the track of a charged particle. This is known as a *Bragg curve*. The Bragg curve for 5.49 MeV alpha particles traversing through air is shown in Figure 2.2 [5]. Bragg curves such as this are often heavily referenced for decisions regarding detector design for a given particle detection experiment. Additionally, while air is not a particular absorber of interest for analyses presented in this dissertation, Figure 2.2 provides a qualitative picture for the specific energy loss of alpha particles covering a wide range of alpha particle energies.

At high and low energies, the Bethe formulation begins to deviate from experimental measurements and requires additional corrections [6]. The corrections necessary are strongly dependent on the charge of the particle. These corrections are referred to as *shell corrections* and *density effect corrections* and are implemented in the Bethe formulation as follows[6][‡]:

$$S = {\frac{4\pi r_0^2 m_e c^2 Z_2}{Z}}^{2}_{1} \beta^2 \left[f(\beta) - \ln < I > - \frac{C}{Z_2} - \frac{\delta}{2} \right] \tag{2.5}$$

where:

- $r_0 = e^2/mc^2$
- $f(\beta) = \ln \left[\frac{2mc^2\beta^2}{1-\beta^2} \right] - \beta^2$
- $\beta = v/c$
- Z_1 is the particle atomic number.
- Z_2 is the target atomic number.

[‡]While the original work was presented by Fano, the description here follows the formulation presented in the review by Ziegler, who cites Fano's work [6].

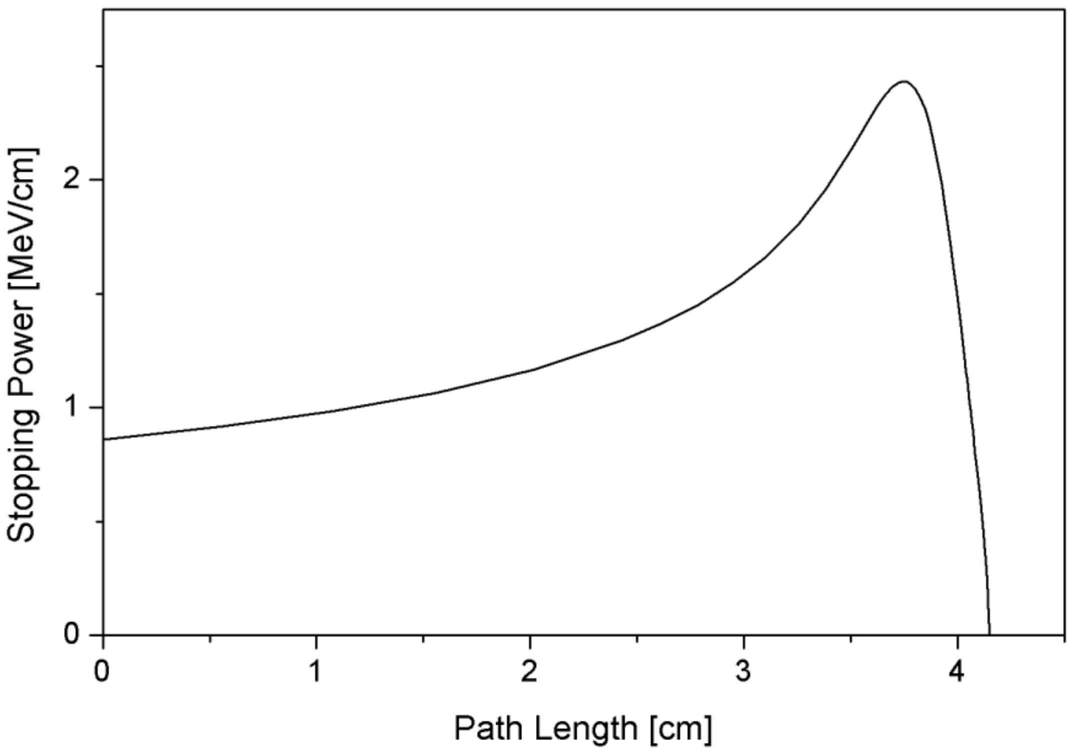

Figure 2.2: Example Bragg curve: Energy loss of alpha particles of energy 5.49 MeV in air.

- C/Z_2 is the shell correction term.
- $\delta/2$ is the density effect correction.

Traditionally, this is further expanded in powers of of Z_1 resulting in the commonly expressed stopping power formula as:

$$S = \frac{\kappa Z_2}{\beta^2}\left[L_0(\beta) + Z_1 L_1(\beta) + Z_2^2 L_2(\beta)...\right] \tag{2.6}$$

where $\kappa \equiv 4\pi r_0^2 m_e c^2$

The term in the brackets in Equation 2.6 contains all corrections to the two-particle energy loss process—at high and low energies—and is often expressed as the *Stopping Number*, $L(\beta)$, such that:

$$L(\beta) \equiv L_0(\beta) + Z_1 L_1(\beta) + Z_1^2 L_2(\beta) + ... \tag{2.7}$$

where each term represents a higher order correction[§]. This simplifies Equation 2.6 to:

$$S = \frac{\kappa Z_2}{\beta^2} Z_1^2 L(\beta) \tag{2.8}$$

For protons at energies down to 1 MeV, the maximum correction to the shell corrections is approximately 6%. The density effect corrections increase in magnitude at higher energies, typically around 1 GeV. For nuclear recoils, the shell corrections arise from the fact that the ion will begin to bind with electrons at lower energies, thereby changing its total charge[¶]. However, while these shell corrections improve the accuracy of the Bethe formulation, the deviations of the Bethe formulation to experimental results become large enough that a different approach is required.

2.3 SRIM

For recoil nuclei at lower velocities—typically in the range of $0.01 < \beta < 0.05$—there is no satisfactory theory to describe the specific energy loss [1]. In place of a theory, a formula derived from phenomenological fitting is used. This standard framework for calculating the expected stopping power in this energy range is the simulation package *Stopping and Range of Ions in Matter* (SRIM) [3].

[§]Historically, L_1 is known to as the *Barkas Correction*, and L_2 is known as the *Bloch Correction*.
[¶]As shown in Equation 2.4, the Bethe formulation requires a constant charge.

2.3.1 LSS formulation

‖For values of $\beta < 0.01$, the velocity of the particle becomes similar to that of outer atomic electrons. As such, the previously assumed approximation that only electronic stopping exists is no longer valid. Lindhard, Scharff, and Schiott (LSS) developed a framework using a Thomas-Fermi atomic model in order to obtain numerical calculations of the total stopping power [8]. Their framework is expressed in terms of:

- $\epsilon \equiv E_R/E_{TF}$
- $\rho \equiv R/R_{TF}$

where:

- $E_R \equiv$ energy of ionizing particle.
- $R \equiv$ stopping distance of ionizing particle.
- $E_{TF} \equiv \frac{e^2}{a} Z_i Z_T \frac{M_i+MT}{MT}$
- $R_{TF} \equiv \frac{1}{4\pi a^2 N} \frac{(M_i+M_T)^2}{M_i M_T}$
- N is the target atom number density, i is the ionizing particle index, T is the target substance index, and $a = a_0 \frac{.8853}{\sqrt{Z_i^{2/3}+Z_T^{2/3}}}$ [7].

Given these definitions, the total stopping power can be written as the sum of the electronic and nuclear stopping powers:

$$\frac{d\epsilon}{d\rho} = \frac{d\epsilon_e}{d\rho} + \frac{d\epsilon_n}{d\rho} \tag{2.9}$$

The LSS formulation shows that the electronic stopping power varies as $\frac{d\epsilon_e}{d\rho} = k\sqrt{e}$, where $k \equiv \frac{0.0973 Z_1^{1/6}}{(Z_1^{2/3}+Z_2^{2/3})^{3/4}} \left[\frac{Z_1 Z_2 (A_1+A_2)^3}{A_1^3 A_2}\right]$. For homonuclear recoils with $1 < A < 131$, this results in the small range of $0.13 < k < 0.17$ [7]. Furthermore it has been shown that with this description of $\frac{d\epsilon_e}{d\rho}$, values of $\epsilon < 1.6$ result in $\frac{d\epsilon_n}{d\rho} > \frac{d\epsilon_e}{d\rho}$ [7, 8]. This results in an increased probability in a recoil nucleus scattering elastically with other nuclei as it decreases in energy. At these low energies, the recoils with other nuclei are unlikely to produce ionization, but will still rapidly decrease in energy until it eventually recombines with electrons to form a thermalized, neutral atom.

‖This discussion follows the excellent summary presented in Reference [7].

CHAPTER 3
NUCLEAR RECOILS FROM FAST NEUTRONS

Fast neutron detection using nuclear recoils has recently become an increasingly important field of study. This chapter will discuss the neutron and the detection of energetic free neutrons in the context of directional detection and spectroscopy. Specifically, this chapter will discuss the neutron as a particle, the physics of fast neutron interactions with matter, particularly atomic nuclei, as well as an overview of current directional fast neutron detection technology.

3.1 The neutron

The neutron is a subatomic, electrically neutral particle that is most commonly found in atomic nuclei along with protons. Because of this, protons and neutrons are both commonly referred to as nucleons. Protons and neutrons are baryons—composite particles made up of quarks that are bound together by the strong interaction governed by *Quantum Chromodynamics (QCD)*. Protons consist of two up quarks and one down quark, and neutrons consist of one up quark and two down quarks. Because their internal quark structures interact via the strong force, the quarks of protons can interact with the quarks of neutrons, and vice-versa, via attractive residual effects of the strong force—often referred to as the residual strong force or nuclear force. This creates a large attractive force felt between protons and neutrons at distances of approximately 1 fm (10^{-15} m), which leads to the formation of atomic nuclei. Additionally, because its constituent particles have non-zero electric charge, the neutron has a small magnetic moment of approximately $\mu_n = -1.91\mu_N$, where μ_N is the *nuclear magneton* defined as:

$$\mu_N = \frac{e\hbar}{2m_p}$$

where e is the elementary charge, $\hbar$ is the reduced Planck's constant, and m_p is the mass of the proton.

The mass of the neutron is approximately a factor 1.008 larger than the mass of the proton. This results in a free neutron being unstable and decaying via the Weak interaction with a lifetime of approximately 900 seconds. In this decay, one of a neutron's constituent down quarks decays to an up quark by emitting a W^- boson, thus producing a proton, an electron, and an electron antineutrino. This decay is graphically represented in the Feynman diagram shown in Figure 3.1 [9].

To summarize, the general characteristics of the neutron is that it is a massive, long-lived, electrically neutral particle that interacts with other particles via the strong and weak forces. As a result, neutrons react almost exclusively with atomic nuclei in matter, which will be the topic of discussion in the next section.

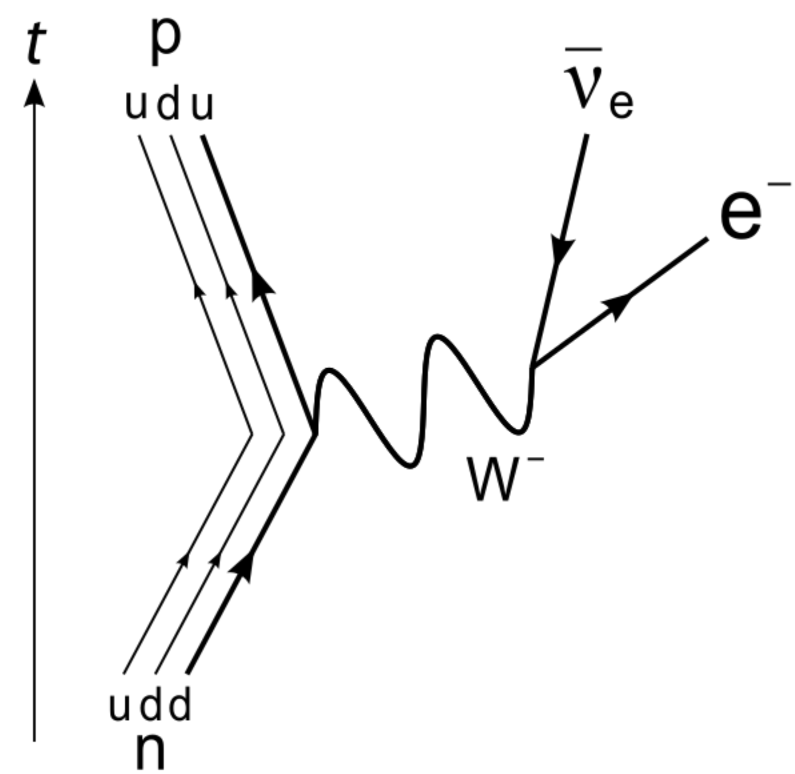

Figure 3.1: Feynman diagram for beta decay of a free neutron

3.2 Interaction of fast neutrons with matter

Neutron interactions with matter vary largely as a function of neutron energy, even in a single isotope, as can be seen in the total neutron interaction cross section for He^4 shown in Figure 3.2 [10]. It is therefore common to classify neutrons within ranges of energy, often referred to as neutron temperature. The common, but not exhaustive, classifications are:

- Thermal neutrons ($E_n \sim 0.025$ eV).

- Slow neutrons (0.025eV $< E_n <$ 100keV).
- Fast neutrons (100keV $< E_n <$ 20MeV).
- Ultrafast/relativistic neutrons ($E_n >$ 20 MeV).

This dissertation is focused on detection of recoil nuclei, and thus on the interactions of fast neutrons, which have typical energies in the 100 keV–20 MeV range.

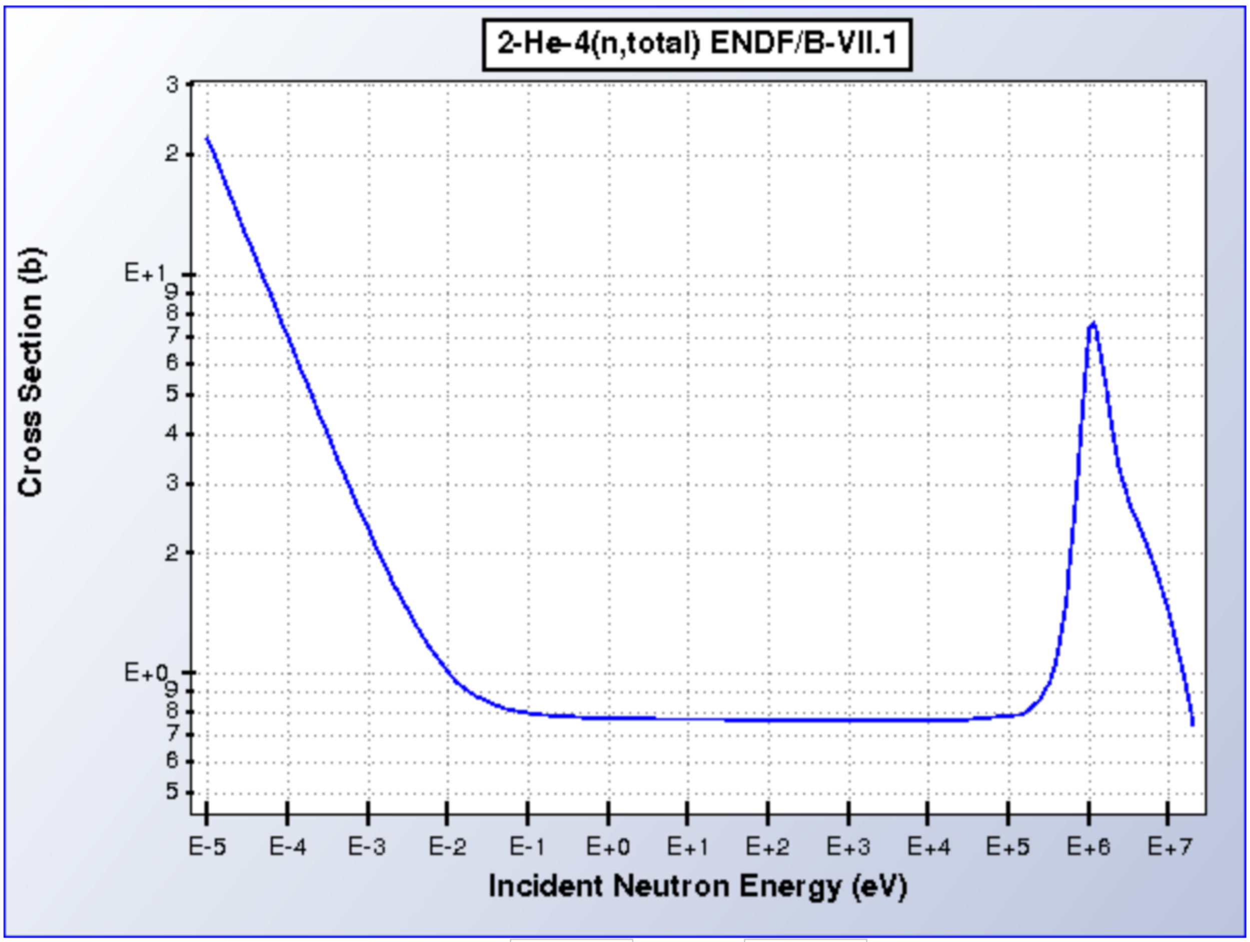

Figure 3.2: Total neutron interaction cross section for He^4 versus neutron energy. The cross section is to first order exclusively elastic.

Fast neutrons interact primarily with matter via scattering with atomic nuclei*. In these interactions, if the scattering is elastic, conservation of momentum and energy can be used

*Scattering of neutrons with orbital electrons would require *deep inelastic scattering*, which has an effectively-zero cross section for center-of-mass energies below 1 GeV [11].

Figure 3.3: Diagrams illustrating the lab frame (left) and center-of-mass frame (right) of a neutron scattering elastically with a target nucleus.

to show that the energy transfer between a single instance of elastic scattering between a neutron and a target nucleus is [12]:

$$E_R = \frac{2A}{(1+A)^2}(1 - \cos\Theta)E_n$$

where:

- A = total number of nucleons in target nucleus.
- E_n = neutron kinetic energy in lab frame.
- E_R = recoil nucleus kinetic energy in lab frame.
- Θ = scattering angle of neutron in center-of-mass frame.

$$\cos\theta = \sqrt{\frac{1 - \cos\Theta}{2}}$$

This results in the following equation for the energy of a recoil nucleus as a function of recoil angle in the laboratory frame [12]:

$$E_R = \frac{4A}{(1+A)^2}(\cos^2\theta)E_n \tag{3.1}$$

The relationship between Θ in the center-of-mass frame and θ in the laboratory frame is shown in Figure 3.3.

Equation 3.1 shows that for an individual neutron of energy E_n, there exists an unambiguous solution of the energy of a recoil nucleus for a given θ. However, E_n cannot be directly measured for each interaction. Therefore, measurement of E_R and θ are necessary. This provides a strong motivation for the development of directional detection of recoil nuclei for neutron detection.

Equation 3.1 also shows that there is an upper limit at to the amount of energy transferred to the recoil nucleus in elastic scattering, E_R, at $\theta = 0$ for a given isotope. This is a useful guideline for designing detectors of recoil nuclei, as events with larger energies are detected with greater efficiency. Table 3.2 shows the ratio of energy transfer for the maximum E_R to E_N for various isotopes. As can be seen, the maximum energy transfer decreases with increasing A. As such, hydrogen and helium based detectors are the most desirable isotopes for detection purposes. More generally, maximal energy transfer occurs when target mass equals the neutron mass and at a recoil angle of $\theta \sim 0$, resulting in [12]:

$$E_R|_{max} = \frac{4A}{(1+A)^2} E_n \tag{3.2}$$

Target Isotope	A	$\frac{E_{Rmax}}{E_N}$
${}^1_1$H	1	1
${}^2_1$H	2	8/9
${}^3_2$He	3	3/4
${}^4_2$He	4	16/25
${}^{12}_6$C	12	38/169
${}^{16}_8$O	16	64/289

Table 3.1: Ratio of maximum energy transferred of recoil nucleus to neutron energy for various isotopes of interest [12].

CHAPTER 4
NUCLEAR RECOILS FROM DARK MATTER

Dark matter is the name given to the non-luminous source of gravity found in abundance in cosmological structures that cannot be described by known and previously observed types of matter. While the gravitational effects of dark matter are observed and well established [13], non-gravitational detection of dark matter has not, at the time of writing, been unambiguously observed. However, there are a multitude of theories and models for dark matter. For the scope of this dissertation, we consider models in which dark matter consists of at least one type of particle which interacts with the Standard Model in any way in addition to gravitational interactions. Specifically, we consider descriptions of dark matter in which recoil nuclei can be produced by elastic scattering of a dark matter particle with atomic nuclei. This chapter provides motivation for this consideration and discusses how directional measurements of recoil nuclei could be used to provide directional measurements of dark matter in a way similar to fast neutrons, as presented in the previous chapter.

4.1 Recoil nuclei from dark matter

In order to use recoil nuclei to study the properties of dark matter, dark matter must interact with atomic nuclei. In general, there are few constraints that expressly forbid or, conversely, require such interactions. However, there are hints from cosmological observations that suggest dark matter should interact with matter and produce nuclear recoils via scattering of dark matter particles—often labeled χ—with quarks found in nucleons. This section discusses these observations to motivate nuclear recoil detection for directional dark matter studies. Additionally, since the material presented here will be based on constraints from the generally accepted cosmological observations, the exact theoretical details of interactions between dark matter and luminous matter will be not be explored and the implications will largely remain model independent.

Dark matter, like luminous matter, is currently theorized to have been created after the radiation-dominated early universe expanded and cooled. This is often referred to as the *freeze-out mechanism*, or *thermal production* of dark matter. The exact temperature of this freeze-out and the effects it has on luminous matter production are not precisely known and vary among models. However, the current consensus is that interactions in

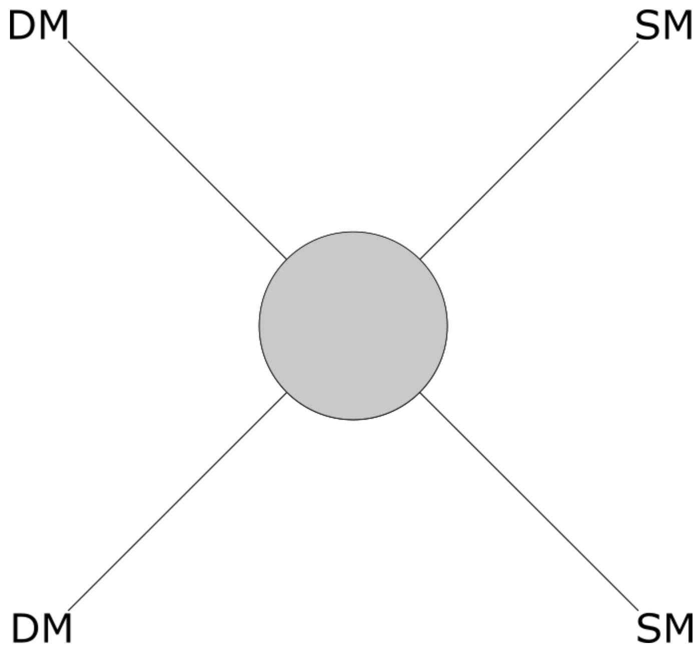

Figure 4.1: Simplified diagram of Dark Matter (DM) interactions with Standard Model (SM) particles. The circle at the center represents unknown processes that would mediate such interactions

the radiation-dominated early universe produced both dark matter and luminous matter, resulting in their observed relative densities. Simulations of these processes lead to structure formation very similar to that which is experimentally observed [14]. This production process can be qualitatively represented by the diagram in Figure 4.1, where dark matter particles (DM) and standard model particles (SM) interact via some currently unknown interaction or interactions—representing the conditions of the early universe—which are represented by the opaque circle.

This diagram, while incomplete, is a useful tool for conceptualizing the expected interactions between dark matter and standard model particles. When read with the time-axis increasing to the right, the diagram shows production of standard model particles via some interaction of dark model particles, and vice versa if read with the time-axis increasing to the left. This is representative of various interactions that likely took place in the early radiation-dominated universe. However, when read with the time-axis pointing upward—permitted by *crossing symmetry*—this represents a scattering process between dark matter and standard model particles. This implies that there should be a non-zero scattering cross-section between dark matter and atomic nuclei, giving rise to the production of recoil nuclei, as described in Chapter 2.

4.2 Recoil nuclei from dark matter

As discussed in previous chapters, the properties of the expected signature of recoil nuclei depend on the incoming particle. While few properties of dark matter are known, cosmological constraints on various properties provide insights on expected detection signatures. This section discusses those constraints and the expected signature of recoil nuclei induced by dark matter scattering.

4.2.1 Expected recoil signal of particulate dark matter

Experimentally measured rotation curves at the galactic radius of the sun suggest a significant concentration of dark matter, providing promise of detection. Furthermore, while the exact distribution of dark matter within our galaxy is not tightly constrained, a non-rotating, isothermal sphere of dark matter—often referred to as the *dark matter halo*—is commonly assumed for the galactic dark matter distribution [15]. The velocity distribution of dark matter particles in the halo follows a Maxwell-Boltzmann distribution with dispersion $\sigma_v = 155$ km/s. As our solar system orbits the galaxy in the galactic plane, it travels through a perceived *dark matter wind*. The halo model therefore predicts a relative velocity of dark matter particles, as measured on Earth, equal to the orbital speed of the sun around the galaxy at 220 km/s [7]. Furthermore, the vast majority of dark matter particles will be traveling at velocities smaller than the galactic escape velocity of $v_{esc} = 500$–600 km/s [15]. Using Equation 2.1, the maximum energy transfer an infinitely massive dark matter particle to a single nucleon* results in $W_{max} < 10$ keV/nucleon. This energy range falls within the regime of the *LSS formulation* of specific energy loss, described in Section 2.3.1.

Furthermore, the velocity of the dark matter wind changes relative to the motion of the earth around the sun. At minimum, this would lead to an annual modulation of detected dark matter rates [16], resulting in an increase of the rate in the summer months by approximately 10% and the opposite effect in the winter months. Additionally, the rotation of the earth about its axis produces a relative change in the dark matter wind velocity with a period of 24 sidereal hours. This daily oscillation causes the average direction of incoming dark matter particles to change by 96° every 12 sidereal hours [7]. This signal would require *directional* detection of dark matter in order to resolve the daily oscillation of the direction of the dark matter wind.

*Specifically, using $m = 1$ GeV/c^2, $m/M \ll 1$, and $v = v_{esc}$ in Equation 2.1.

CHAPTER 5
BEAST µTPCS

The BEAST µTPCs are a system of two Time Projection Chambers (TPCs) that provide 3D measurements of charge density distributions via micro pattern gas detectors used for analyzing fast neutron backgrounds during the commissioning efforts for SuperKEKB. SuperKEKB commissioning will be discussed in Chapter 6. This chapter provides a general description of this detector technology, namely principle of operation, calibration, and performance.

Furthermore, we describe the steps of calibrating and correcting the energy response of the TPCs using a dedicated simulation. The steps of this procedure as follows:

- Correct for charge-loss due to pixel saturation by determining the relationship between the charge-loss and the average number of saturated pixels per event.
- Correct for charge-loss due to the pixel threshold by determining the relationship between the charge-loss and the average Time-Over-Threshold (TOT) per pixel per event.
- Determine overall energy correction factor comparing the TPC response in the measured energy of the internal ^{210}Po calibration sources to a dedicated simulation of the calibration sources.
- Determine if an additional constant calibration factor is needed in the low-energy recoil regime by looking at dE/dx in experimental and simulated data.

Finally, we present various performance metrics of the background rejection and measurements of the energy and directionality of nuclear recoils.

5.1 Principle of operation

The TPCs detect recoil nuclei with a target-gas mixture of $^4_2$He and CO_2 (70% He, 30% CO_2) contained within a $2.0 \times 1.68 \times 10.0$ cm^3 active volume inside of a sealed vacuum vessel. This gas mixture was chosen as an optimized and safe gas for fast neutron detection. Via the processes described in Chapter 2, fast neutrons scatter elastically with target atoms in the gas mixture, producing $^4_2$He, $^{12}_6$C, and $^{16}_8$O recoil nuclei that leave a cloud of ionization behind as they propagate inside the gas volume. An electric field of 530 V/cm applied to

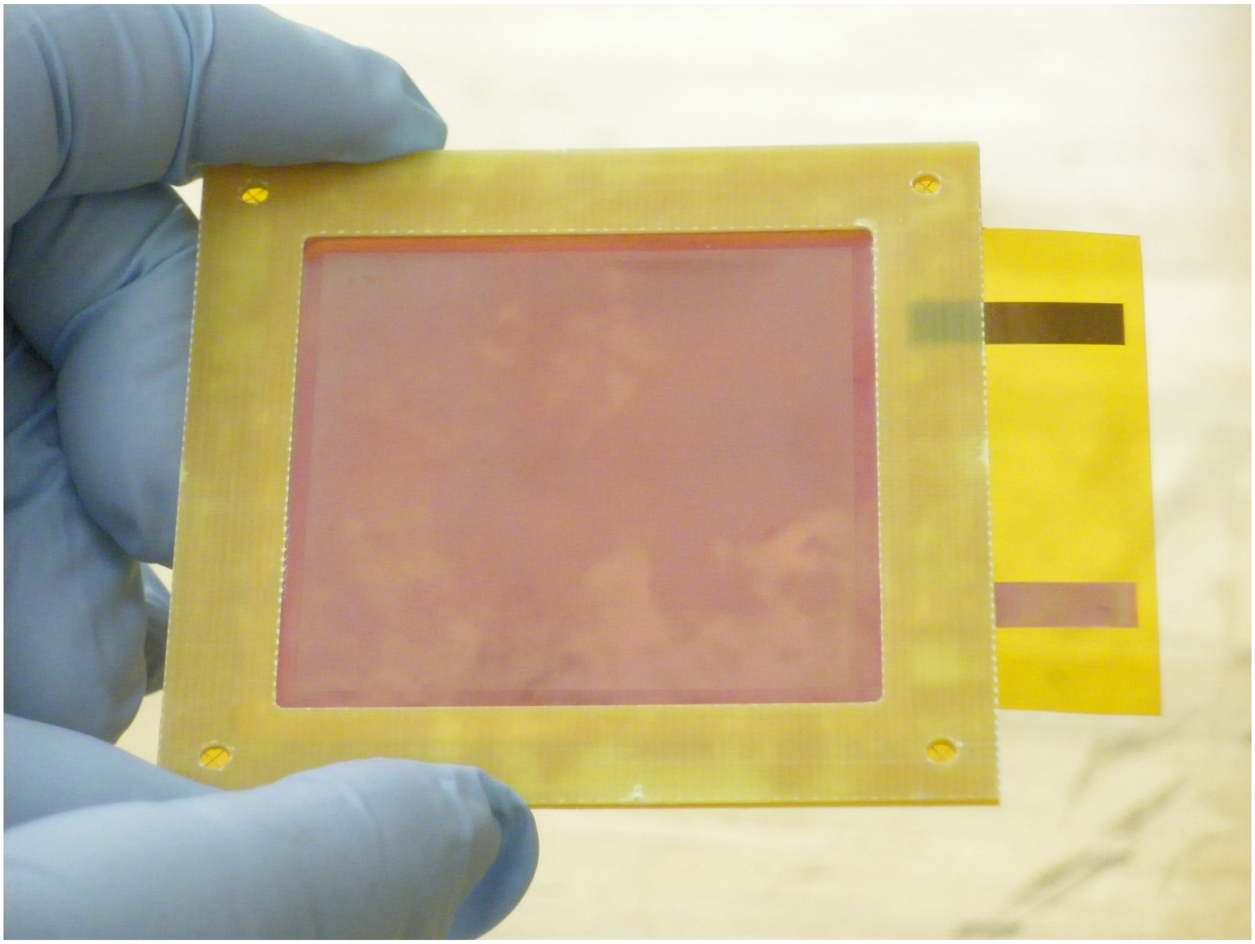

Figure 5.1: One of the 5 × 5 cm GEMs used to amplify charge in the TPCs.

the gas volume causes the electrons from the ion pairs to drift through two sequential Gas Electron Multipliers (GEMs) [17]. A picture of a single GEM is shown in Figure 5.1. The circuit diagram for the high voltage system is shown in Figure 5.2 [18]. The GEMs, held at high voltage, cause the electrons to avalanche, resulting in a gain with magnitude between 10–10^2 per GEM, depending on the applied voltage. After traversing through the GEMs, the amplified charge is collected by an ATLAS FE-I4B pixel ASIC—or *chip*—which digitizes the detected charge signal.

A schematic of the FE-I4B is shown in Figure 5.3 [19]. Reference [19] provides detailed documentation on the design and performance of the pixel chip. To summarize, the chip is an array of 26880 individual pixels arranged in 80 columns × 336 rows. Each pixel has an array of 250×50 µm^2, resulting in a 2×1.68 cm^2 active area for the entire chip. The columns and rows define the internal x and y components of the TPC internal coordinate

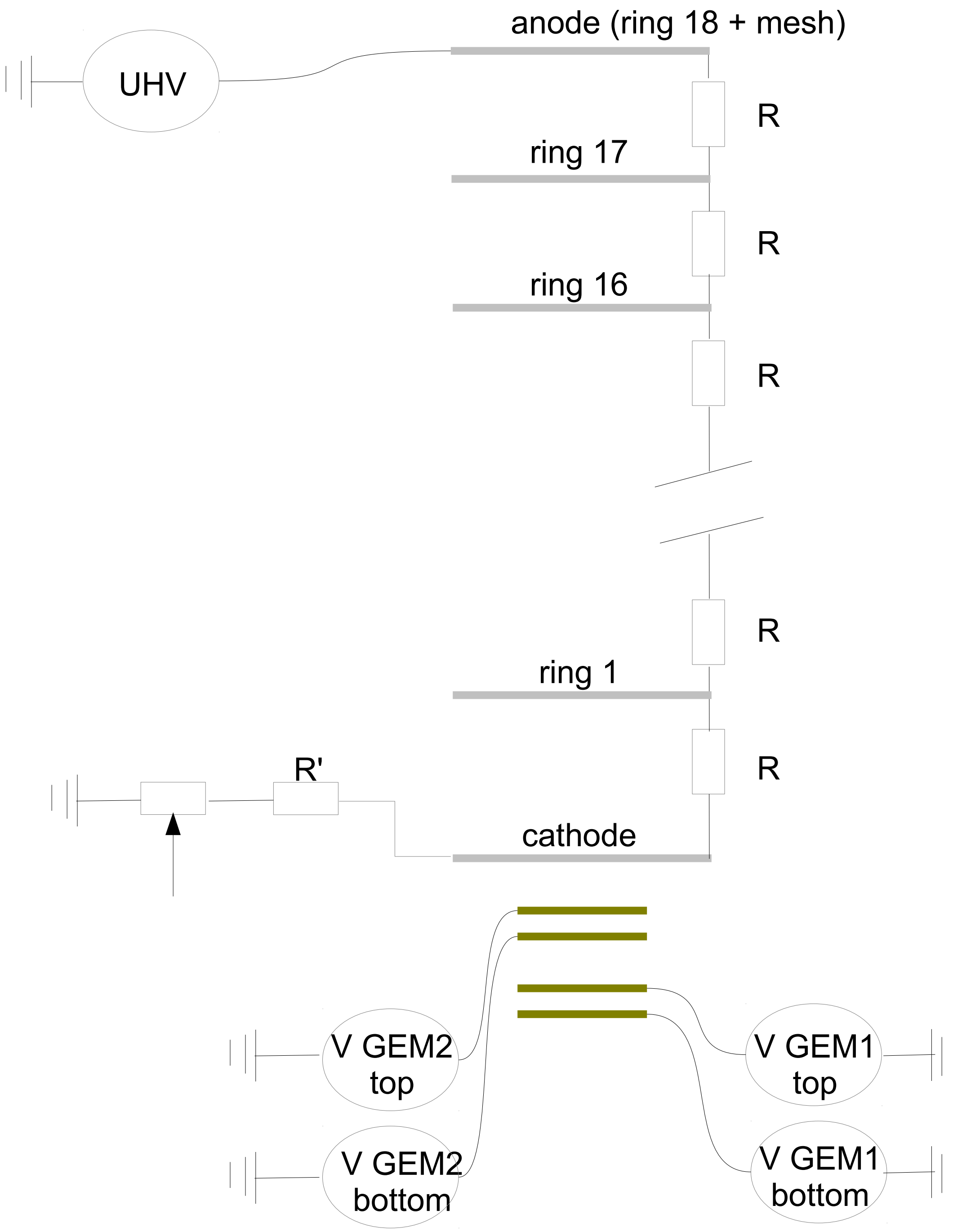

Figure 5.2: Circuit diagram for the TPC high voltage system consisting of a drift volume with a field cage and the GEM amplification region [18].

system, respectively.

The chip self-triggers when any individual pixel activates, defined by when the collected charge in a pixel rises above a configurable threshold. This marks the beginning of an event. After pixel activation, a 40 MHz clock is then used to sample the status of each pixel until all pixels measure charge below the threshold, marking the end of the event. The sampling is used to determine the charge and relative timing of the activation of all pixels in the event. The charge collected by a single pixel is determined by the number of samples, as measured by the 40 MHz clock, in which a pixel remains over the threshold. Unit of charge are integer numbers of *Time Over Threshold* (TOT), which correspond to an integer number of 25 ns in which a pixel is repeatedly measured to be above threshold. Finally, the drift coordinate used for 3D measurements comes from the clock-measured relative timing between sequential pixel activations. Electrons from the primary ionization travel through the drift volume at a constant velocity due to the applied drift field. This constant velocity along with uniform sampling time allows for reconstruction of the relative drift coordinates for all charge clusters detected by the pixels. Using Magboltz [20] to calculate the drift velocity and the 25 ns sampling clock, we find the quantization of the drift coordinate to be 250 µm. The resulting 2D reconstruction for multiple event types is shown in Figure 5.4. The pixel chip is interfaced via the pyBAR software, which communicates with the pixel chip via the USBPix2 [21] and SEABAS2 [22] data acquisition (DAQ) systems—both of which can be used interchangeably.

5.2 Track fitting

The reconstructed 3D pixel information is then fit to form a track. The fit algorithm is a MINUIT based χ^2 minimization of a straight, 3-dimensional line hypothesis. The algorithm simultaneously minimizes five parameters: polar and azimuthal angles—θ and ϕ, respectively—and 3 point coordinates in x, y, and z along the unit vector of the line. All parameters are given with respect to the internal coordinate system of the TPC, which is defined such that increasing column number corresponds to $+x$, increasing row number corresponds to $+y$, and the drift direction corresponds to $+z$. Of the 5 fit parameters, θ and ϕ are parameters of interest, as they provide the angular information of the reconstructed recoil track.

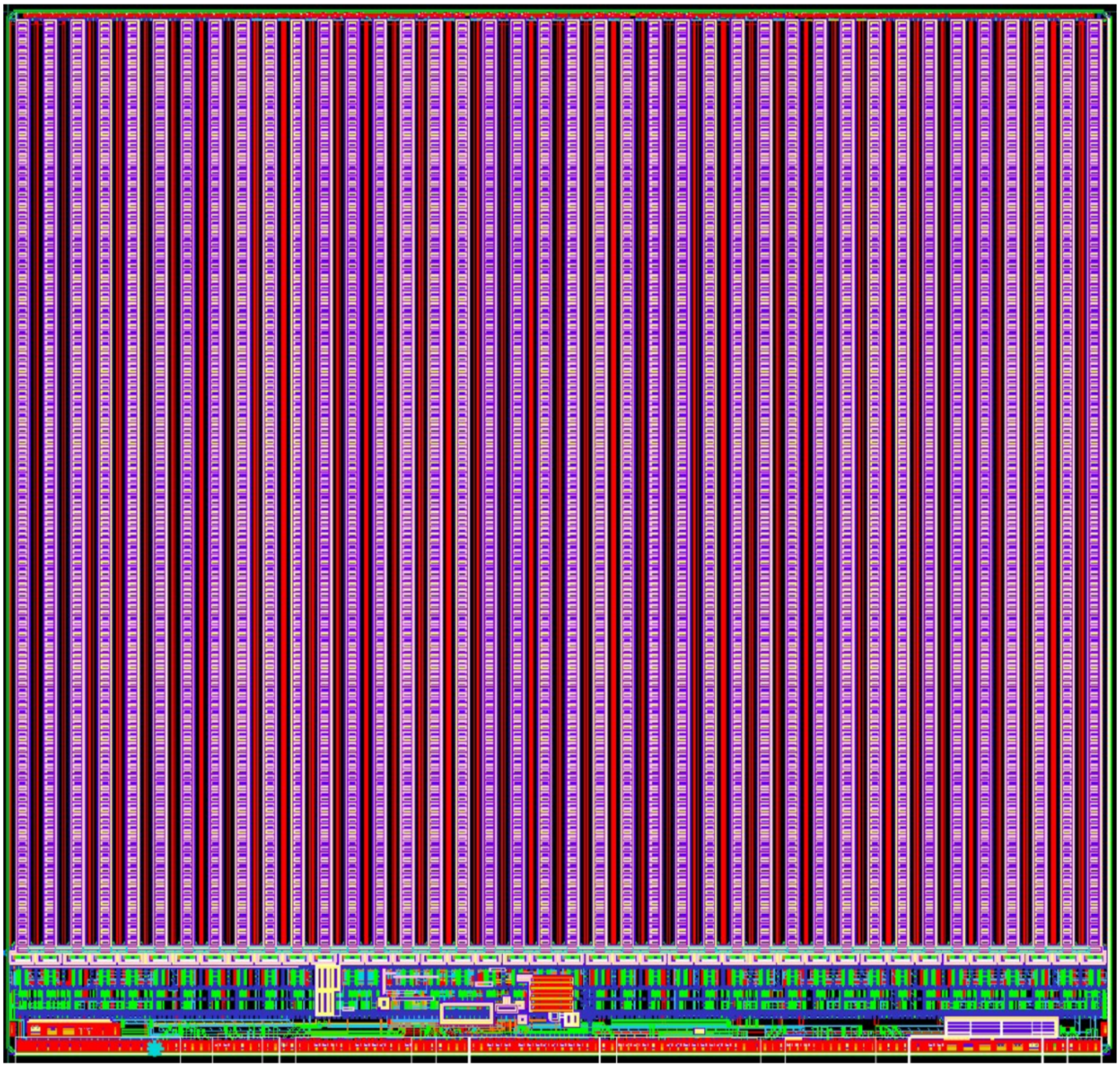

Figure 5.3: Top-down view of the ATLAS FE-I4 pixel chip layout. The origin for row and column number is at the top left, with column number increasing to the right and row number increasing downwards.

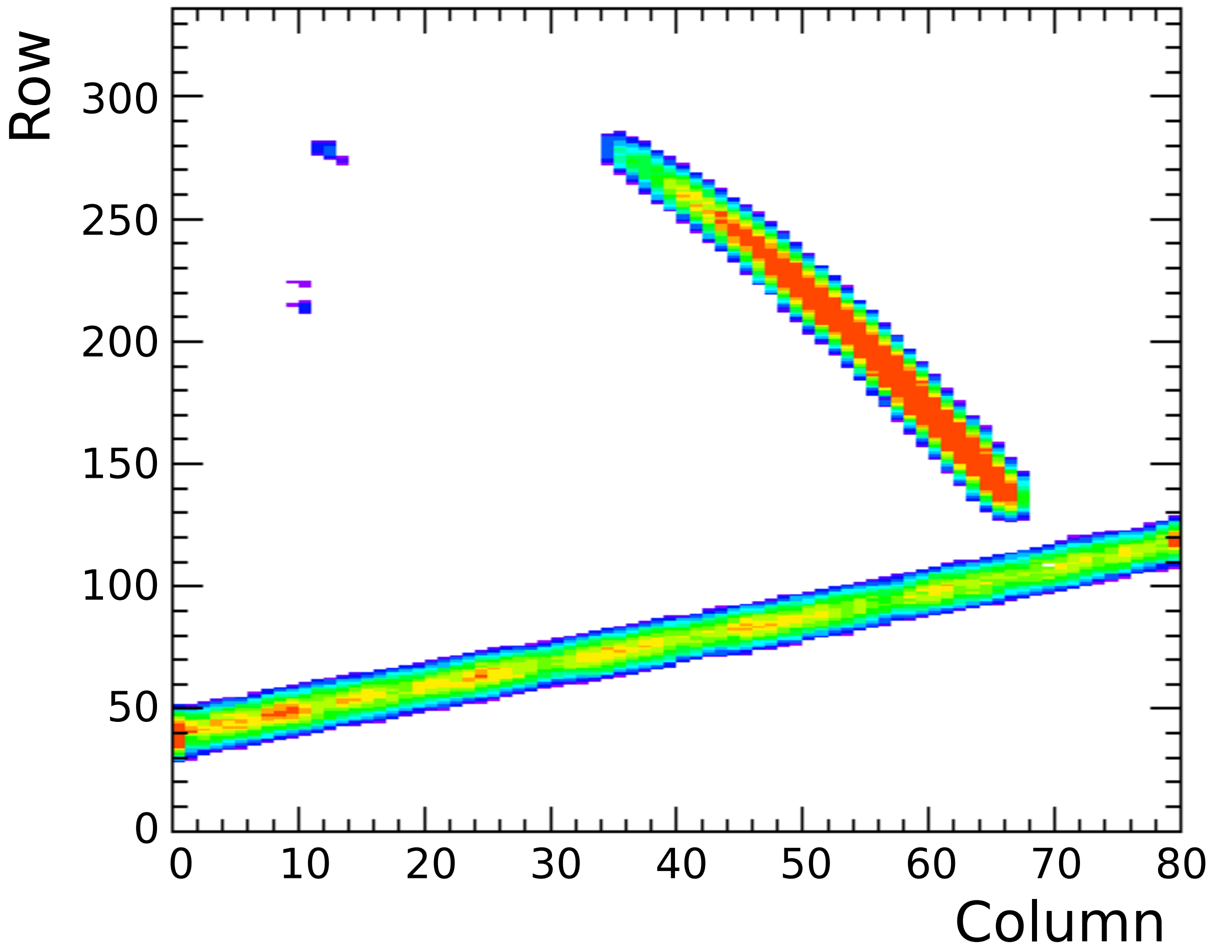

Figure 5.4: Three separate events detected by a TPC, superimposed in the same event display. The display is an occupancy plot of all of the pixels that triggered in the events, organized by row and column number. The color indicates the amount of charge collected in each pixel. The small isolated clusters are from X-rays, the long continuous track spanning the entire width of the pixel chip is from an MeV energy-scale alpha particle emitted from a ^{210}Po calibration source. The track completely contained within the chip area is our signal: the resulting nuclear recoil from a fast neutron elastically scattering off of a nucleus in the target gas.

5.3 Energy calibration

As previously mentioned, the pixel chip measures charge in units of TOT. In order to provided accurate and meaningful measurements of the detected charge to infer the amount of ionization in the primary charge cloud, one must translate these units of TOT into units of charge via calibration. This procedure consists of two steps—calibrating the pixel chip response and measuring the gain of the GEMs.

5.3.1 Pixel chip calibration

For calibrating the pixel chip, the response of all pixels in the chip must be uniform. This is done in each individual pixel via a test-pulser on the chip. Test pulses of varying charge values are repeatedly injected into each pixel as the DAQ software fine-tunes the charge-threshold and charge-integration time iteratively until variation in performance of all pixels is minimized at the desired threshold setting. The result is a mean threshold of approximately 2600 electrons. This calibration also measures the mean of the pixel noise to be of the order of a few hundred electrons. Since the noise level is approximately an order of magnitude below the threshold, the TPCs can achieve steady-state operational running without noise triggering the readout.

This calibration process allows converting units of TOT in individual pixels into electrons via the value of the capacitance of the built in test-pulser. While individual pixel calibrations can be applied, the spread in performance across individual pixels is small enough that the mean value is applied to all pixels in the event.

5.3.2 Measurement of GEM effective gain

The sum of all charge collected by the pixel chip results in a measurement of the total charge post-amplification. To convert this charge back into primary ionization generated by the recoil, a measurement of the double-GEM effective gain is required. The gain of a single GEM is primarily determined by the applied high voltage, and the gain of a double-GEM configuration is determined by multiplying the expected gain factors from the two GEMs. However, idealized conceptualization of the gain assumes that no charge in the primary ionization cloud is lost before the charge reaches the first GEM. The primary mechanisms by which charge can be "lost" during drift is by charge-loss by diffusion and charge-loss by recombination.

Charge-loss mechanisms

As electrons in the charge cloud traverse the drift volume, they undergo a random-walk process via collisions with bound atomic electrons, called *diffusion*, in which the average difference between adjacent electrons in the charge cloud will increase over time. For example, a group of electrons concentrated in a single point would spread out away from the original point into a Gaussian spatial distribution with increasing width over time. The behavior of this diffusion process can be described by [23]:

$$\sigma = \sqrt{Dt}$$

where

- σ is the width of the gaussian.
- t is time.
- D is the *diffusion coefficient*, obtained by gas transport models, such as Magboltz [20].

To first order, the drift velocity is constant for free electrons inside the TPC. Therefore it is useful to consider the diffusion versus drift distance—the distance along the z axis. This results in

$$\sigma = \sqrt{D \times z/v_d}$$

where z is the drift distance and v is the drift velocity. This shows that the width of the charge cloud depends on how far it drifts before being detected by the pixel chip. Assuming no charge is lost due to other mechanisms, this implies that the charge density per unit area will decrease when the charge reaches the pixels. Charge-loss by diffusion occurs when the fringes of the charge cloud diffuse enough that the charge collected by the pixels is below the configured pixel threshold. This undetected charge is referred to as *charge under threshold*. Charge under threshold is readily modeled by the implementation of charge transport modeling packages, e.g. Magboltz, in addition to accurate simulation of the digitization of charge performed by the FE-I4b chip.

The pixels also have a limited range of charge that can be measured. The pixel TOT range is 14 units. Because of this, a charge larger than a TOT of 14 will be recorded as exactly 14, thus misrepresenting the charge in collected by the pixel. We refer to this mechanism as charge loss due to *saturation*.

Independent of the configurations and performance of the pixel chip, electrons can also interact with positive ions in which an ion captures an electron to form a neutral particle before reaching the GEMs. This is charge-loss from *recombination*. There are two common types of charge-loss due to recombination—*columnar*, or *initial*, recombination and *volume* recombination [23]. The former type of recombination occurs on short time scales after the primary ionization is created. If the density of generated ion pairs along the track is large, it is possible for electrons and positive ions to recombine before they can be separated by the applied drift field. The effect of this type of charge loss varies depending on the local conditions of individual tracks.

The latter form of charge loss, charge loss from volume recombination, occurs when drifting electrons recombine with atoms after they have drifted away from the initial production area. In an ideal volume of pure $^4He:CO_2$, this type of recombination should be rare and negligible. However, electrophilic substances such as oxygen and water vapor are abundant in air. As such, when the vacuum vessel is initially purged of air and replaced with the target gas, residual electrophilic impurities are still present in the drift volume for a significant amount of time due to the desorption of these substances from the surfaces of the TPC internal components. This surface desorption process is also known as *outgassing* and can last for days or even weeks until charge-loss is minimal. The magnitude and time in which impurities can affect the gain of an individual typically varies largely in comparison to similarly constructed detectors, thereby making prediction and accurate simulation of this effect difficult.

Effective gain measurement

To account for these charge-loss mechanisms, we utilize calibration sources that are mounted inside of the TPC vessel in order to measure the effective gain *in situ*. The sources used are 10 nCi ^{210}Po sources that emit alpha particles with average energy of approximately 5 MeV. There are two sources inside each TPC on the outside of the field-cage installed at different drift lengths and local x coordinates—allowing for discrimination of individual sources. The source installed at largest drift distance is referred to as the "top" source, and the other is referred to as the "bottom" source. The physical setup of this configuration is shown in Figure 5.5. Comparing in-situ measurements of events from the calibration sources to a dedicated Geant4 Monte Carlo simulation [24] provides a relative correction factor for each TPC.

To achieve this, we first check the stability of the gain versus time. This requires selecting

Table 5.1: Fit parameters obtained from fitting detected charge in calibration alpha events in TPC H, shown in 5.6, to a line.

	$m \times 10^{-4}$	$b \times 10^{-7}$
Top	-1.4 ± 4.9	4.11 ± 0.02
Bottom	-6.8 ± 4.1	4.34 ± 0.01

a sample of events from the calibration sources in a TPC. Reconstructed alpha events are selected by their unique signal of a long track with a large dE/dx that spans the entire width of the pixel chip, as shown in Figure 5.4. Once a collection of calibration events are achieved, we then check the stability of the signal from these events by plotting the total detected charge in an event versus time. This is shown in two similarly-constructed TPCs*—referred to as "TPC H" and "TPC V"—in Figures 5.6 and 5.7. In these plots, we note that, as expected, events from the bottom source have, on average, more charge per event than events from the top source. This is due the aforementioned effects of charge loss. We also note from this plot that the gain is very stable over the course of many hours. Specifically, the slope of each line is very near zero—a few percent change per hour, at most. The values obtained from the fit are listed in Tables 5.1 and 5.2.

After establishing that the gain is stable, a gain correction factor must be calculated for each TPC. The first step in this process is to determine the effects of the charge-loss mechanisms described earlier. To look for these effects, we plot a histogram of the dE/dx distributions of all sources in experimental and Monte Carlo data. The Monte Carlo, described in detail in Ref. [24], simulates a point-like source, whereas the physical sources are not point-like. As such, tight selections on the opening angle of the source are chosen. Specifically, the angle θ is selected to be $89.5 < \theta < 90.5$, corresponding to $\pm 0.5°$ from a perfectly horizontal track. The dE/dx distributions for these events are shown in Figure 5.8.

In Figure 5.8, it is clear that each physical TPC differs in gain from the other, and both have an effective gain lower than the simulated TPC, which assumes a uniform gain of 1500. This requires a more thorough investigation of the above-listed charge-loss mechanisms. One can look for evidence of the effects of charge loss from diffusion and saturation by looking at the distribution of TOT in each peak in the simulated TPC. This is shown in Figure 5.9. As can be immediately seen in the TOT distribution for the bottom source, a significant amount of charge is lost due to saturation.

*The reason for the naming will be discussed in Chapter 6. The important point is that these are two TPCs that are built to perform identically.

Table 5.2: Fit parameters obtained from fitting detected charge in calibration alpha events in TPC V, shown in 5.7, to a line.

	$m \times 10^{-4}$	$b \times 10^{-7}$
Top	-22.9 ± 3.4	2.87 ± 0.01
Bottom	-8.9 ± 4.4	3.34 ± 0.01

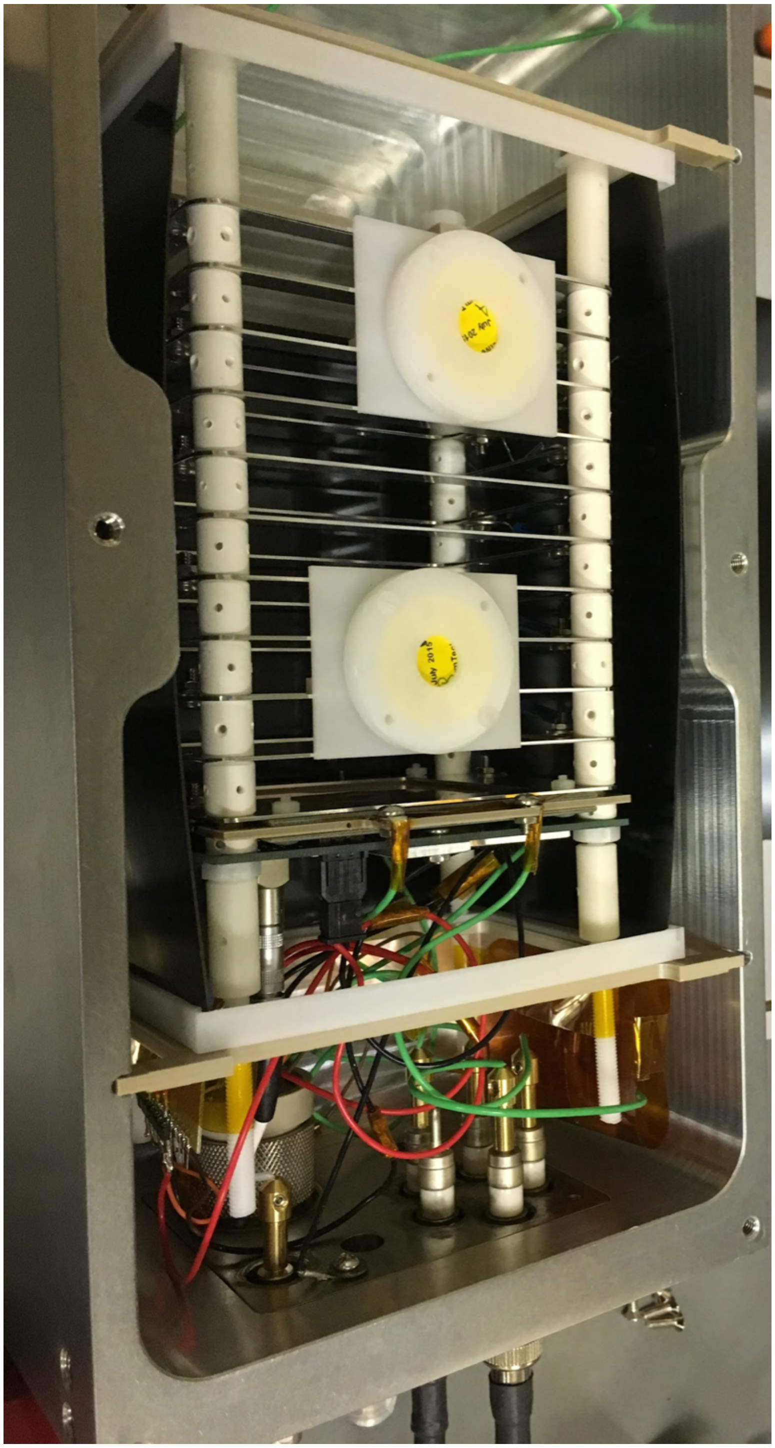

Figure 5.5: A photo of the inside of a TPC showing the ^{210}Po calibration sources. The white containers with the yellow centers in the upper half of the photo hold source holders. The source holder at the top of the photo is the “top” source—the source at largest drift distance—and the source holder towards the bottom of the photo, closest to the green wires, is the “bottom” source—the source at smallest drift distance.

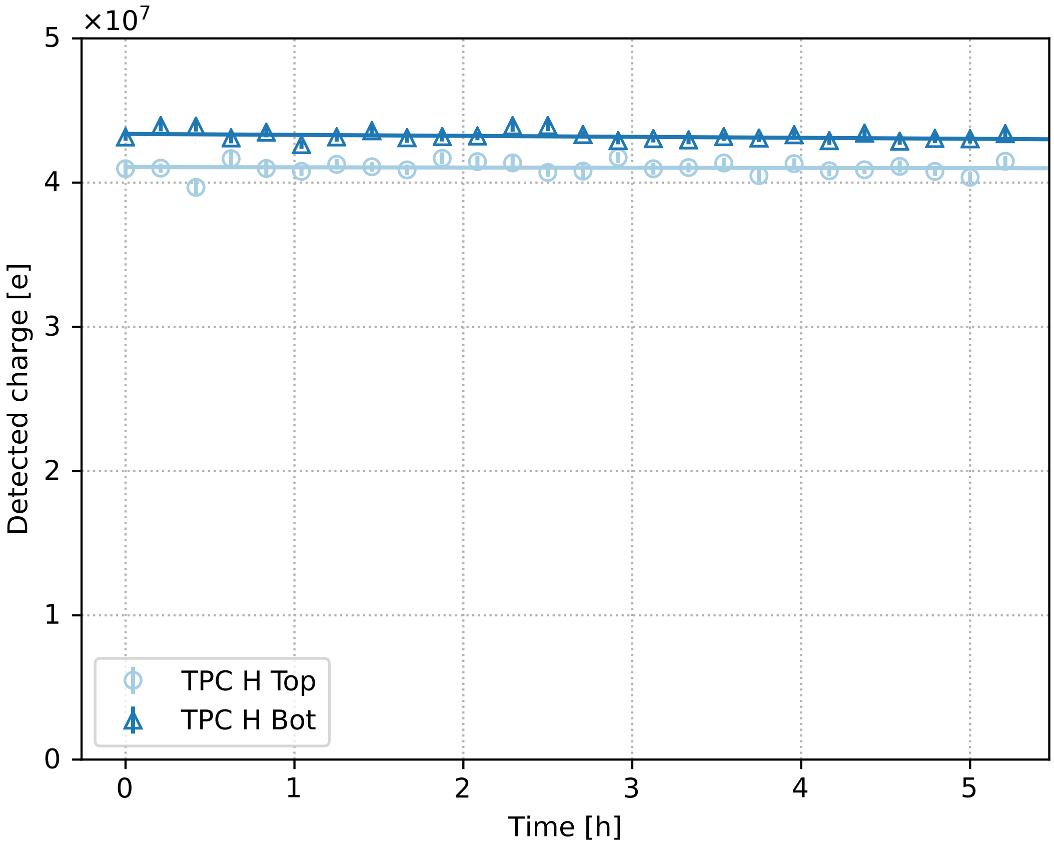

Figure 5.6: Detected charge of alpha particle calibration events in TPC H versus time. The dark blue triangles in each plot correspond to the bottom ^{210}Po source, corresponding to the source at smaller drift distance, and the light blue circles correspond to the top calibration source at larger drift distance. The fitted lines represent the change of energy over time of events from each internal calibration source. The fit results are shown in Table 5.1.

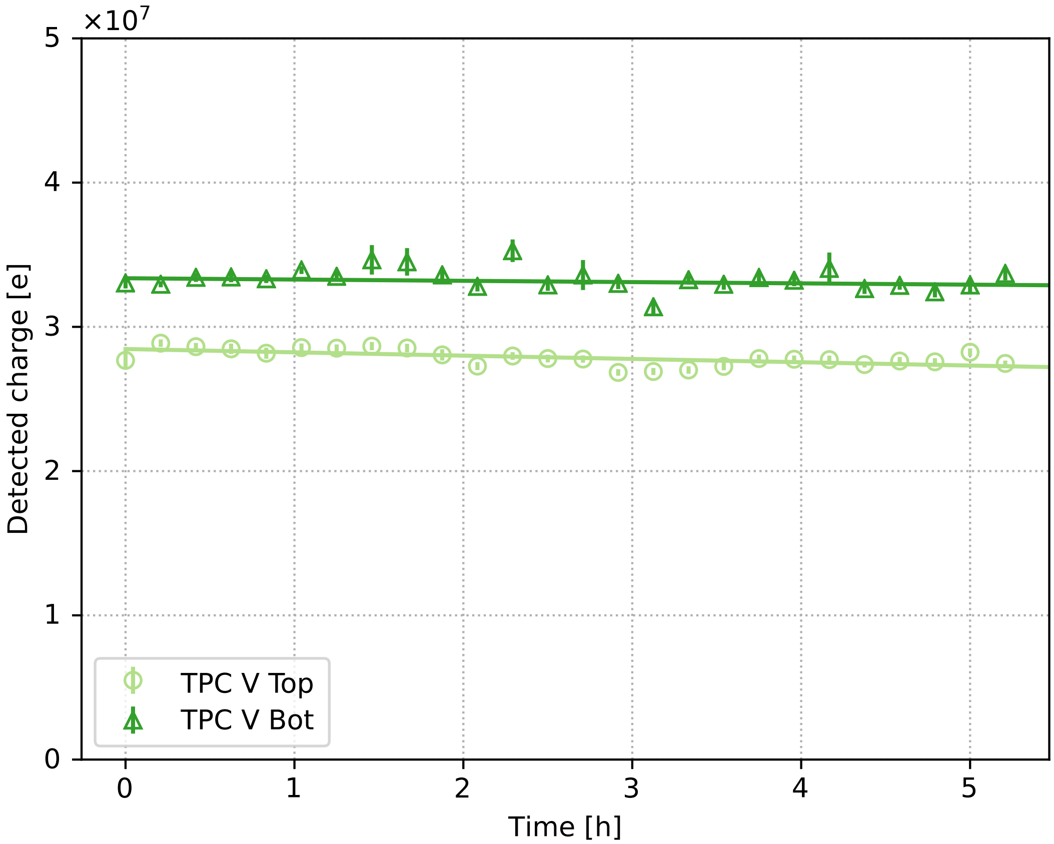

Figure 5.7: Detected charge of alpha particle calibration events in TPC V versus time. The dark green triangles in each plot correspond to the bottom ^{210}Po source, corresponding to the source at smaller drift distance, and the light green circles correspond to the top calibration source at larger drift distance. The fitted lines represent the change of energy over time of events from each internal calibration source. The fit results are shown in Table 5.2.

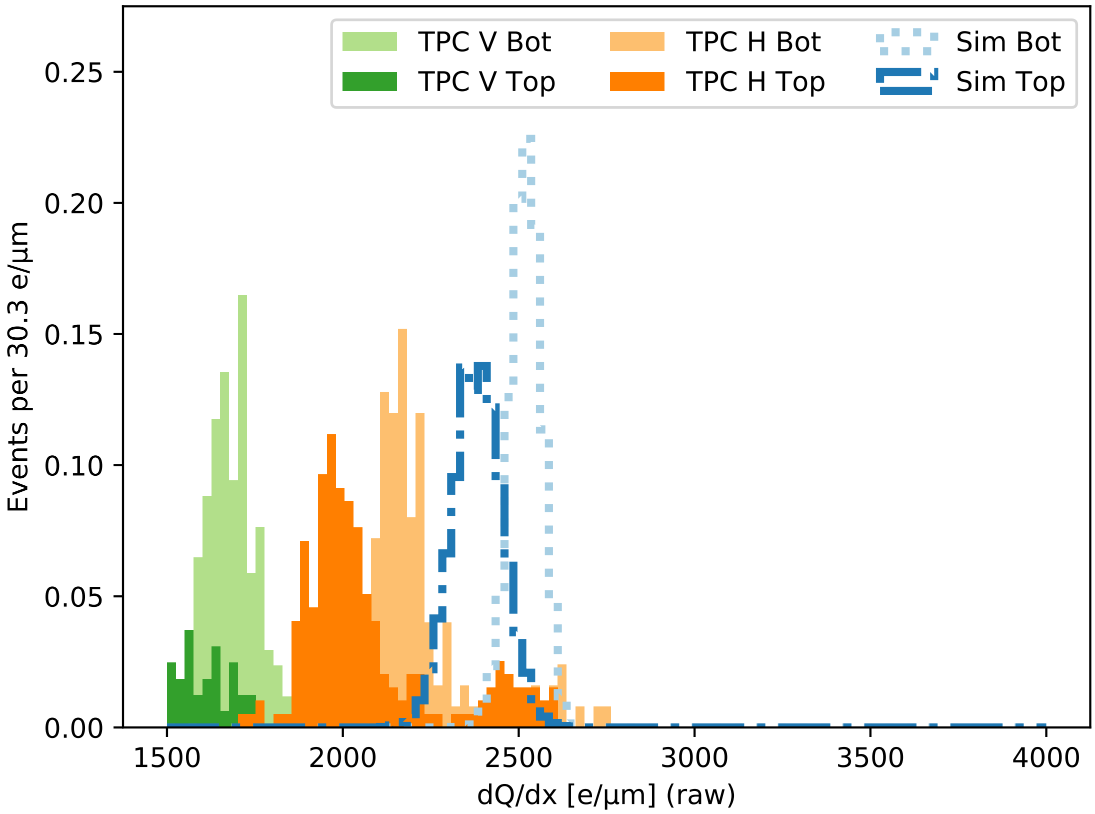

Figure 5.8: Histograms of the reconstructed detected charge divided by track length before calibrations for events from internal ^{210}Po calibration alpha sources in experimental and Monte Carlo data before application of any energy-scale corrections. The vertical axis shows the total number of events from both sources, normalized to 1, for two TPCs and Monte Carlo separately.

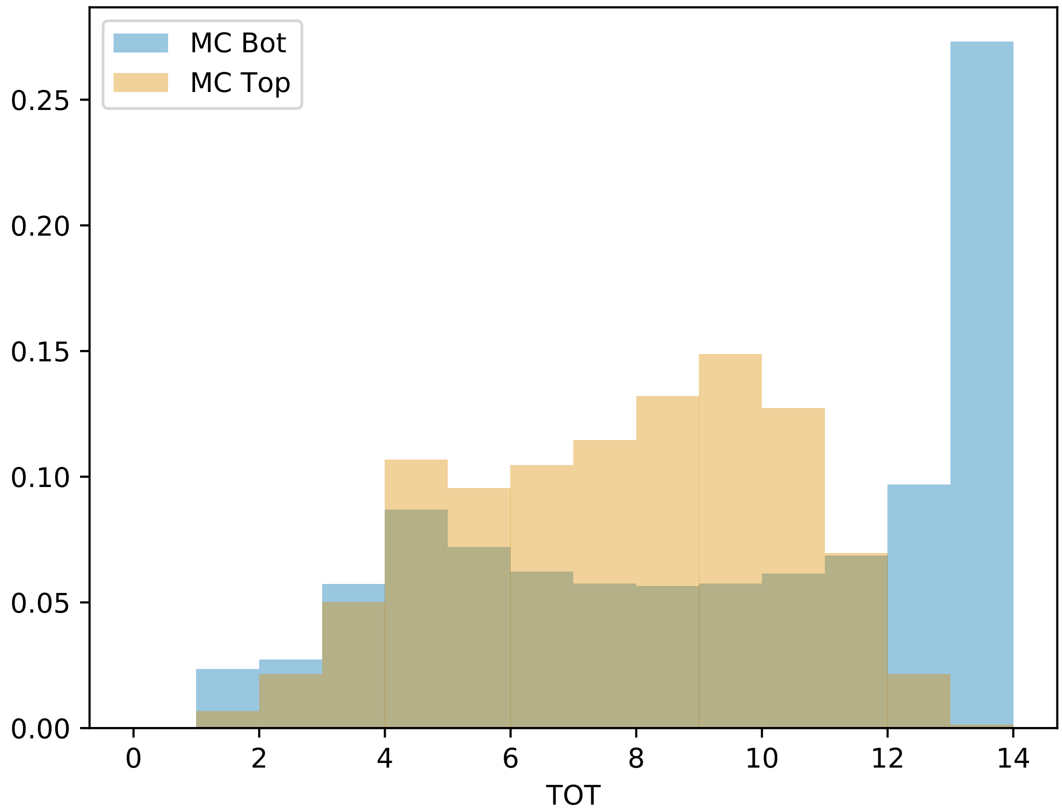

Figure 5.9: TOT distributions of simulated events from the top and bottom calibration sources in a TPC at a gain of 1500.

In order to correct for charge loss from saturation, we turn to a dedicated Monte Carlo simulation of nuclear recoils, the details of which are described in Chapter 6. In this simulation, the true particle initial energy can be compared to the energy reconstructed from the simulated TOT in the event. This is possible by selecting nuclear recoil events that are entirely contained within the sensitive, or *fiducial*, volume of the TPC. We achieve this by excluding events with activated pixels within 500 µm of the edge of the pixel chip. We require this criteria for the simple reason that if ionization is recorded at the edge of the chip, it is unknown what fraction of the recoil energy was lost specifically due to charge-loss mechanisms.

After applying this fiducialization, we plot the ratio of the reconstructed energy (E_{reco}) to the true energy (E_{truth}) in an event versus the number of saturated pixels in the event. This is shown as scatter plots in Figures 5.10, 5.11, and 5.12 for helium recoils, carbon

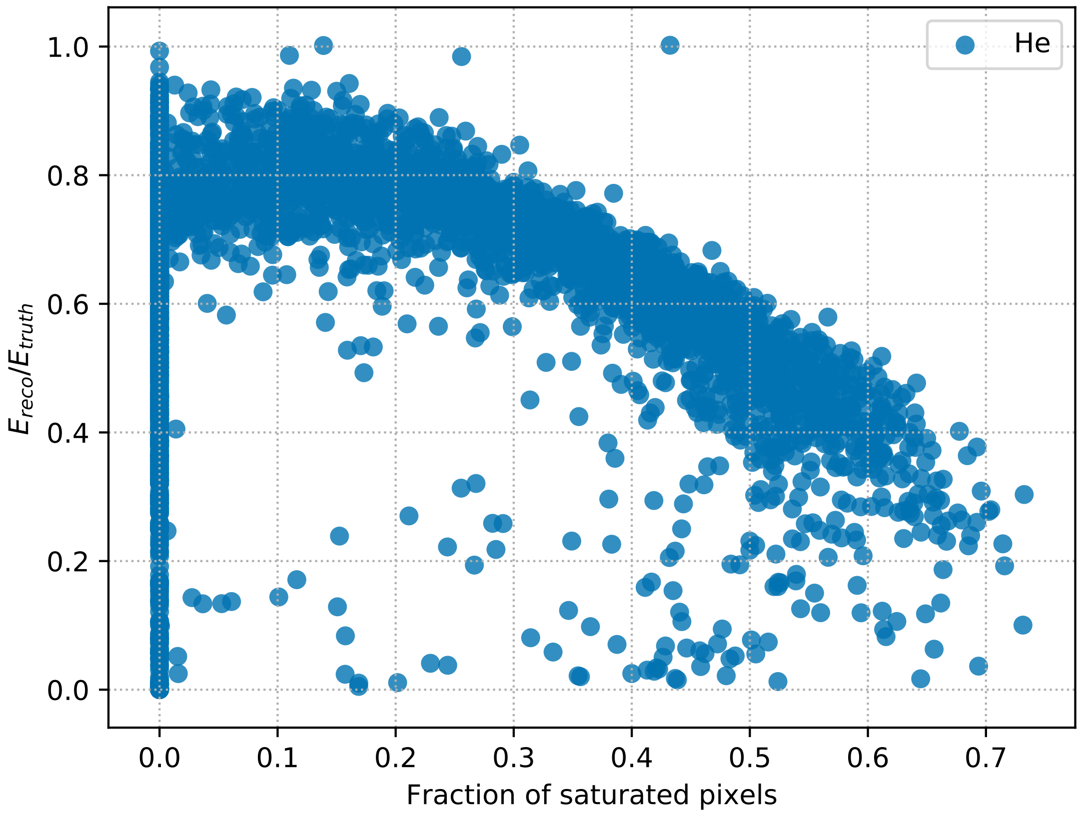

Figure 5.10: Ratio of reconstructed to true recoil energy versus the number of pixels with saturated TOT in simulated helium recoils.

and oxygen recoils, and all recoils, respectively. By binning the distribution in Figure 5.12 along the horizontal axis and plotting the mean and error on the mean of each bin, we can fit the distribution to a polynomial of order 4 to obtain a correction function for the charge lost to saturation. This is shown in Figure 5.13. The values of the fit are shown in Table 5.3. Applying this correction function to the distributions in Figure 5.8 results in the saturation-corrected distributions shown in Figure 5.14.

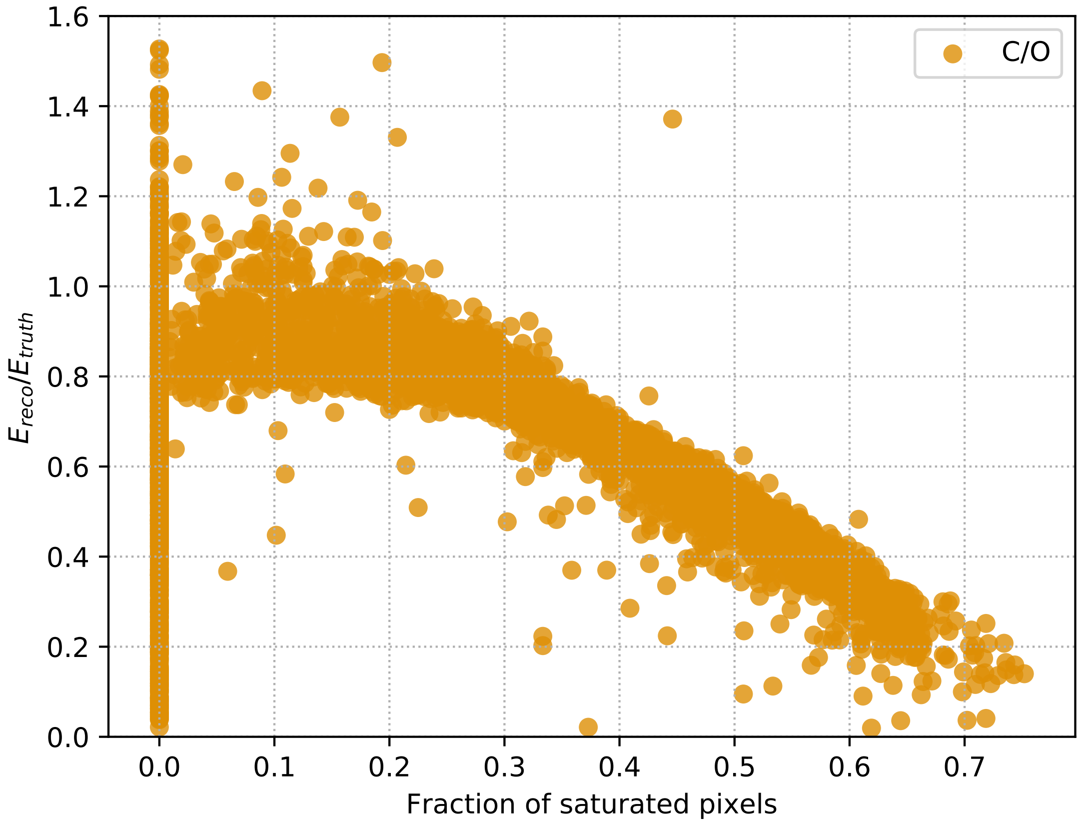

Figure 5.11: Ratio of reconstructed to true recoil energy versus the number of pixels with saturated TOT in simulated carbon and oxygen recoils.

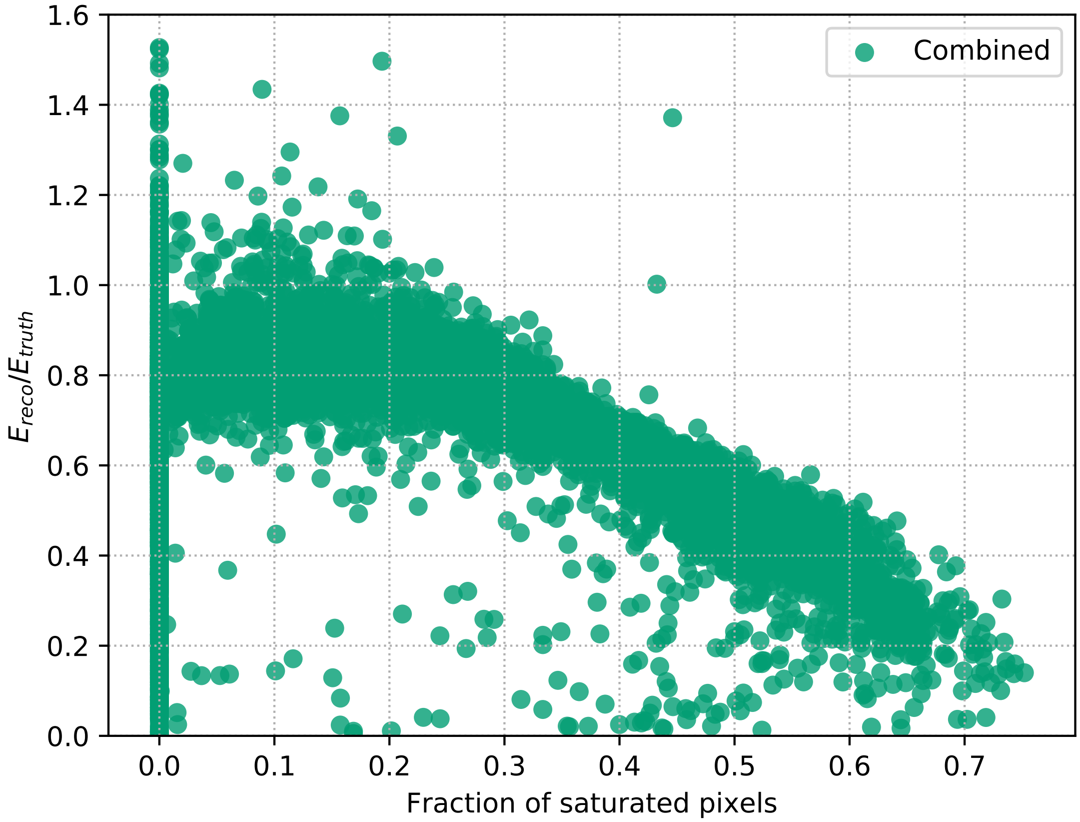

Figure 5.12: Ratio of reconstructed to true recoil energy versus the number of pixels with saturated TOT in all simulated recoils.

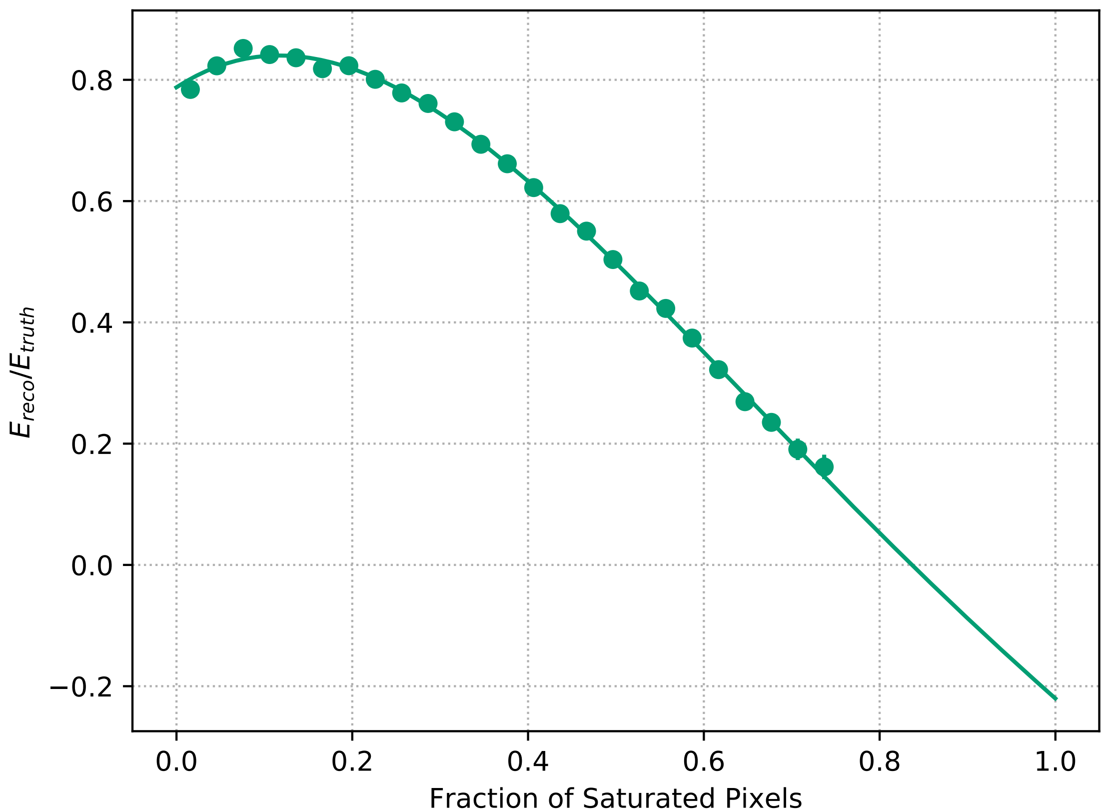

Figure 5.13: Ratio of reconstructed to true energy versus fraction of saturated pixels per event in all simulated recoils, binned and fit to a fourth order polynomial.

Table 5.3: Parameter values returned by the fourth order polynomial fit shown in Figure 5.13. Here c_i corresponds to the coefficient of the i^{th} power of x in the polynomial function.

	Central Value	Hesse Error
c_4	-1.03	1.11
c_3	3.73	1.66
c_2	-4.65	0.84
c_1	0.94	0.17
c_0	0.79	0.01
χ^2/ndf	1.22	

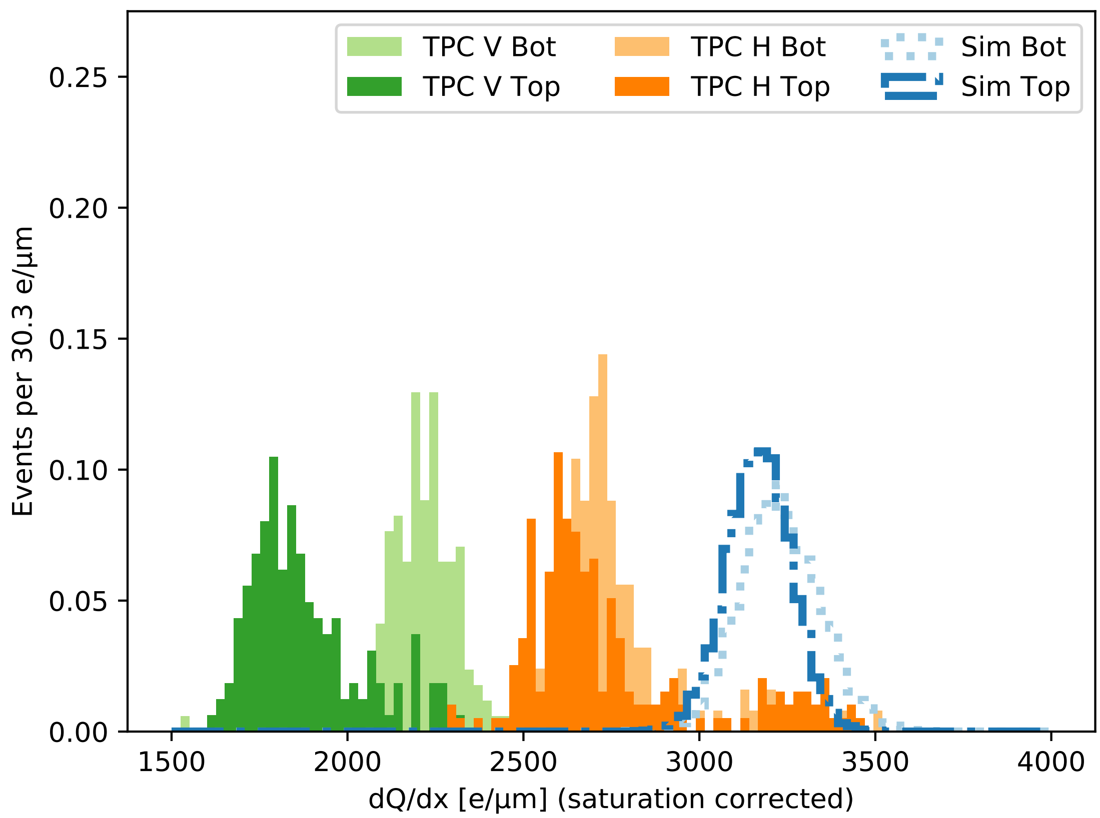

Figure 5.14: Histograms of the reconstructed detected charge divided by track length after correcting for pixel saturation via the fitted function shown in Figure 5.13, for events from internal ^{210}Po calibration alpha sources in experimental and Monte Carlo data. The vertical axis shows the total number of events from both sources, normalized to 1, for two TPCs, and Monte Carlo separately.

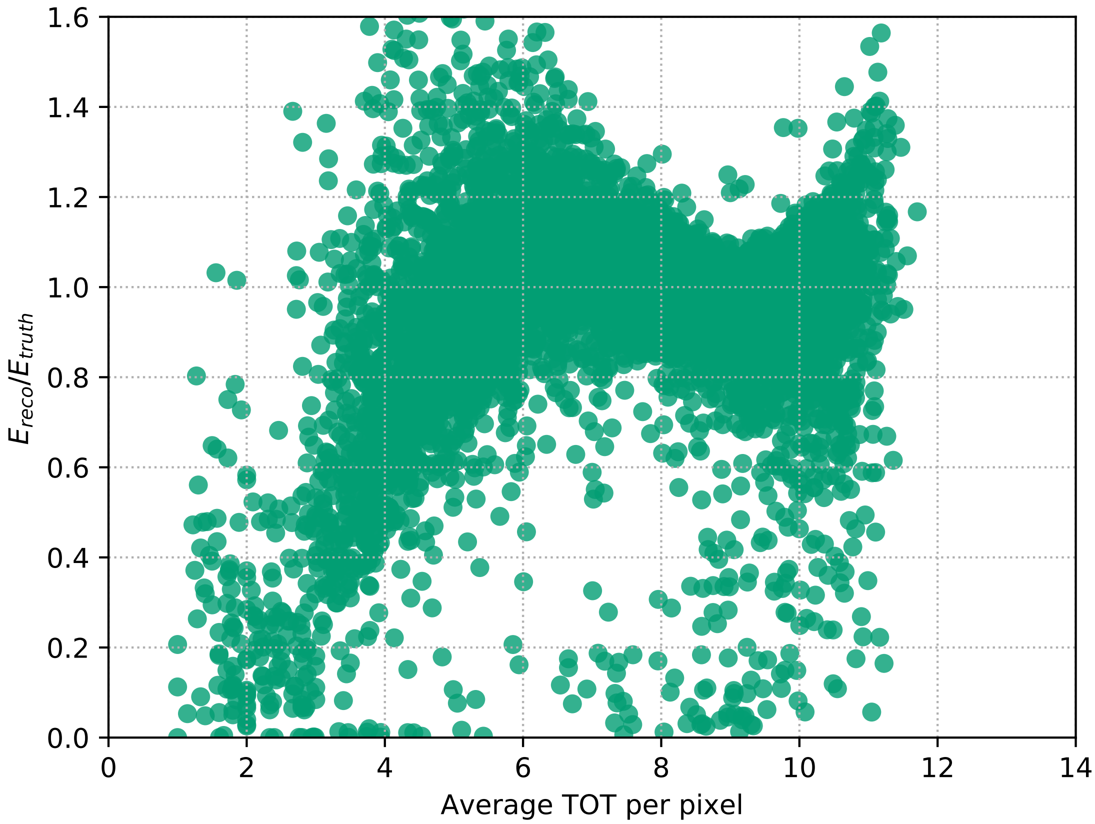

Figure 5.15: Ratio of reconstructed to true recoil versus average TOT per pixel in in all simulated recoils.

After correcting for charge loss due to saturation, the same procedure can be done for accounting for charge lost due to the pixel threshold. We can see this by plotting E_{reco}/E_{truth} versus the average TOT in the event after correcting for charge loss from saturation. A scatter plot of this distribution for all recoils is shown in Figure 5.15. In the same fashion as for charge loss from saturation, we bin and fit this distribution to a polynomial—in this case a fifth order polynomial. The fit of a fifth order polynomial to the binned representation of the data is shown in Figure 5.16, and the resulting parameters of the fit are listed in Table 5.4.

After applying both the saturation correction and the under-threshold correction, we plot the fully corrected version of Figures 5.8 and 5.14. This is shown in Figure 5.17. We now use these peaks to obtain correction factors for the gain of the physical TPCs to match the

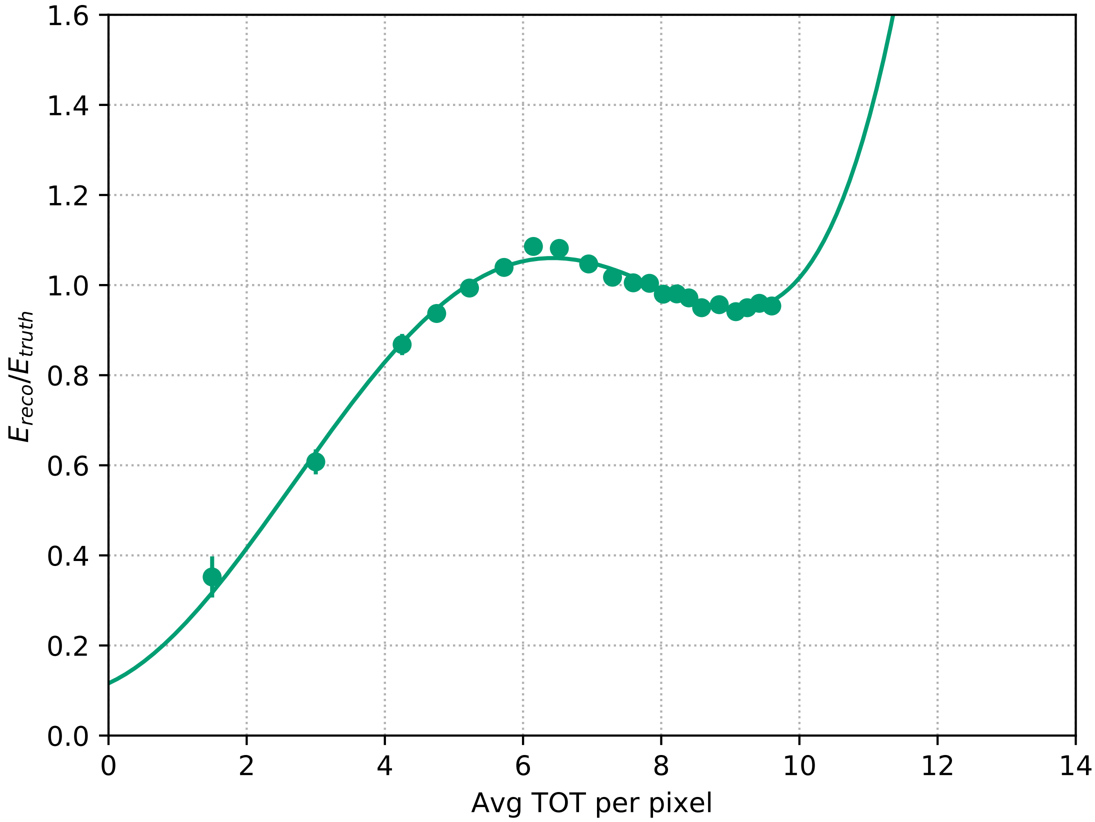

Figure 5.16: Ratio of reconstructed to true energy versus the average TOT in a single pixel per event binned and fit to a fifth order polynomial.

Table 5.4: Parameter values returned by the fifth order polynomial fit shown in Figure 5.16. Here c_i corresponds to the coefficient of the i^{th} power of x in the polynomial function.

	Central Value	Hesse Error
c_5	6.7×10^{-5}	3.2×10^{-7}
c_4	-7.9×10^{-4}	3.5×10^{-6}
c_3	-3.5×10^{-3}	3.2×10^{-5}
c_2	4.9×10^{-2}	2.7×10^{-4}
c_1	7.0×10^{-2}	2.2×10^{-3}
c_0	1.2×10^{-1}	1.2×10^{-2}
χ^2/ndf	2.46	

Table 5.5: Table of values of corrected dQ/dx in TPC H, TPC V, and Monte Carlo simulation and resulting conversion factors. A mean value of dQ/dx obtained from averaging the dQ/dx of each of the two ^{210}Po calibration sources in Monte Carlo, TPC H, and TPC V, shown in Figure 5.17, is calculated separately and shown in the second column of the table. The third column shows the ratio of the obtained mean in each TPC to the mean calculated from the Monte Carlo simulation. This ratio is then used as a multiplicative correction to the detected recoil energies presented in Chapter 6.

	Average dQ/dx [e/µm]	Correction Factor
Simulation	3227	1.0
TPC H	2647	1.22
TPC V	2051	1.57

effective gain of the simulated TPC. To do this, an average between the two peaks for a given TPC is then obtained to provide one measurement of dQ/dx for alphas events drifting a length halfway between the two calibration sources. A calibration coefficient for the TPC is obtained by taking the ratio of the average in experimental data to the average in simulated data. We then use this factor as a multiplicative correction for all charge measurements of events. A table of the values for the mean dQ/dx for the two sources in the two TPCs in Figure 5.17 is shown in Table 5.5[†]. To measure the effect these corrections have on the detected recoil energy spectra, we plot the histograms of the true recoil energy obtained from the simulation alongside the uncorrected and corrected versions of the reconstructed recoil energy for helium events. This is shown in Figure 5.18. Here we see that the this calibration procedure produces an energy spectrum in much better agreement with the true recoil energies than the uncorrected recoil energy spectrum. We can also validate this method after obtaining a sufficient sample of Monte Carlo and experimental data samples of nuclear recoils after applying event selections, which is the basis of the next section.

[†]This is the same procedure as in Ref. [25], a work we have previously published. However, the results presented in this dissertation make use of the charge-loss corrections presented earlier, whereas no such corrections were done in Ref. [25].

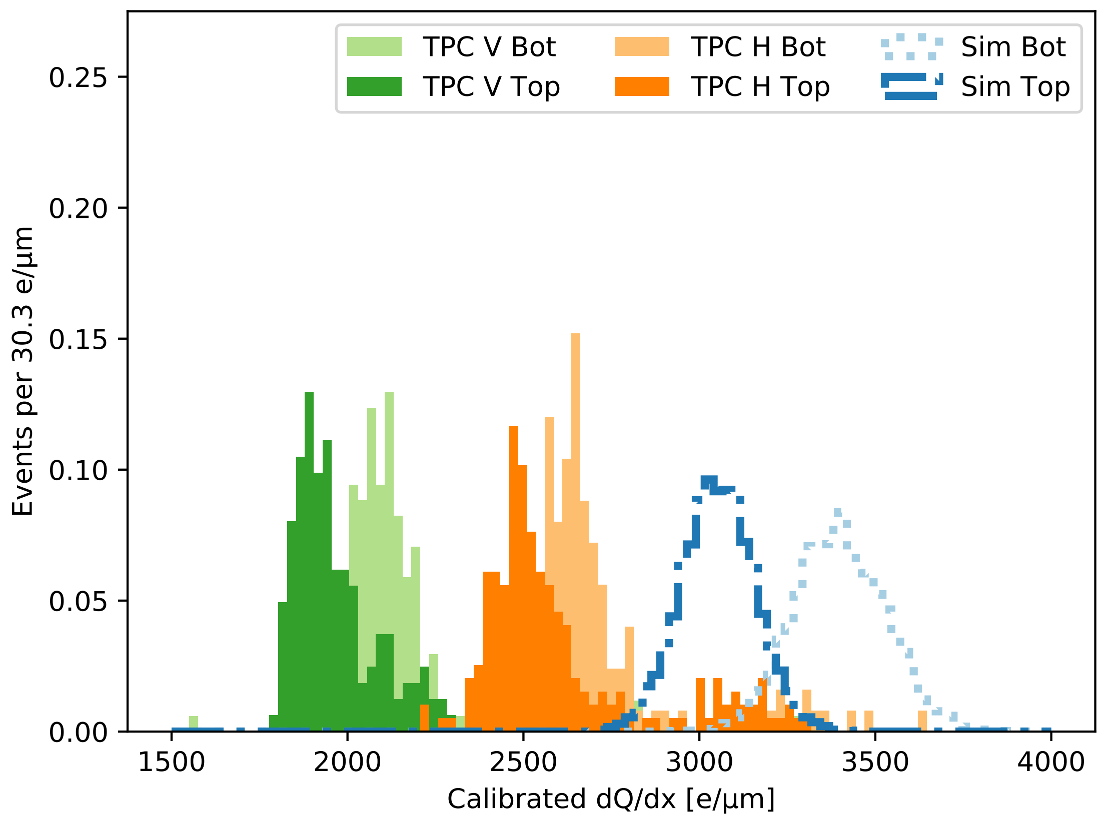

Figure 5.17: Histograms of the reconstructed detected charge divided by track length after correcting for pixel saturation and charge below the pixel threshold, via the fitted unction shown in Figures 5.13 and 5.16, respectively, for events from internal ^{210}Po calibration alpha sources in experimental and Monte Carlo data. The vertical axis shows the total number of events from both sources, normalized to 1, for TPC H, TPC V, and Monte Carlo separately.

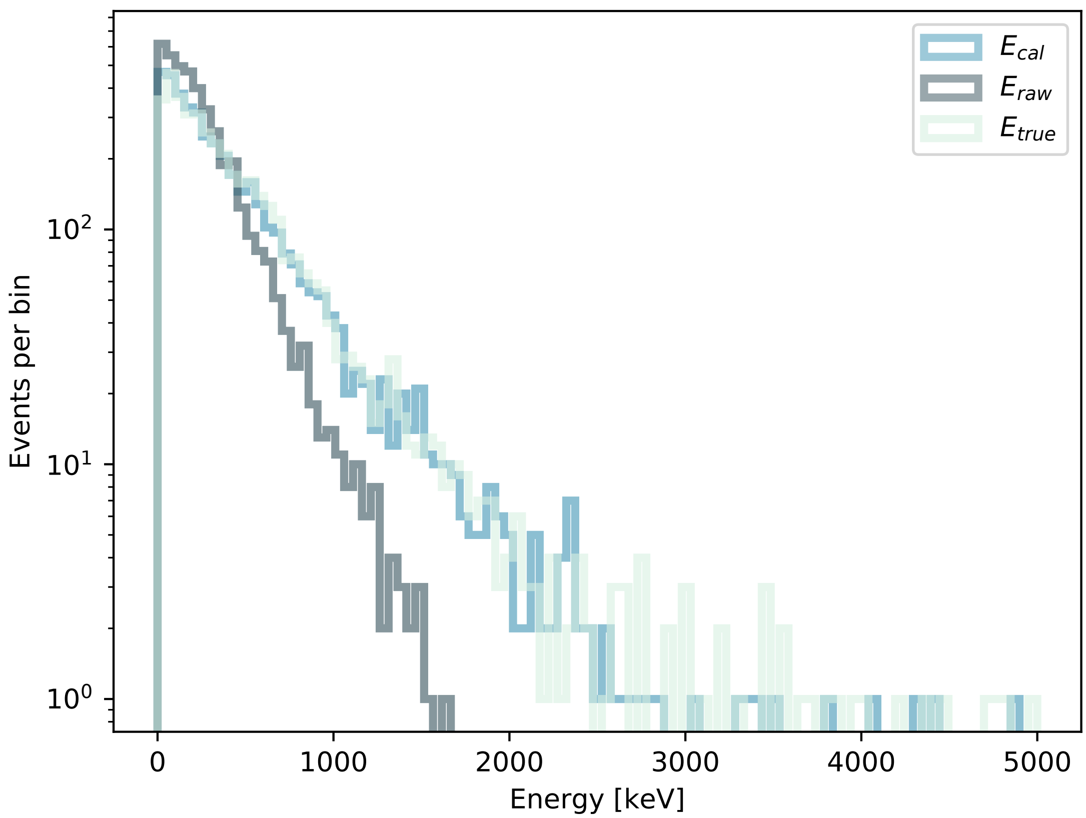

Figure 5.18: Histograms of the reconstructed energy compared to the true energy of helium recoils in simulated data. The line of darkest color corresponds to the corrected energy values, and the line of lightest color corresponds to the true energy. The last shade corresponds to the uncorrected energy values.

5.4 Background rejection

In order to obtain a clean nuclear recoil signal, it is necessary to reject background events. The following selections are applied to reject background events—a fiducial volume "edge veto," which requires no pixels triggered within 500 µm of the four outer edges of the pixel chip in order to veto tracks, including tracks from the calibration alpha sources, originating from outside the fiducial volume; the fitting algorithm used to fit the event to a straight line must converge so that the track length can be properly calculated; and the ratio of calibrated detected energy to track length (dE/dx) is greater than 40 eV/µm, removing electron recoil events and minimum ionization particles. We use a "corrected" length defined as:

$$L_C = L_{RAW} - w \tag{5.1}$$

where:

- L_{RAW} is the "raw" 3D length of the track, calculated by projecting the pixel coordinates along the fitted track axis and returning the 3D distance between the two points of largest mutual projected-distance.

- w is the *width* of the track, defined as the magnitude of the vector product of the unit vector along the z axis with the reconstructed track vector of magnitude L_{RAW}.

Furthermore, we implement a firmware veto that effectively rejects events with low energies in order to reject a majority of electron backgrounds. While electrons are easy to reject at the analysis level, triggering on many such events can lead to significant detector dead-time. The veto rejects events with a "trigger length" smaller than a configurable threshold. The trigger length of an event corresponds to the total length of time from when the integrated charge in any pixel is first larger than its threshold until the measured charge on all pixels is under threshold. The veto rejects events where the trigger length is less than a set length. We expect that an electron event will have significantly shorter trigger length than a nuclear recoil, because a nuclear recoil will have a far larger charge density per pixel than an electron event. The veto was tuned to reject electron events while accepting events from nuclear recoils [25].

The effectiveness of these selections are tested with a sample of 13011 Monte Carlo events generated for the accelerator induced fast-neutron analyses presented in Chapter 6. Detailed presentation and discussion of the simulation package can be found in Ref. [24]. The signal Monte Carlo sample consists of recoiling helium, carbon, and oxygen nuclei as

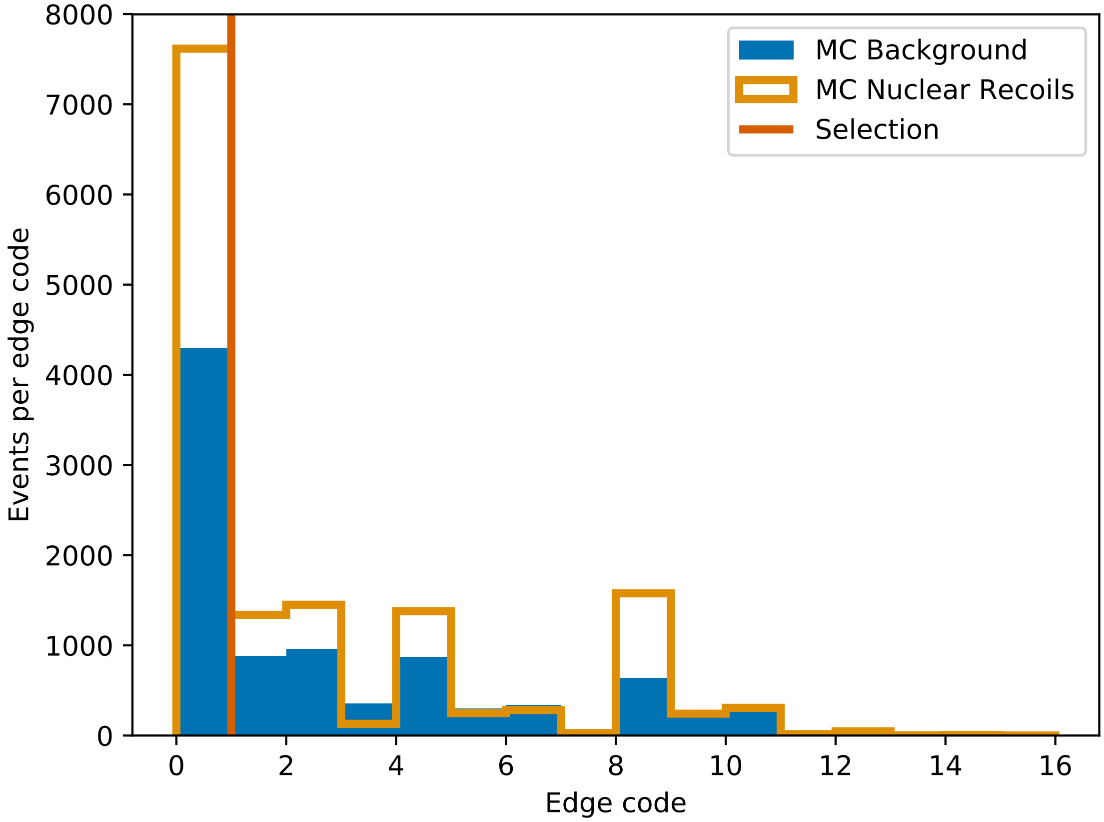

Figure 5.19: Recorded edge code in events in Monte Carlo signal and background data. An edge code of zero corresponds to the applied fiducialization selection, indicated by the vertical line. All other codes represent one or more edges of the pixel chip triggered in an event and are vetoed.

well as protons produced by fast neutron scattering. The background Monte Carlo sample consists of electrons, positrons, and photons.

The effect of applying the edge veto is shown graphically in Figure 5.19. This figure shows the proportion of signal and background Monte Carlo events that are selected and rejected by implementing this veto. 52.29% of signal events and 22.14% of background events remain with this selection. Given that this selection is implemented in order to fully reconstruct the energy information of a given recoil event, we accept these efficiencies without attempting to optimize further.

After applying these selections to experimental and Monte Carlo data and applying the relevant gain correction factor obtained in Table 5.5, the dE/dx of both data sets can be plotted simultaneously to check for agreement. This is shown in Figure 5.20. This distribution is also shown with a focus on low energy and short length tracks in Figure 5.21. These figures show that there is not only a clear separation of signal recoils from electron and proton backgrounds, but that there is also clear separation between helium recoils and carbon and oxygen recoils. However, it is also clear that the energy calibration and correction procedure result in a difference between experimental and Monte Carlo data. Specifically, Figures 5.20 and 5.21 show that the amount of detected energy in experimental data is underestimated in both the helium and carbon and oxygen bands. We find that an additional increase of 20% in the detected energy results in better agreement between simulated and detected helium events. Applying this 20% increase to events in experimental data is shown in Figures 5.22 and 5.23, where it is immediately apparent that agreement between the Monte Carlo (blue) and experimental (black) helium bands are in overall better, but not perfect, agreement. We speculate that this 20% correction is needed in order to account for possible discrepancies in the modeling of the charge digitization in the simulated data. While the agreement in helium improves with this factor, there is still noticeable disagreement in the carbon and oxygen band. We conclude that with this procedure, agreement can be obtained for either helium or carbon and oxygen events in experimental and Monte Carlo data, but not both simultaneously.

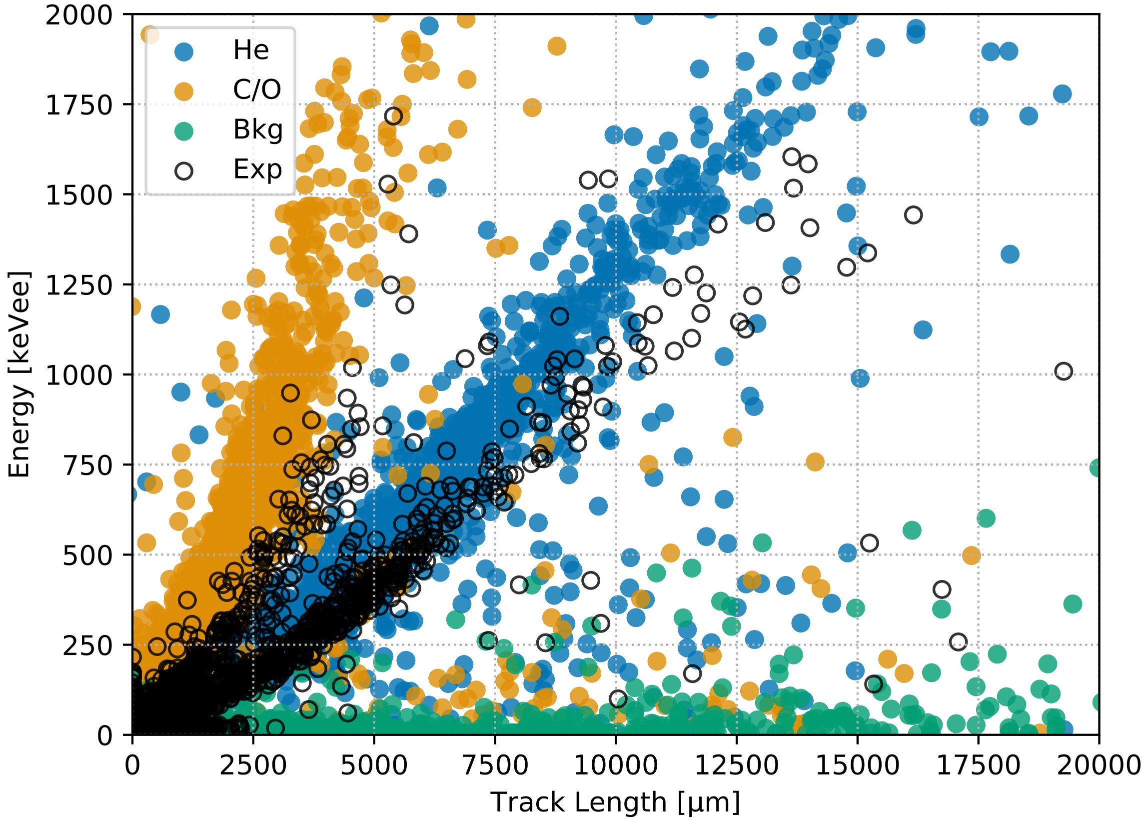

Figure 5.20: TPC recoil charge versus recoil length for fiducially selected events in TPCs H and V, for both Monte Carlo and experimental data, combined. This includes applying the gain correction factors in Table 5.5 to each TPC. The blue, orange, and green filled circles represent helium recoils, carbon/oxygen recoils, and proton backgrounds in Monte Carlo, respectively. The open black circles represent the events in experimental data that pass the fiducialization selection.

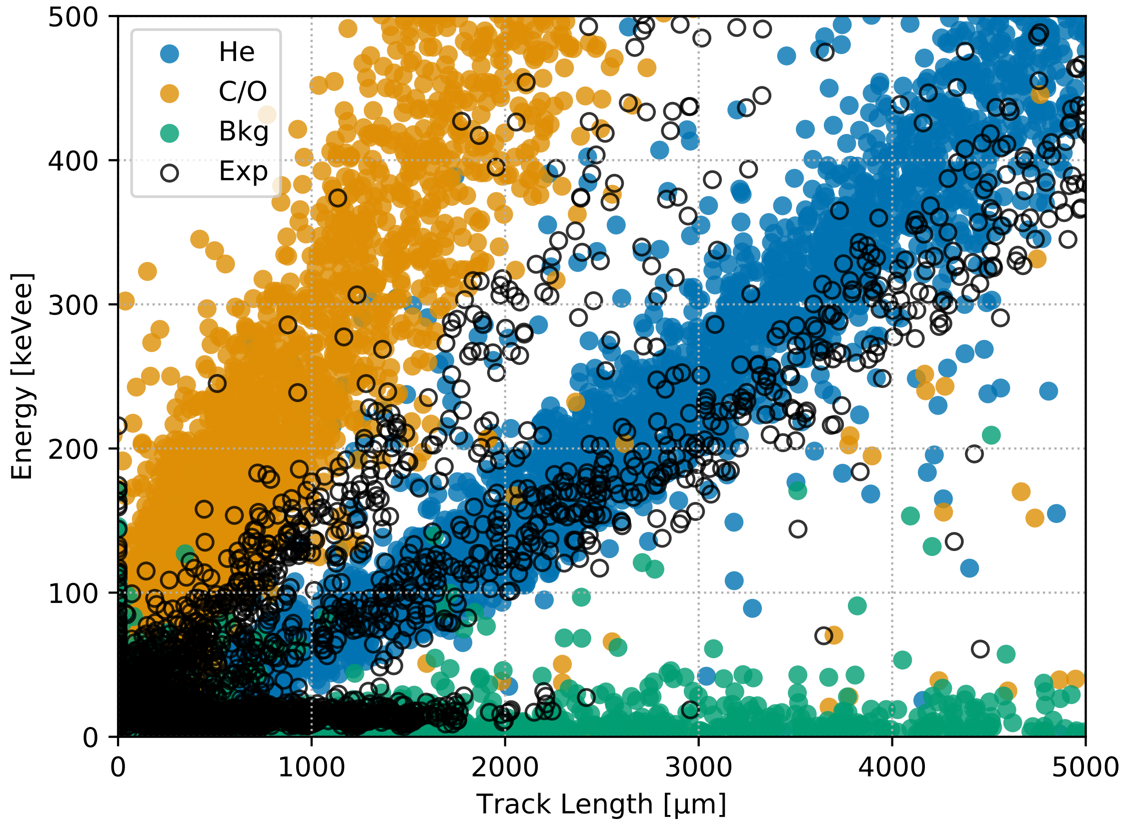

Figure 5.21: TPC recoil energy versus recoil length, as shown in Figure 5.20, with a focus on low energy and short length events.

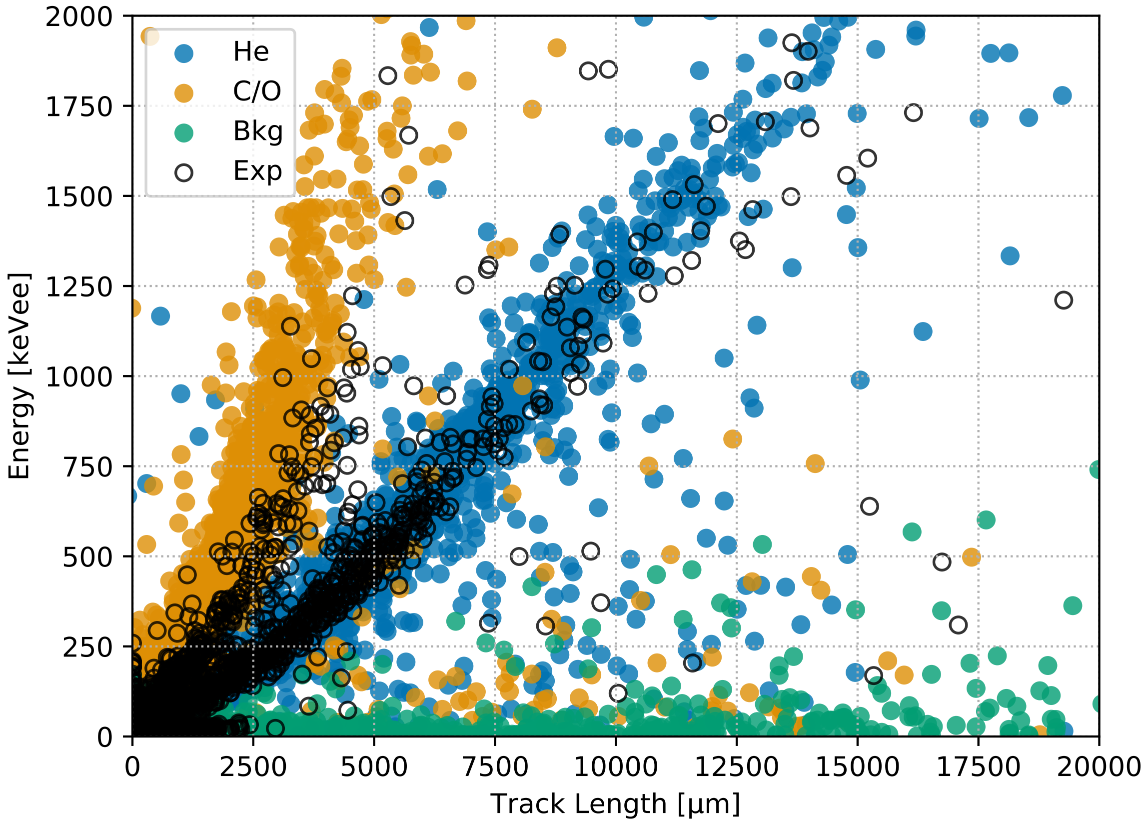

Figure 5.22: TPC recoil charge versus recoil length for fiducially selected events in TPCs H and V, for both Monte Carlo and experimental data, combined. This includes applying the gain correction factors in Table 5.5 to each TPC and an additional correction factor of 1.2 in order to align the helium bands in Monte Carlo and experimental data. The blue, orange, and green filled circles represent helium recoils, carbon/oxygen recoils, and proton backgrounds in Monte Carlo, respectively. The open black circles represent the events in experimental data that pass the fiducialization selection.

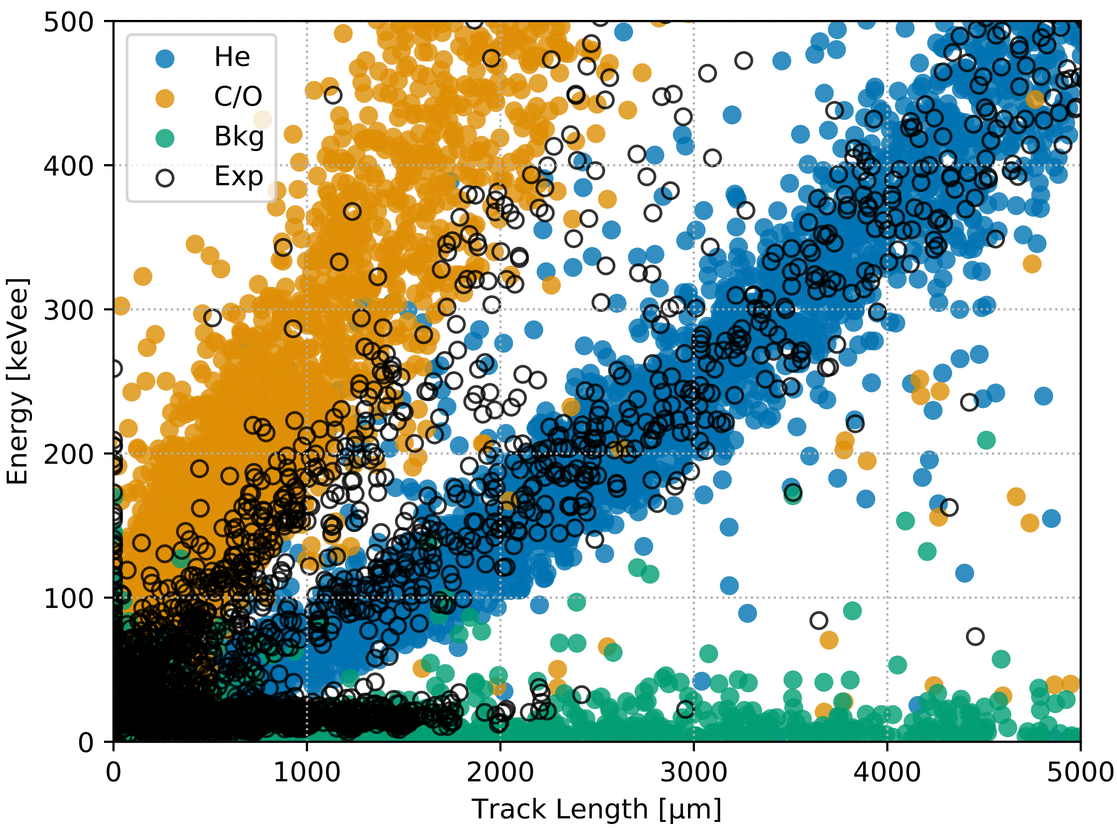

Figure 5.23: Corrected TPC recoil energy versus recoil length, as shown in Figure 5.22, with a focus on low energy and short length events.

From these figures, it can be seen that separation from signal and background should be possible based on a selection of dE/dx. In order to optimize this selection, we look specifically at the *efficiency*, ϵ, and *purity*, p, of selecting events based on a given value of dE/dx in the Monte Carlo. Here, ϵ is defined such that:

$$\epsilon = \frac{N_{sel}^{SIG}}{N_T^{SIG}} \tag{5.2}$$

where:

- N_{sel}^{SIG} is the number of *selected* signal events using the applied selection.
- N_T^{SIG} is the *total* number of signal events in the Monte Carlo sample.

The purity is defined such that:

$$p = \frac{N_{sel}^{SIG}}{N_T^{all}} \tag{5.3}$$

where:

- N_T^{ALL} is the amount of *all*—signal plus background—events in the Monte Carlo sample.

For a single value of dE/dx, we calculate the efficiency and purity at a certain minimum energy and define N^{SIG} to be the sum of helium, carbon, and oxygen recoils. The energy values scanned over span from 1–100 keV. This process traces out a curve in p versus ϵ space. This is shown in Figure 5.24. In this plot, a perfect selection would correspond to $\epsilon = p = 1$. In Figure 5.25, we restrict the axes limits to better see the region near unity and find that the optimal selection corresponds to $dE/dx > 20$ eV/µm at a minimum energy of 20 keV. Additionally, ϵ and p are shown separately versus energy in Figures 5.26 and 5.28, respectively. The same plots with axes limits near unity are shown in Figures 5.27 and 5.29, respectively. As expected, p increases with increasing energy and increasing dE/dx, and the ϵ decreases with increasing energy and increasing dE/dx.

To validate this selection, we can view the energy versus length plot specifically at the low energy and short length regime. As the background and helium bands are clearly visible, this check should determine if the dE/dx selection and/or an additional energy threshold should be applied to improve background rejection performance. By doing so, we find that a selection of $dE/dx > 0.04$ keV/µm with an energy threshold of 50 keV provides a cleaner background rejection criteria. This is shown in Figures 5.30 and 5.31. We note that there

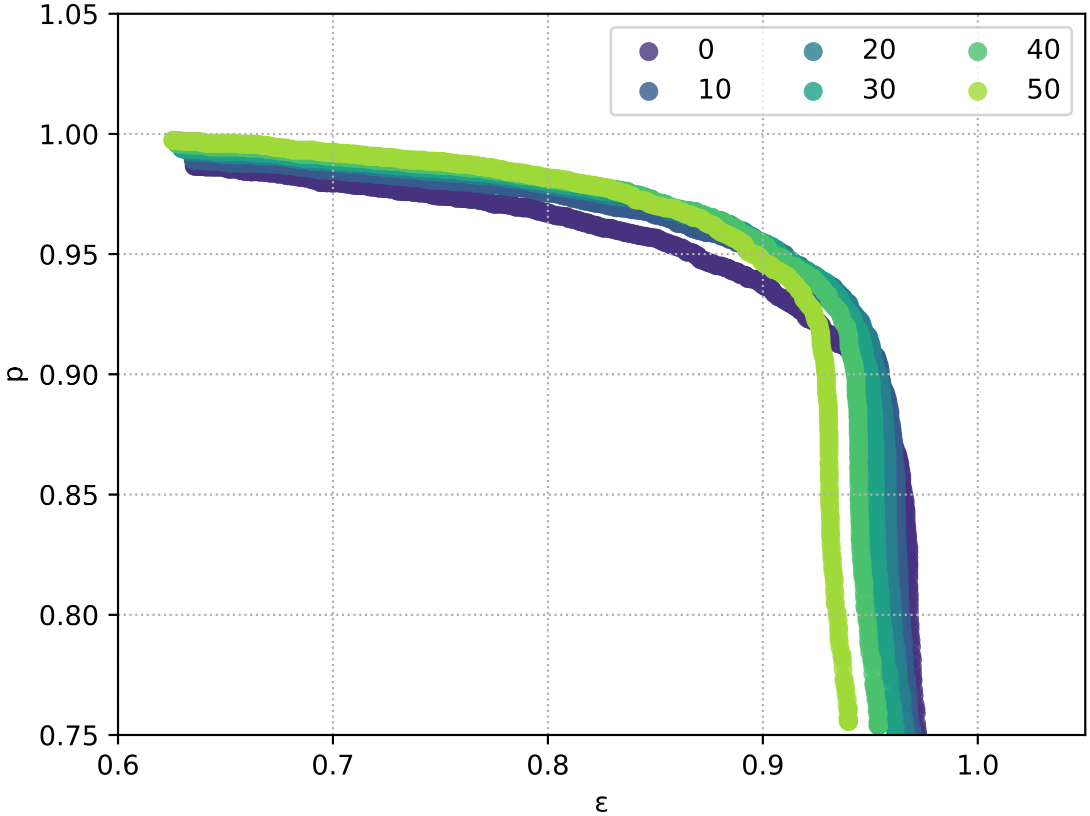

Figure 5.24: Efficiency versus purity of various values for the lower bound on the dE/dx selection for helium recoils. Each point corresponds to the purity and efficiency of nuclear recoils for a given minimum dE/dx (indicated by color) and above a minimum energy. The optimal selection corresponds to dE/dx greater than 20.0 eV/µm and detected recoil energy greater than 20 keV.

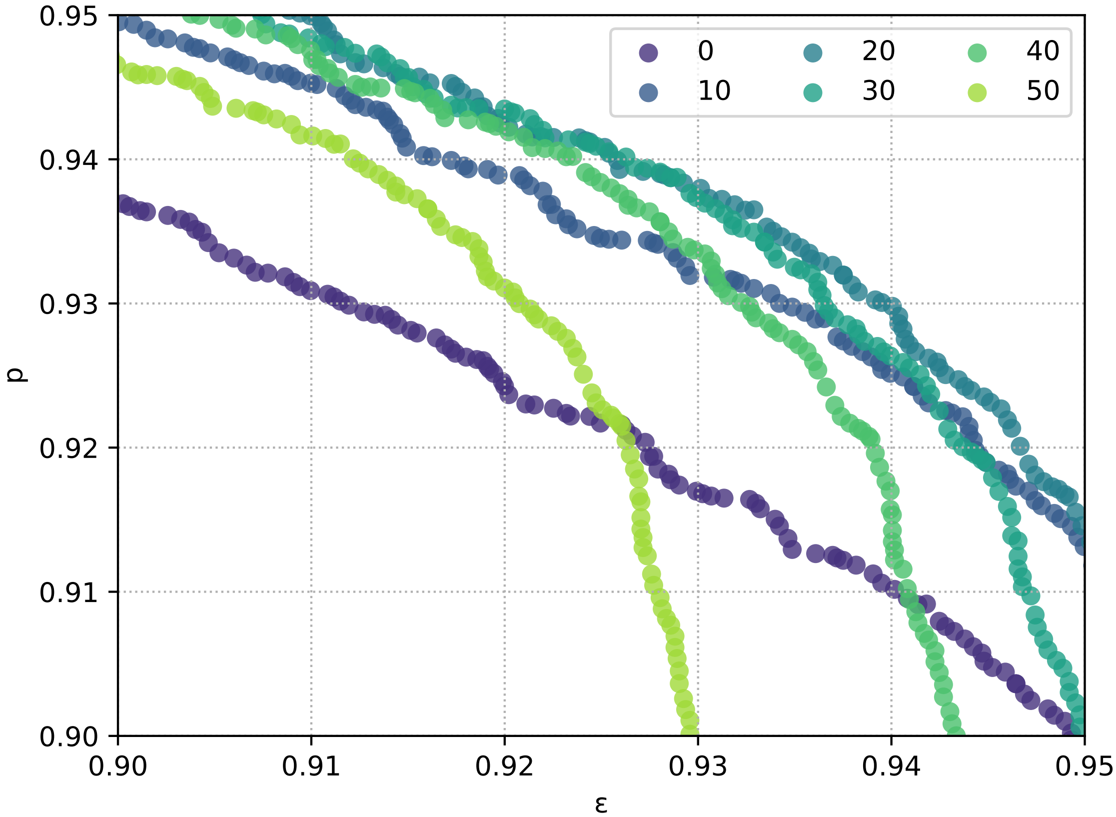

Figure 5.25: A tighter view of Figure 5.24 near the point of maximal efficiency and purity for the lower bound on the dE/dx selection for nuclear recoils.

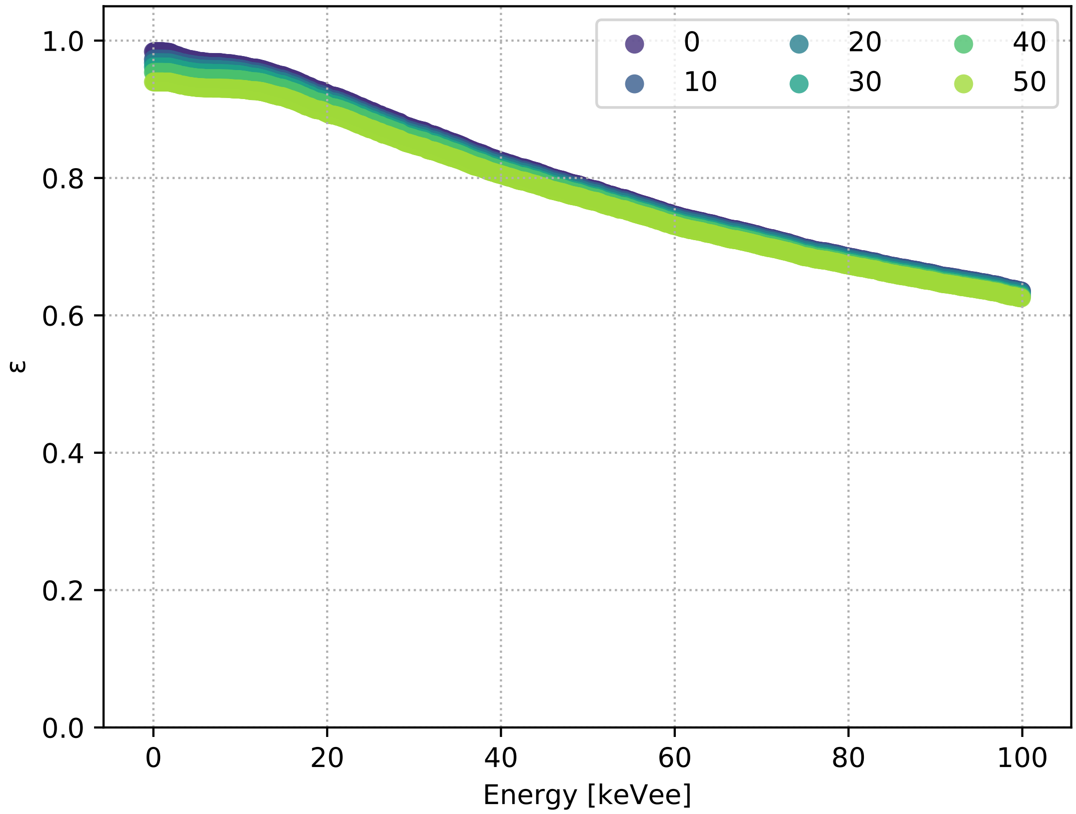

Figure 5.26: Efficiency versus energy of various values for the lower bound on the dE/dx selection for helium recoils. Each point corresponds to the purity and efficiency of nuclear recoils for a given minimum dE/dx (indicated by color) and above a minimum energy. The optimal selection corresponds to dE/dx greater than 20.0 eV/µm and detected recoil energy greater than 20 keV.

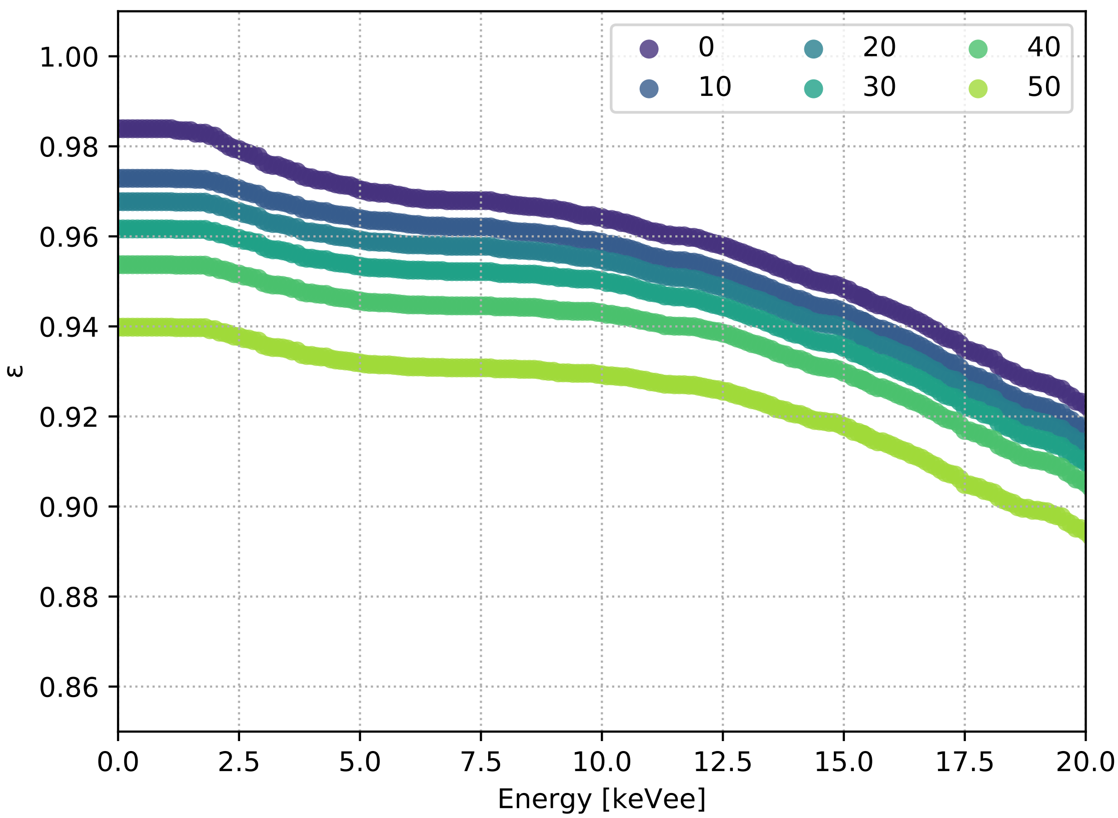

Figure 5.27: Efficiency versus energy of various values for the lower bound on the dE/dx selection for helium recoils, as shown in Figure 5.26, with axes limits to focus in where the efficiency gets nearest to unity.

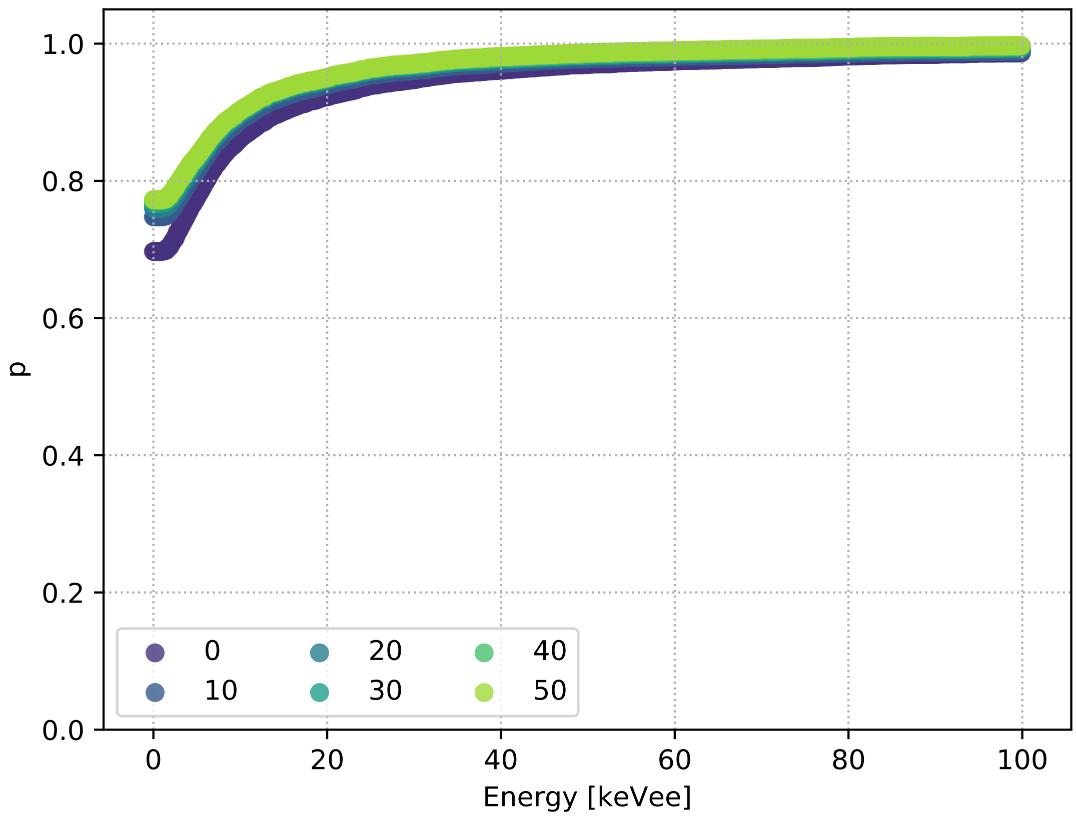

Figure 5.28: Purity versus energy of various values for the lower bound on the dE/dx selection for nuclear recoils. Each point corresponds to the purity and efficiency of helium recoils for a given minimum dE/dx (indicated by color) and above a minimum energy. The optimal selection corresponds to dE/dx greater than 20.0 eV/µm and detected recoil energy greater than 20 keV.

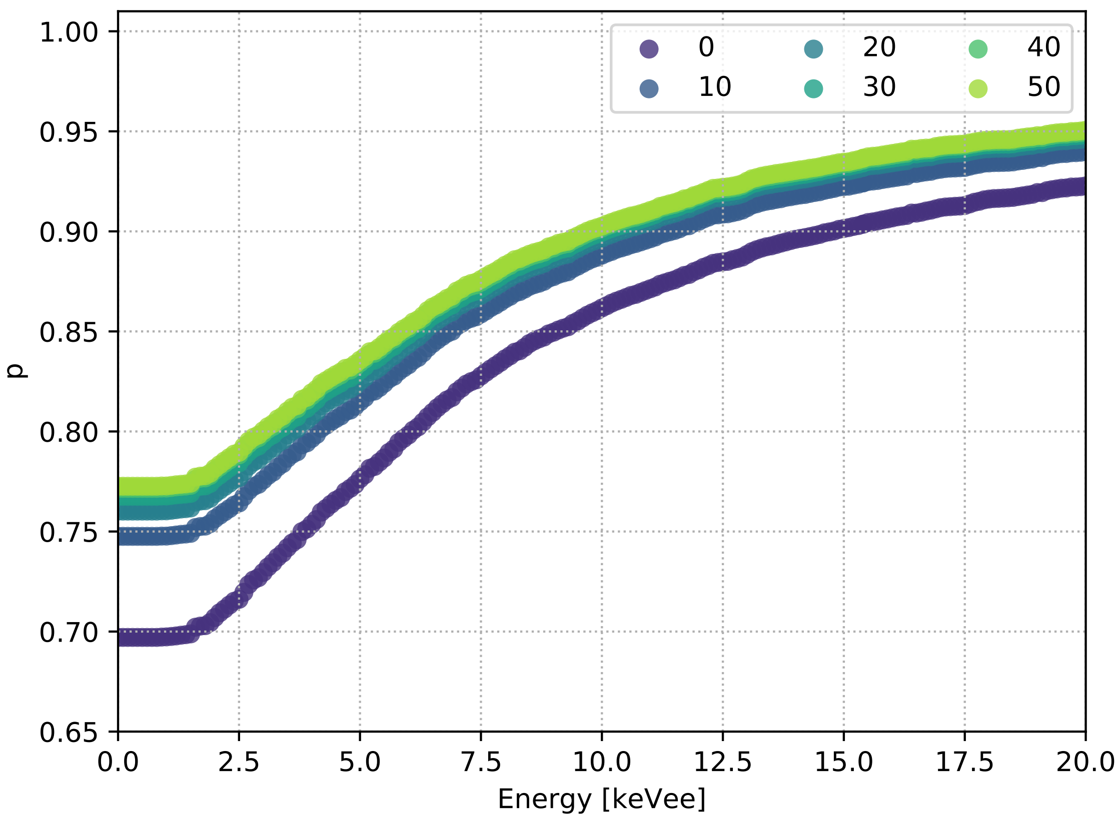

Figure 5.29: Efficiency versus energy of various values for the lower bound on the dE/dx selection for nuclear recoils, as shown in Figure 5.28, with axes limits to focus in where the efficiency gets nearest to unity.

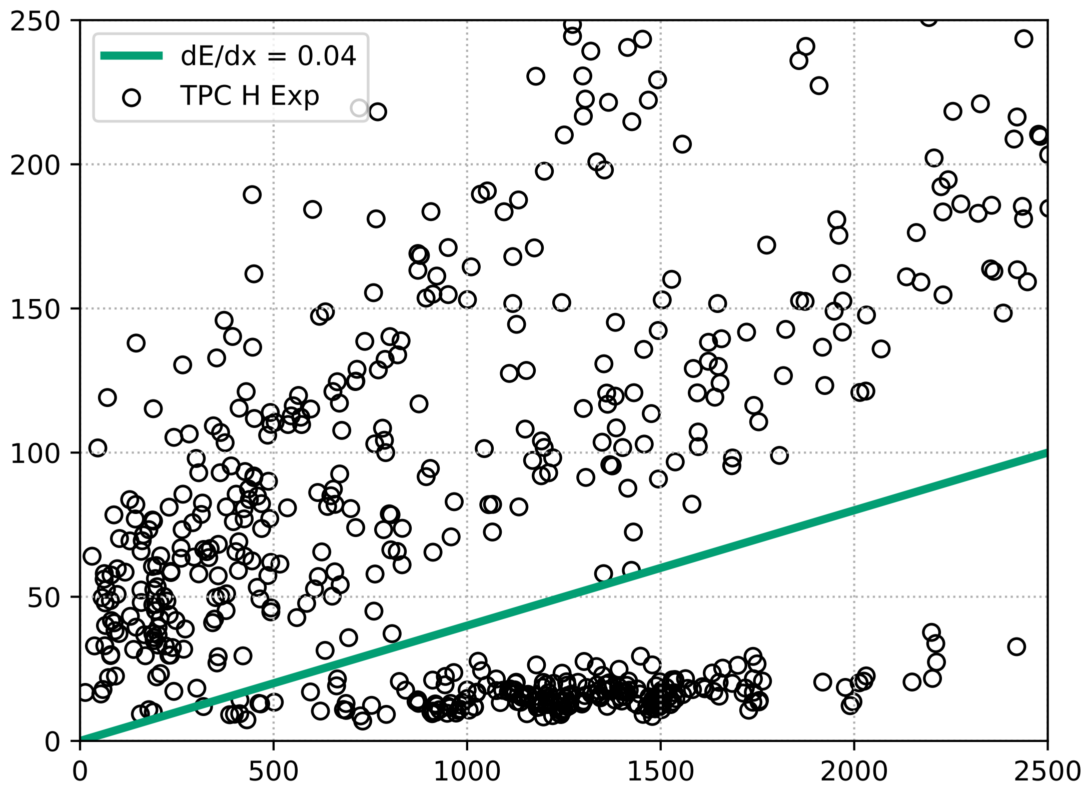

Figure 5.30: Energy versus length for all events that pass the fiducialization selection in TPC H. The green line shows the boundary of a selection of $dE/dx > 0.04$ keV/µm.

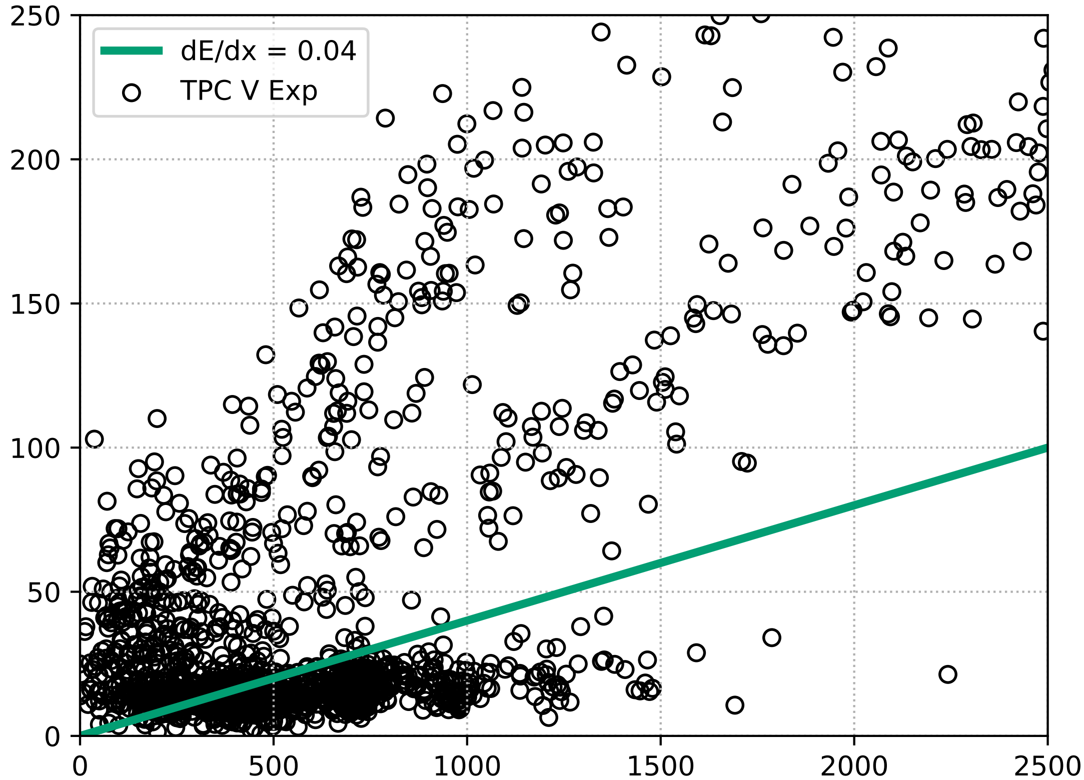

Figure 5.31: Energy versus length for all events that pass the fiducialization selection in TPC V. The green line shows the boundary of a selection of $dE/dx > 0.04$ keV/µm.

are significantly more background events in TPC V. We speculate that this is due to either a mistaken setting or improper performance of the firmware-level background veto.

This same procedure can be used to select an upper dE/dx to discriminate carbon and oxygen recoils from helium recoils. This is performed similarly to finding the lower dE/dx bound, with the exception that each point corresponds to a selection above a minimum and below a maximum value of dE/dx. Furthermore, for this analysis, N^{SIG} corresponds to helium recoils only. From the previous analysis, we choose the lower bound to be $dE/dx >$ 0.02 keV/µm, and we scan the upper limit using a range of minimum recoil energies from 1–100 keV, as before. The efficiency versus energy for five values of dE/dx is shown in Figure 5.32, and the purity versus energy for the same values is shown in Figure 5.33. Finally, the efficiency versus purity is shown in Figure 5.34, with a focus on the section of maximal efficiency and purity in Figure 5.35. We find that optimal efficiency and purity is reached by selecting events below 162 eV/µm with a detected recoil energy greater than 28 keV.

To gauge the effect of our event selection on the recoil energy spectrum, which is one of our final observables, we can calculate the efficiency of event selection criteria as the fraction of events passing the edge veto and the minimum dE/dx selection in experimental data. This efficiency versus energy serves to determine which nuclear recoil energies we are sensitive to and whether the selections bias the observed energy spectrum. This efficiency is shown in Figure 5.36. The efficiency becomes 50% at approximately 30 keV and is near unity and flat for recoil energies larger than $\sim$ 65 keV.

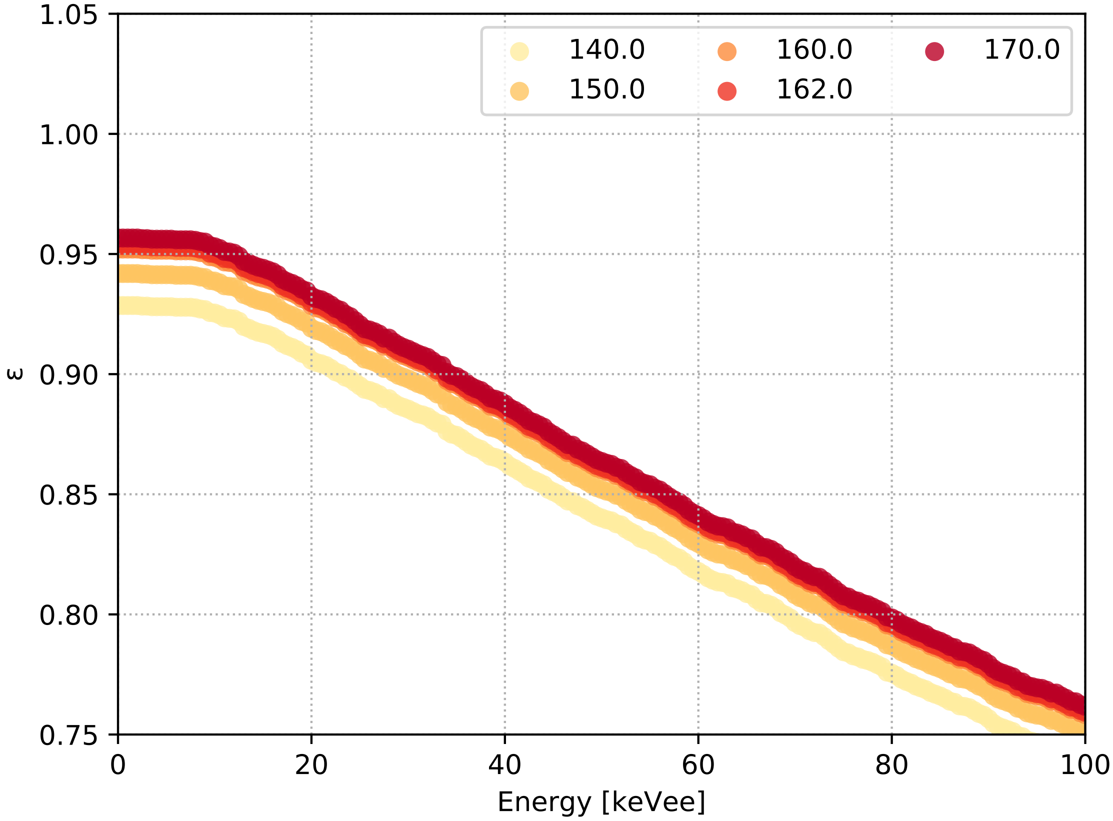

Figure 5.32: Efficiency versus energy of various values for the upper bound on the dE/dx selection for helium recoils. Each point corresponds to the purity and efficiency of helium recoils for a given minimum dE/dx (indicated by color) and above a minimum energy. The optimal selection corresponds to dE/dx less than 162 eV/µm and detected recoil energy greater than 28 keV.

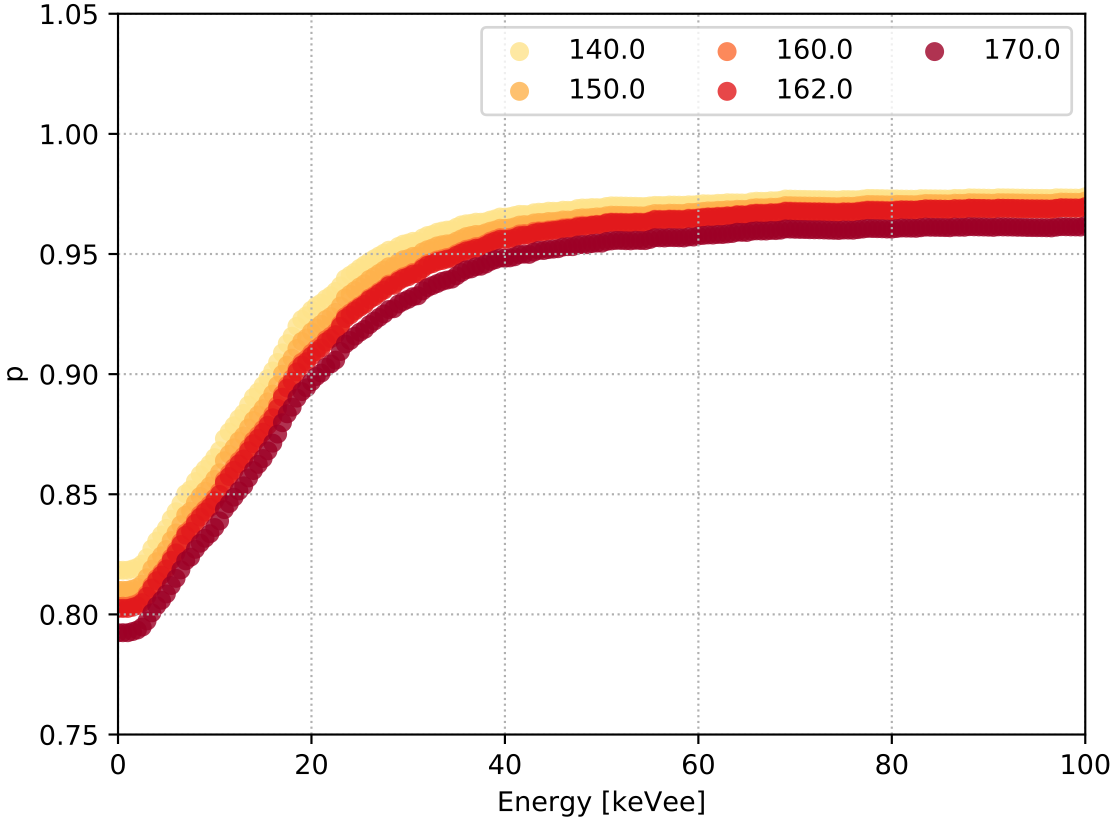

Figure 5.33: Purity versus energy of various values for the upper bound on the dE/dx selection for helium recoils. Each point corresponds to the purity and efficiency of helium recoils for a given minimum dE/dx (indicated by color) and above a minimum energy. The optimal selection corresponds to dE/dx less than 162 eV/µm and detected recoil energy greater than 28 keV.

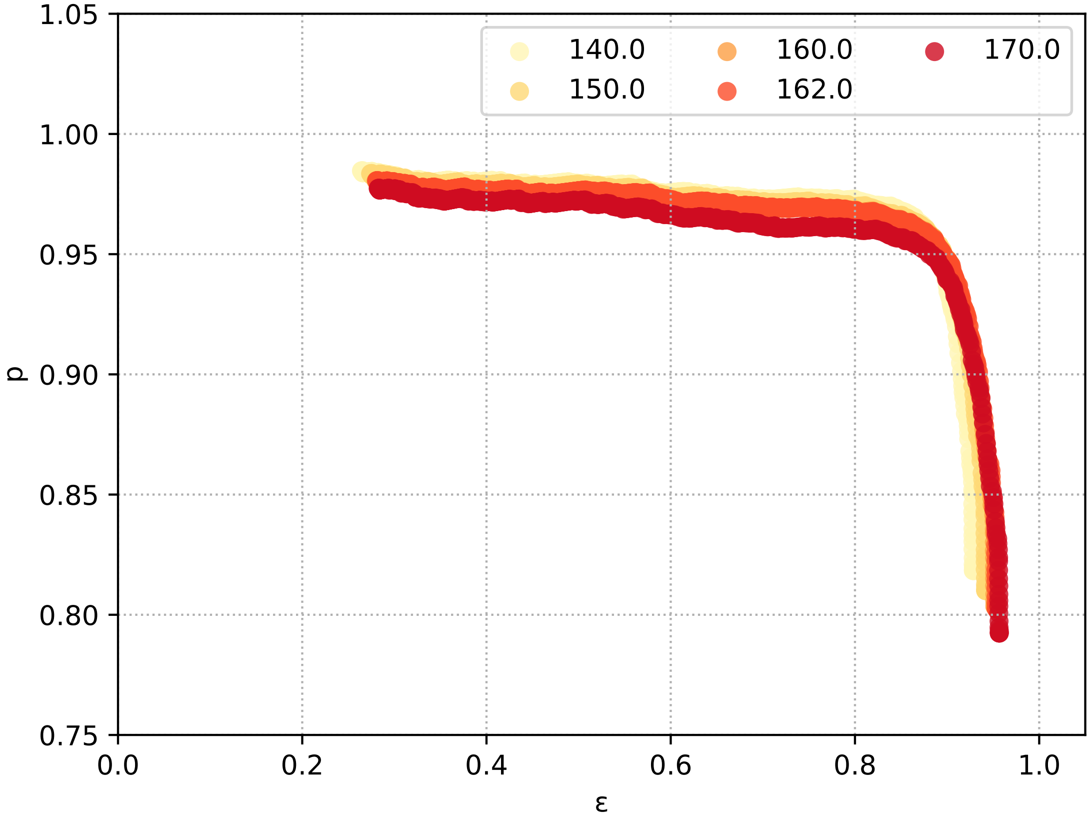

Figure 5.34: Efficiency versus purity of various values for the upper bound on the dE/dx selection for helium recoils. Each point corresponds to the purity and efficiency of helium recoils for a given maximum dE/dx (indicated by color) and above a minimum energy. The optimal selection corresponds to dE/dx less than 162 eV/µm and detected recoil energy greater than 28 keV.

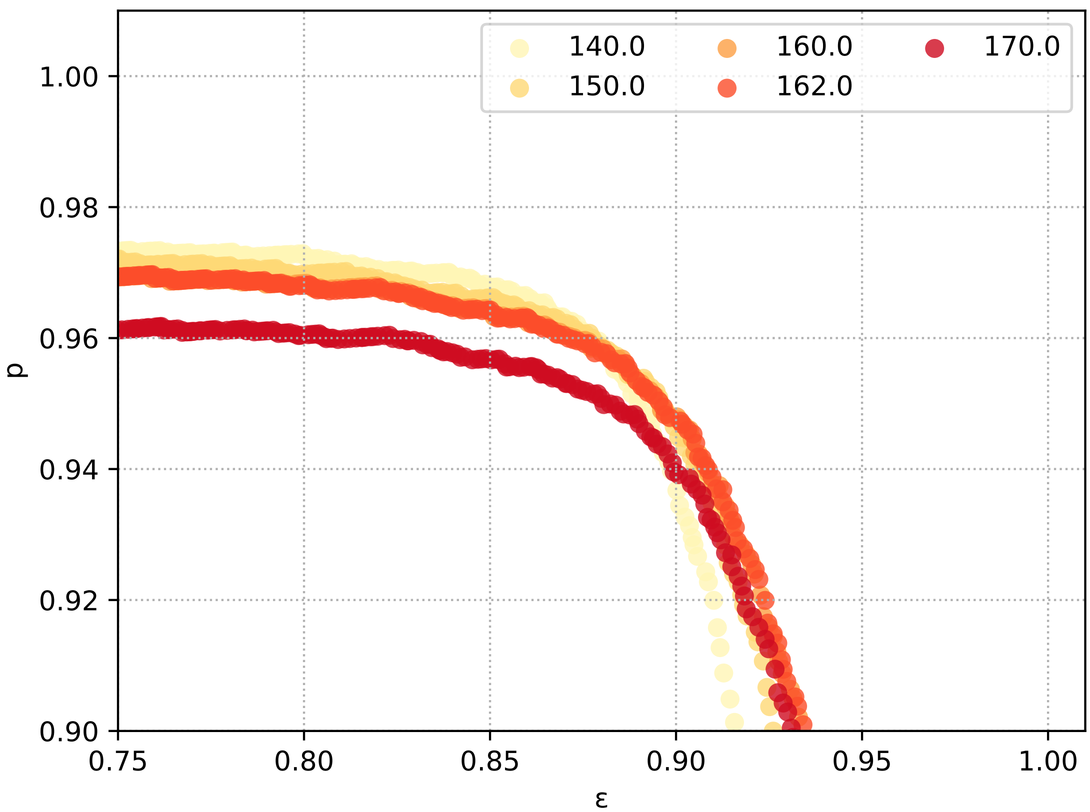

Figure 5.35: A zero-suppressed view of Figure 5.34 near the point of maximal efficiency and purity for the upper bound on the dE/dx selection for helium recoils.

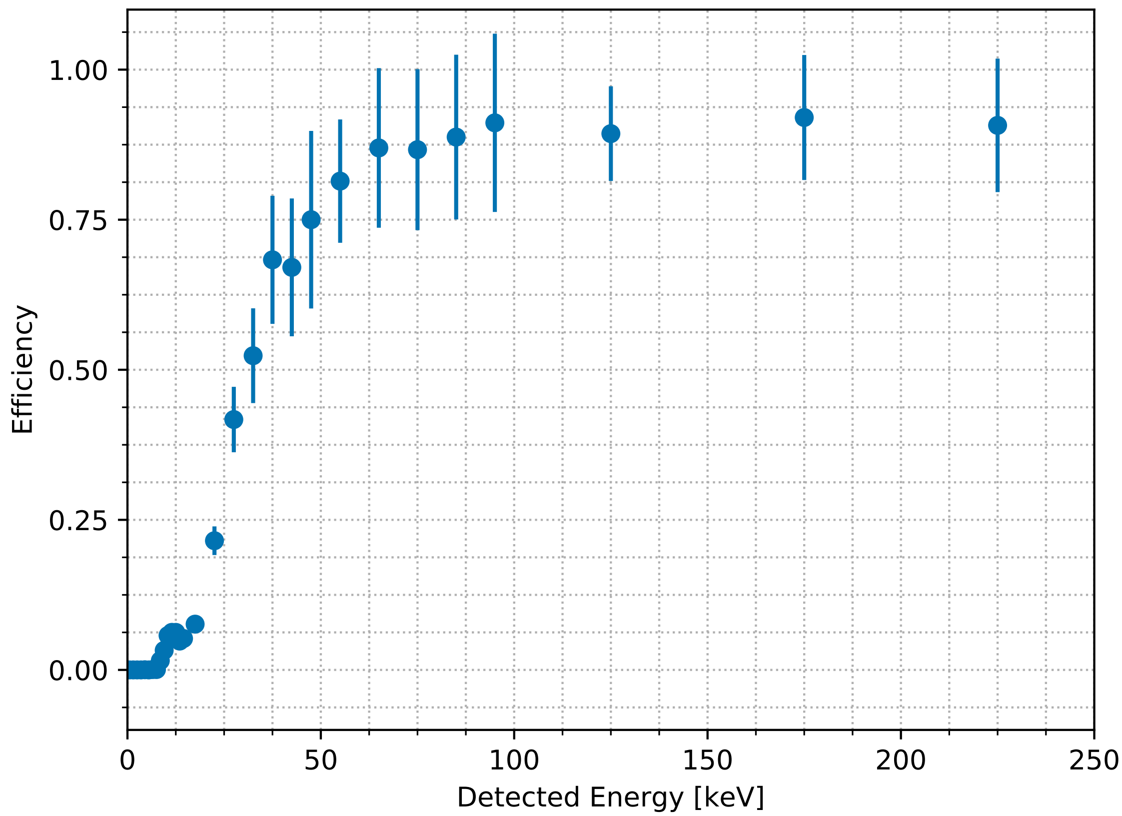

Figure 5.36: Efficiency of TPC neutron selections described in Section 5.4 versus detected energy in experimental data. Efficiency of 50% occurs at approximately 30 keV. The unequal spacing between adjacent points is due to nonuniform bin sizing so that all bins have relatively similar statistical uncertainties. There are no bins with zero entries.

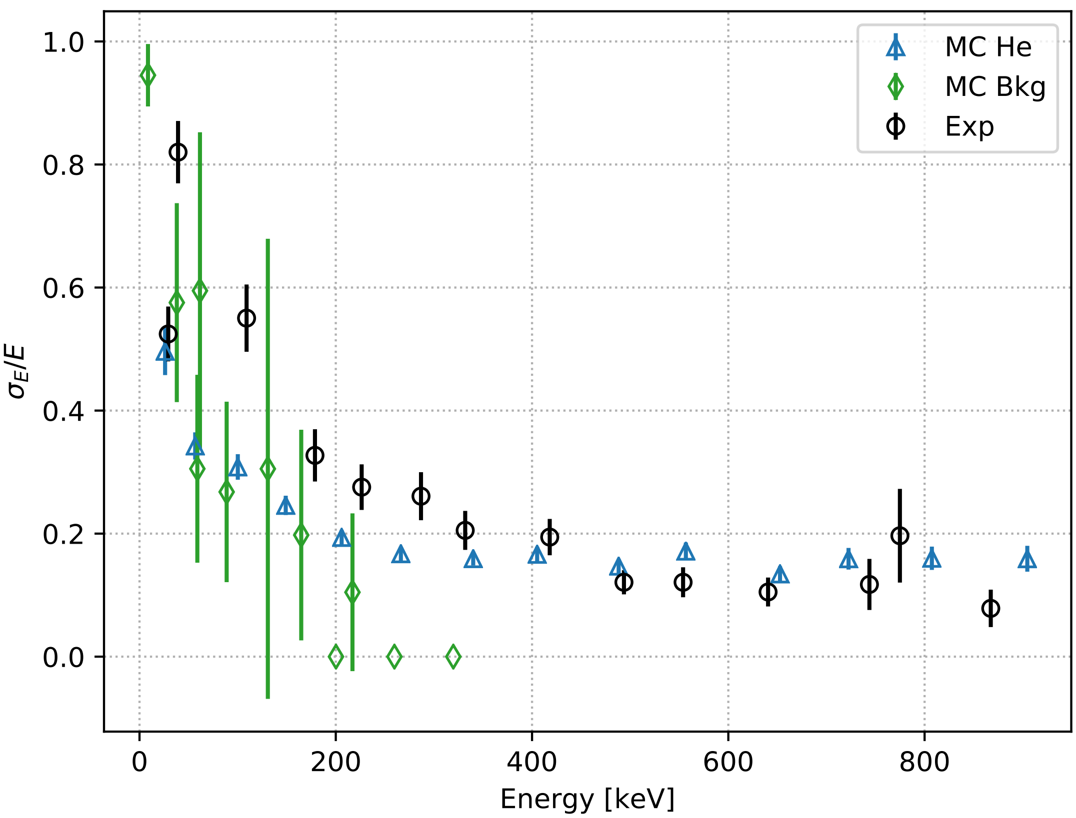

Figure 5.37: Fractional energy resolution versus energy in helium recoils.

5.5 Directionality

5.5.1 Axial directionality

In order to provide directional measurements of nuclear recoils, we must quantify the directional performance of the TPCs. This is done by finding a measure of the accuracy in which the TPCs and analysis can reconstruct the angular information about a track with respect to the true value available in Monte Carlo data, and how this resolution behaves versus detected event energy. Additionally, we aim to provide a measure of directional performance in a experimental data instead of relying purely on Monte Carlo data. Furthermore, we aim to provide 3D directional measurements, that is to quantify the performance of identifying the "sense," or the *head* and *tail* of a given track.

We begin by first measuring the accuracy of the reconstructed axis, or *axial directionality* of events. Using Monte Carlo data, we compare the 3D reconstructed track axis to the true track axis as provided by the Monte Carlo data by plotting the 3D angle between the two axes versus . Given that this is a test of axial directionality, the angle between the two axis cannot exceed 90°. Performing this measurement on many tracks serves as a measure of average of the *true axial mismeasurement* of the TPCs for an average track length.

In an attempt to find a method without relying on true Monte Carlo information, thus providing a means to quantify the axial mismeasurement in experimental data, we divide each track into halves, bisecting the track along the reconstructed track axis. We then reconstruct a track for axis each half independently and calculate the mean 3D angle difference between the two halves and divide by $sqrt(2)$ to account for the propagated error associated with two fits. We then plot this quantity versus the length of the halved, or *split*, track.

Figure 5.38 shows the results of the true axial mismeasurement and the intra-track mismeasurement in both Monte Carlo and experimental data versus length. Here, the horizontal coordinate in the measure of the true axial mismeasurement is the full length of the track, whereas the horizontal coordinate for the other points corresponds to the length of the "split track"—equal to half of the total track length. The same values versus reconstructed energy are shown in Figure 5.39.

From these figures, we find that the intra-track mismeasurement obtained from halving a single track does agree with the true mismeasurement in both Monte Carlo and experimental data at energies above 100 keV, with an average mismeasurement of approximately 20°.

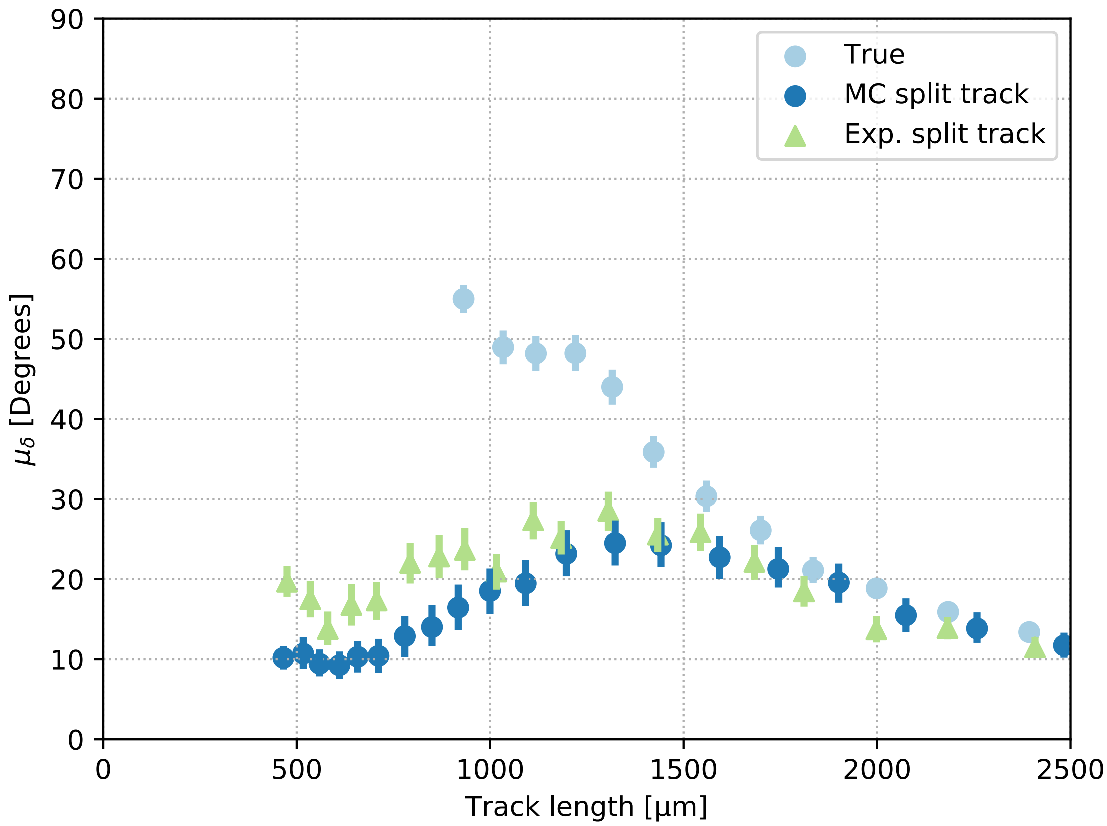

Figure 5.38: Angular resolution measured with true values in simulation and using the split-track method in experimental data versus track length.

5.5.2 Head/tail recognition

In order to perform 3D analyses, we must be able to infer the vector direction of a recoil. One method to do so is to consider the specific energy loss of the recoil. As shown in Figure 2.2, the specific energy loss can change drastically depending on the initial energy and distance travelled within a medium. However, the events we consider are those in which the entire path of the recoil is contained within the fiducial volume of the TPC. This means that, by definition, the specific energy loss of the event will lie at the end of the Bragg curve, corresponding to a sharp decline in the specific energy loss until the energy loss no longer activates pixels on the chip. Therefore, in principle, one should be able to identify the positive trajectory of the track, often referred to as the track's *head*, as the end with less detected energy.

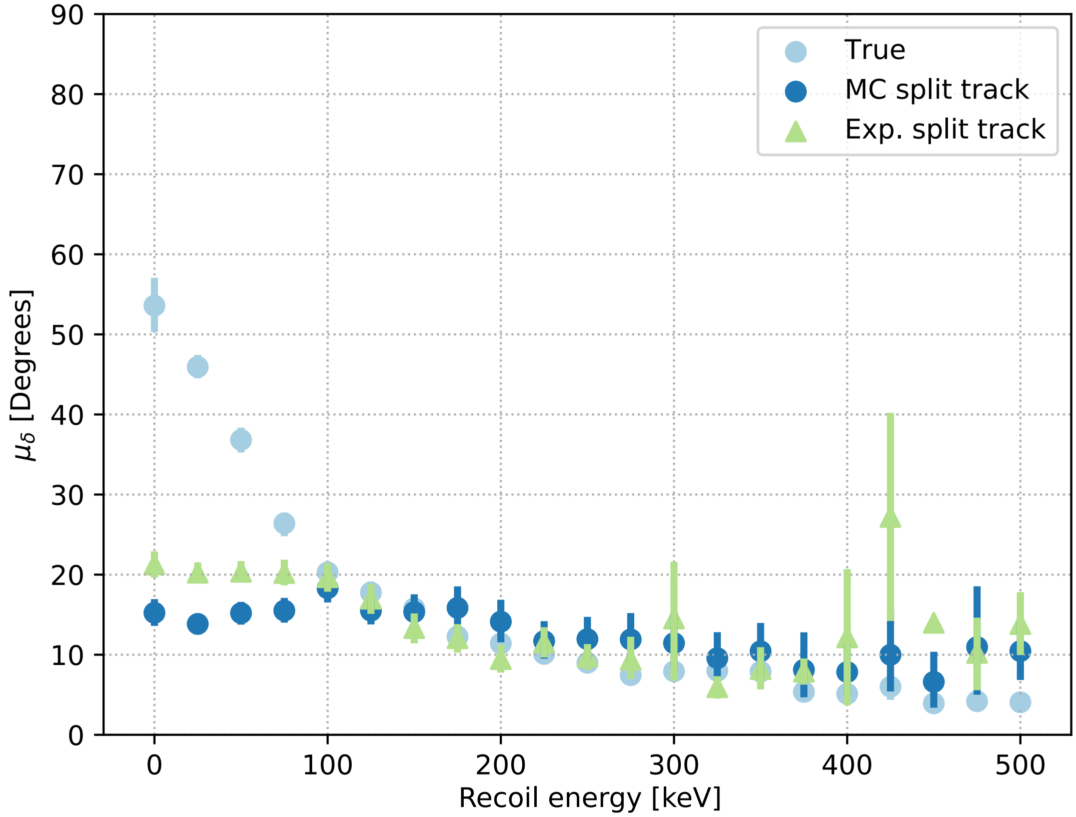

Figure 5.39: Angular resolution measured with true values in simulation and using the split-track method in experimental data versus detected energy.

To test this, we take the simple approach of dividing the track in two halves and use the truth information in the Monte Carlo data to plot the ratio of detected energy in the true head to the total amount of detected charge in an event. This is shown in Figures 5.40 and 5.41 for helium events and carbon and oxygen events, respectively. We note in these plots that the helium recoils exhibit the expected behavior—less than half of the detected charge, or energy, is found in the head, corresponding to a *head charge fraction* (HCF) of less than 0.5. For carbon and oxygen, however, the HCF distribution peaks at HCF = 0.5, meaning that the head of the track is, on average indistinguishable from the tail of the track. To investigate this further, we plot the HCF versus track length and versus energy in Figures 5.42 and 5.43, respectively. These figures show that HCF < 0.5 for helium recoils across a broad range of recoil energies, whereas HCF in carbon and oxygen is approximately 0.5 across the same range of recoil energies. Thus, we conclude that full 3D directionality using this method is only effective for helium recoils.

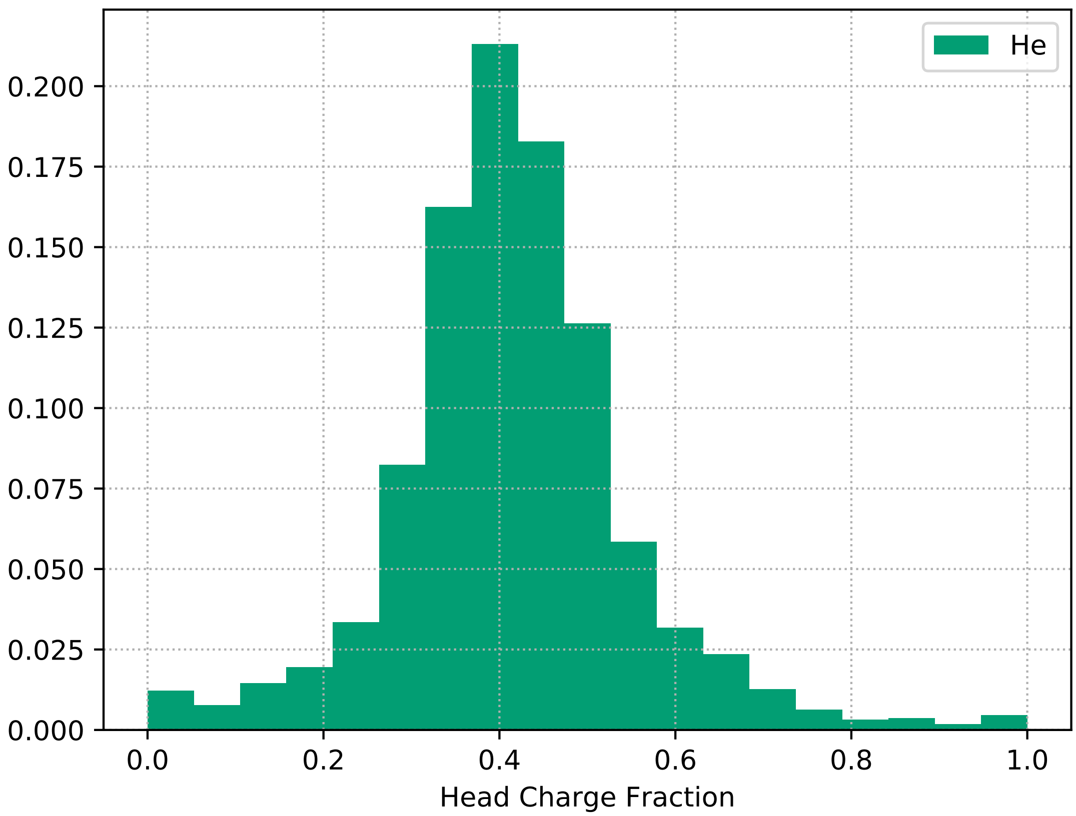

Figure 5.40: Fractional charge in the true head of helium events (green) and its mirrored distribution in TPC H.

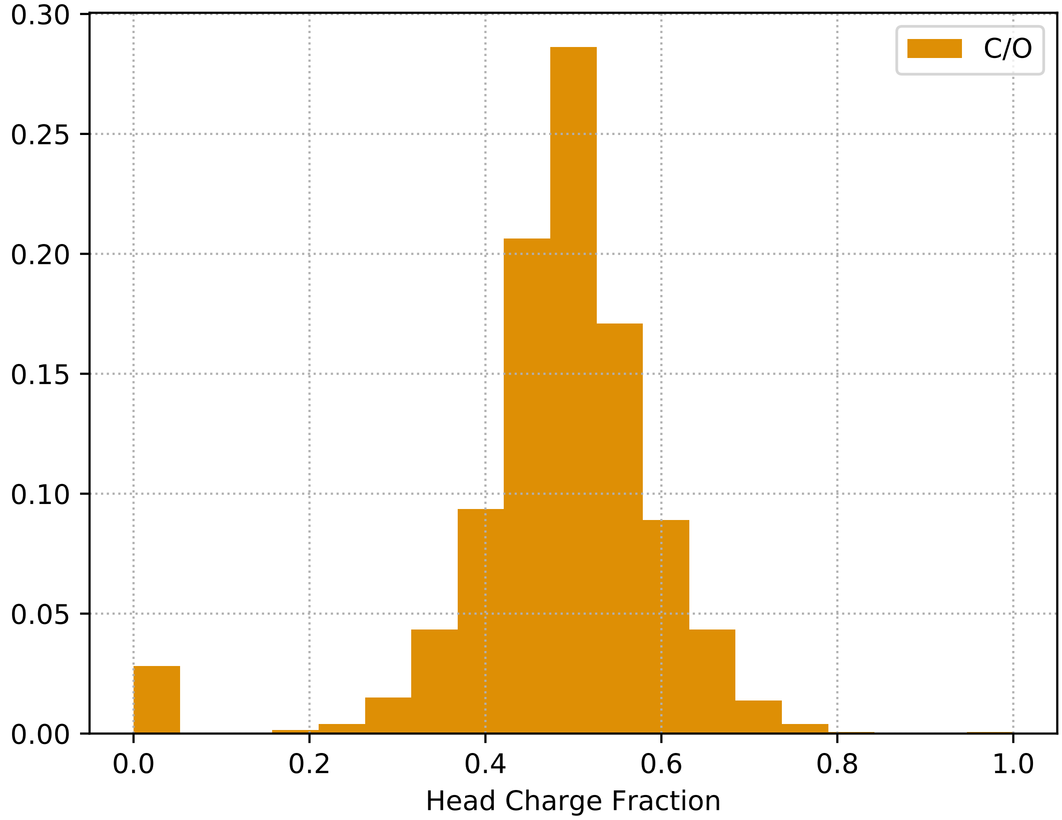

Figure 5.41: Fractional charge in the true head of carbon and oxygen events in TPC H.

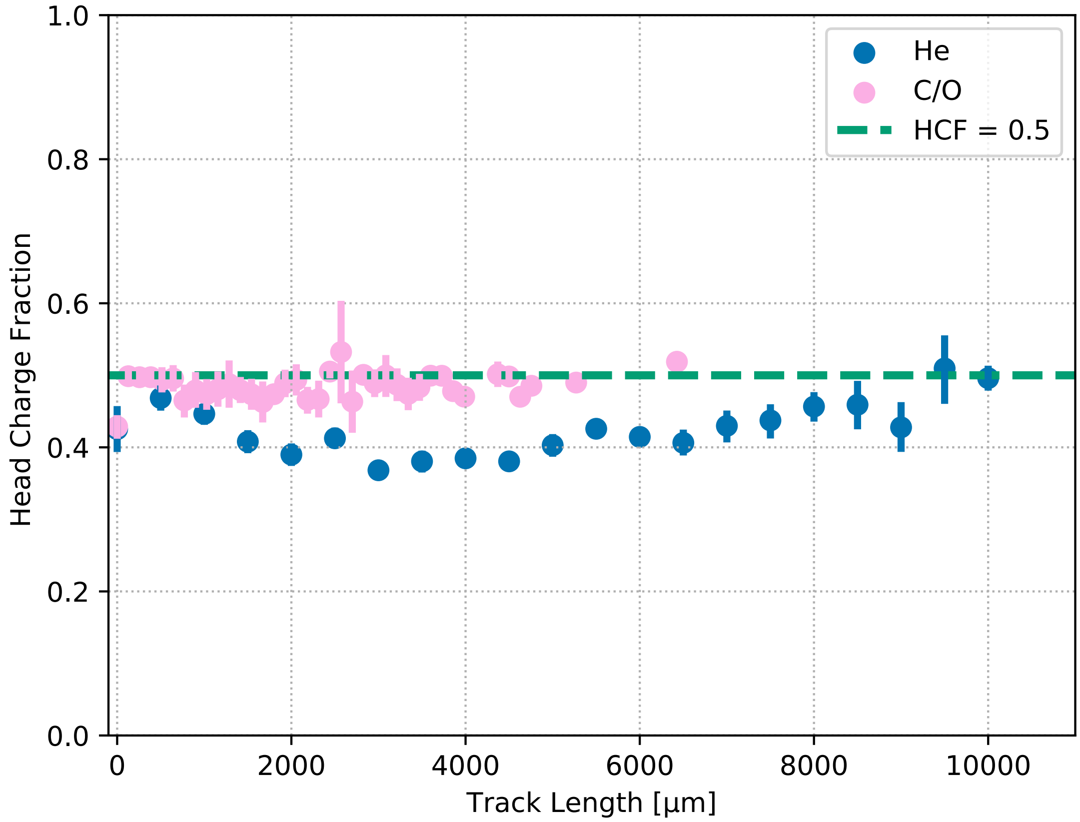

Figure 5.42: Head charge fraction in helium recoils (blue) and combining carbon and oxygen recoils (pink) versus track length in TPC H.

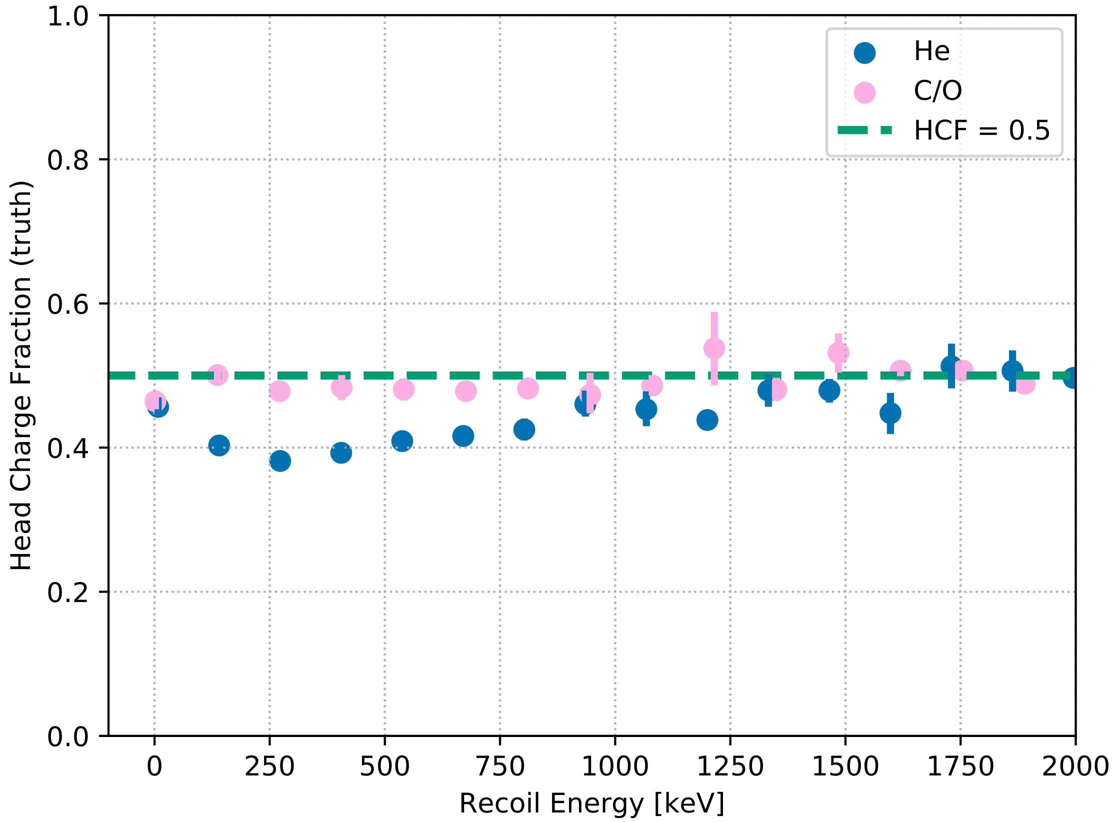

Figure 5.43: Head charge fraction in helium recoils (blue) and combining carbon and oxygen recoils (pink) versus detected recoil energy in TPC H.

CHAPTER 6
ANALYSIS OF FAST NEUTRON BACKGROUNDS AT SUPERKEKB

6.1 Introduction

The SuperKEKB accelerator is an asymmetric-energy electron-positron collider that is currently in operation at the High Energy Accelerator Research Organization (KEK) in Tsukuba, Japan. Its goal is to use a novel "nano-beam scheme," proposed by P. Raimondi, to deliver a luminosity of 8×10^{35} cm^{-2} s^{-1} at the $\Upsilon(4S)$ resonance of 10.48 GeV [26] for the Belle II experiment. This scheme squeezes the vertical size of the beam to 50 nm at the interaction point with beam currents of 2.62 A for the 7.0 GeV electrons in the high-energy ring (HER) and 3.60 A for the GeV positrons in the low-energy ring (LER). This will place the luminosity of SuperKEKB to be approximately 50 times larger than the previous generation accelerator, KEKB [26]. The projected luminosity of SuperKEKB compared to other high-energy colliders is shown in Figure 6.1 [27].

The increased beam currents and luminosity in addition to the decreased beam size present in SuperKEKB will result in a substantial increase in the rate of particles of the beam undergoing interactions before colliding at the desired interaction point (IP). Some of these interactions cause a sufficiently large change of momentum of beam particles such that their momenta are no longer within an "accepted" range. This acceptable range is fittingly referred to the *beam acceptance*. When beam particle momentum is outside the beam acceptance, the particle will eventually be "lost" from the beam orbit, interact with the beam-pipe wall, and create secondary showers that scatter forward down the beam-line. These lost particles are thusly referred to as *beam losses*. Beam loss is expressed relative to the change in beam current current, I, and is described by:

$$I = I_0 \exp\left(-\frac{t}{\tau}\right) \tag{6.1}$$

where τ represents the *beam lifetime*, with units of time, and I_0 represents the initial beam current.

When the showers created from beam losses enter the volume inside of Belle II—known as the *interaction region* (IR)—they can cause fake-rates, detector dead-time, and electronics

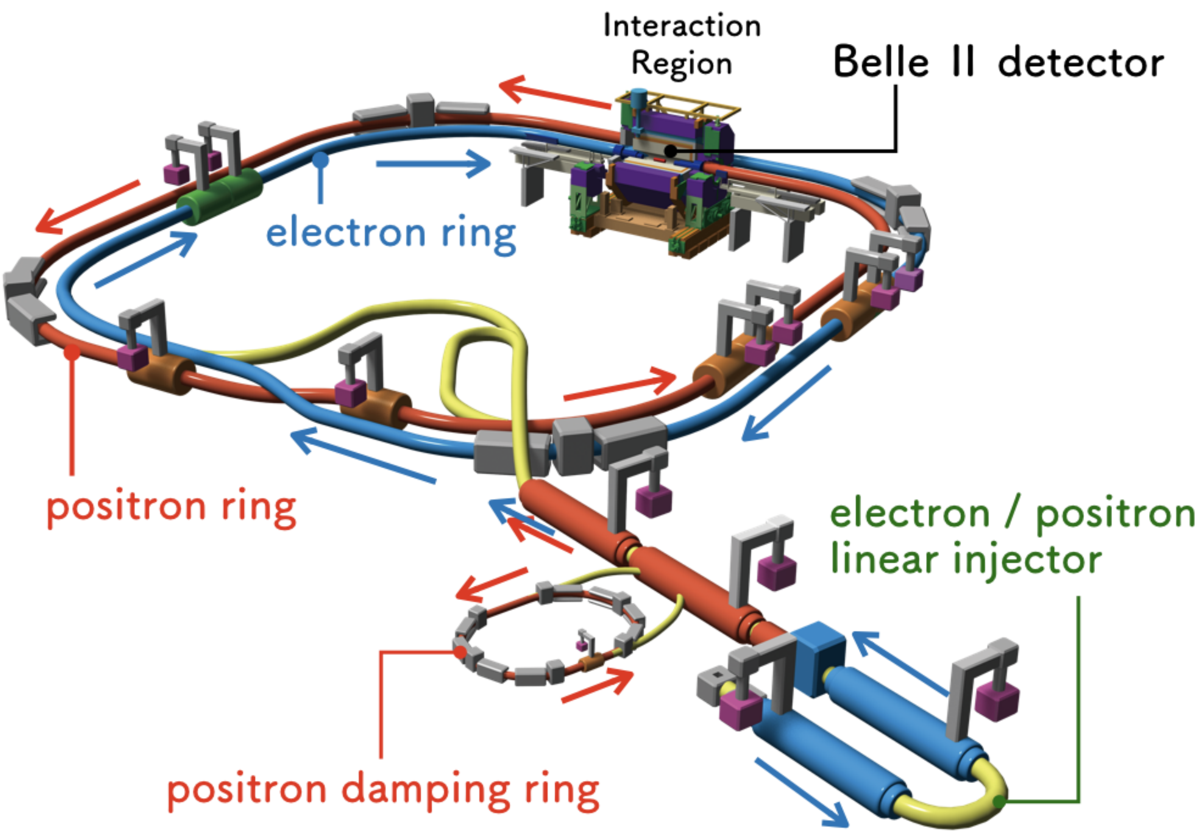

Figure 6.1: Schematic drawing of the SuperKEKB/Belle II facility [27].

	LER	HER
Energy [GeV]	4.0	7.0
Current [A]	3.6	2.62
Vertical beam size [nm]	59	59
Horizontal beam size [nm]	10200	7750
Bunch length [nm]	6×10^6	5×10^6
Number of bunches	2503	2503
Beam-pipe pressure [nTorr]	10	10

Table 6.1: SuperKEKB design parameters [28].

damage to the Belle II detector systems. These effects are more commonly referred to as "beam backgrounds." The success of the operation and performance of the SuperKEKB accelerator and the Belle II detector depend on accurate modeling and effective mitigation of such backgrounds.

In general, beam losses can be classified into two types—inter-beam losses, interactions which involve particles from different beams; and single-beam losses, interactions which involve particles within the same beam. The magnitudes of the losses are typically expressed in terms of the beam lifetime. The total lifetime of the beam is combination of all respective lifetimes for each beam-loss mechanism and is expressed by:

$$\frac{1}{\tau} = \sum \frac{1}{\tau_i} \tag{6.2}$$

where i represents the beam-loss mechanism. The beam lifetime relates to the rate of current loss by:

$$-\frac{1}{I}\frac{dI}{dt} = \frac{1}{\tau} \tag{6.3}$$

where I is the beam current.

In order to isolate the effects of all beam loss processes and understand all of the different components of the total beam lifetime, the commissioning of SuperKEKB was broken into two phases—Phase 1 and Phase 2. The scope of this dissertation is limited to Phase 1 of SuperKEKB commissioning, which was dedicated to the study of single beam losses without any luminosity and without the Belle II detector present in the IR. The beam parameters for the design conditions for SuperKEKB and during Phase 1 operations are shown in Table 6.1.

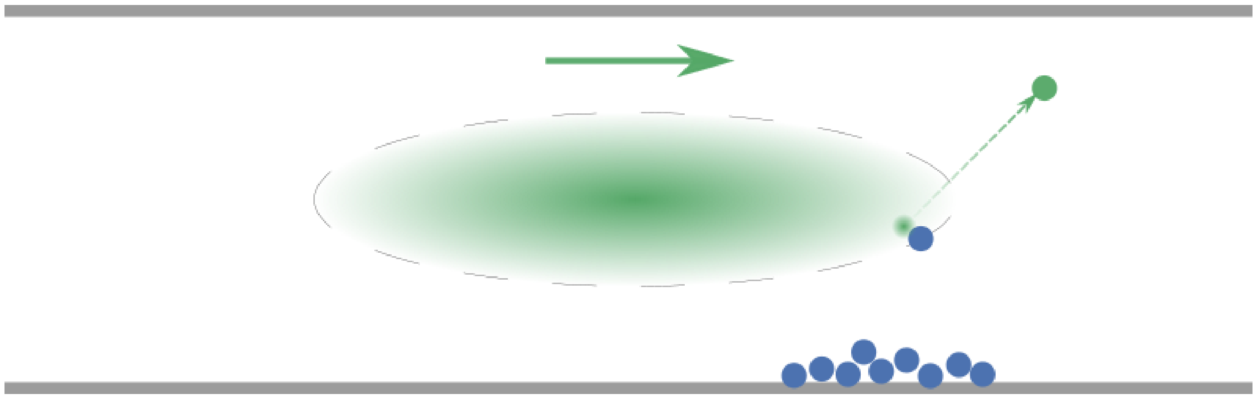

Figure 6.2: Graphic demonstrating a simplified model of beam loss due to beam-gas scattering. A single beam particle (green), originally contained within the beam orbit—represented by the ellipse—scatters with a residual gas atom (blue) after the atom desorbs from the inner beam-pipe surface. After the scattering, the beam particle is lost from the beam orbit and will eventually produce showers that leave the beam-pipe.

6.2 Single-beam loss processes

There are three primary mechanisms of beam-losses that can occur within a single beam—beam-gas scattering, Touschek scattering, and synchrotron radiation—which will be detailed in the sections below.

6.2.1 Beam-gas losses

Beam-gas losses occur when the beam interacts with a residual gas atom inside of the beam-pipe via Coulomb scattering. This process is illustrated in Figure 6.2.1. Beam-gas interactions scale with the pressure inside of the beam-pipe and the square of the charge of the residual gas nuclei. In ideal conditions, such as those assumed during the design conditions of SuperKEKB, beam-losses due to beam-gas interactions should be negligible since the vacuum levels are expected to be optimal—approximately 10 nTorr. However, during Phase 1 of commissioning, beam-gas scattering is of significant concern due to the fact that the vacuum levels inside of the beam-pipe are expected to be orders of magnitude larger than those assumed in the design conditions.

Interactions of beam particles with residual gas atoms can happen via elastic or inelastic collisions. The cross section for elastic interactions is given by [29]:

$$\sigma_{\text{elastic}} = \frac{2\pi r_e Z^2}{\gamma^2}\frac{\beta_1\beta_2}{d^2} \tag{6.4}$$

where r_e is the classical electron radius, Z is the target nucleus atomic number, γ is the relativistic Lorentz factor, β_1 and β_2 are the betatron functions, and d is the beam size aperture. Inelastic scattering interactions are a form of bremsstrahlung radiation in that the beam particle emits a bremsstrahlung photon when its trajectory is altered. The cross section for this process is given by [29]:

$$\sigma = \frac{16 r_e^2 Z^2}{411}\ln\left[\frac{183}{Z^{1/3}}\right]\ln\left[\frac{E}{\epsilon_{RF}} - \frac{5}{8}\right] \tag{6.5}$$

where ϵ_{RF} is the energy acceptance of the beam, and E is the beam energy.

The component of the total beam current due to beam-gas interactions, τ_{BG}, is given by:

$$\frac{1}{\tau_{BG}} = c\sum \sigma_i n_i \tag{6.6}$$

where σ_i and n_i represent the beam-gas cross section and atomic density of each atomic element present in the residual gas, respectively and c represents the speed of light—the approximate speed of the highly relativistic beam particles in the accelerator. If the atomic composition of the residual gas is constant over time, i.e. Z in Equations 6.4 and 6.5 is constant, the summation in Equation 6.6 reduces to one term. The beam lifetime is then directly related to the density of charged particles in the beam, their velocity, and the density of residual gas atoms. Quantitatively, this means the beam-loss scales with beam current and the pressure in the beam-pipe. Expressing this in terms of the beam-loss rate given by Equation 6.3 results in:

$$\frac{dI}{dt} \propto -IP \tag{6.7}$$

where P is the pressure in the beam-pipe.

If Z is not constant, then the Z^2 terms in the cross-sections given by Equations 6.4 and 6.5 change. Taking this into account results in a relationship of:

$$\frac{dI}{dt} \propto -IPZ^2 \tag{6.8}$$

in the limit of $Z^2/\ln\frac{1}{Z^{1/3}} \approx Z^2$, in which the $\ln\left[\frac{183}{Z^{1/3}}\right]$ term can be safely ignored.

6.2.2 Touschek losses

Touschek losses occur when particles within the beam interact with each other via electrostatic repulsion. Specifically, Touschek losses are beam losses from the transformation of small transverse momentum into large longitudinal momentum due to Coulomb scattering [26]. This process is illustrated in Figure 6.2.2.

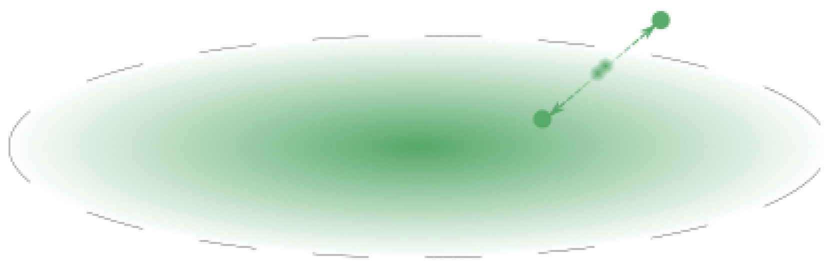

Figure 6.3: Graphic demonstrating a simplified model of beam loss due to Touschek scattering. Two particles within the same beam bunch scatter off of each other, causing one to leave the beam orbit and eventually producing showers that leave the beam-pipe volume.

The Touschek loss rate of the beam is given by [26]:

$$\frac{dN}{dt} = -\frac{N}{\tau} \tag{6.9}$$

where τ is the Touschek lifetime of the beam and N is the number of particles in a beam bunch. A beam bunch is the substructure of the larger beam in which packets of particles are contained. The number of bunches in the LER and HER are shown in Table 6.1. The Touschek loss rate can also be described by integrating local loss rates [26]:

$$-\frac{N}{\tau} = -R \tag{6.10}$$

and

$$R = \frac{1}{L_{\mathrm{circ}}} \oint r\, ds \tag{6.11}$$

where L_{circ} is the circumference of the ring and r is the local loss rate. The formal description of local loss rate can be obtained by Bruck's formula. For scaling purposes, r scales, in general, with the square of the amount of charge in the bunch and volume of the beam bunch [26]. Specifically:

$$\frac{dI}{dt} \propto \frac{N^2}{\sigma_x \sigma_y \sigma_z}$$

where σ_x, σ_y, and σ_z are the transverse (x and y) and longitudinal (z) dimensions of the bunch volume. As can be seen in Table 6.1, σ_y is many orders of magnitude smaller than the other dimensions. As such, σ_x and σ_z can be approximated as constants with respect to σ_y. This allows for the following scaling relationship for Touschek beam losses and, subsequently, the Touschek lifetime:

$$-\frac{N}{\tau_T} = \frac{dN}{dt} \propto \frac{N^2}{\sigma_y} \tag{6.12}$$

For practical experimental reasons, it is usually not feasible to measure the number of particles within a single bunch. However, as shown in Table 6.1, the number of bunches in each beam is a constant value for both beams. Additionally, measurements of the beam current during operation are readily available. Therefore, it is convenient to utilize the relationship between N and I:

$$N \propto \frac{I}{N_b}$$

ca where I is the beam current and N_b is the number of bunches. Utilizing this in Equation 6.12 results in the following expression for rate of beam loss from Touschek losses for SuperKEKB:

$$\frac{dI}{dt} \propto -\frac{I^2}{N_b \sigma_y} \tag{6.13}$$

indicating that the Touschek losses of significant concern for the LER beam due to its higher beam current.

6.2.3 Synchrotron radiation

Synchrotron radiation (SR) losses occur when accelerated charged particles radiate photons. This process is illustrated in Figure 6.2.3 [30]. The amount of power radiated by a given charged particle via SR is proportional to the beam energy squared and the magnetic field strength squared. As such, the main source of synchrotron radiation is the HER beam. The expected photon energies due to SR are $\mathcal{O}(10)$ keV—significantly lower than the other types of beam losses. While low in energy, a large rate of synchrotron can be especially damaging. However, for Phase 1 of SuperKEKB operations, there were no magnets close enough to the IR to produce significant SR, leading to the conclusion that synchrotron radiation, while important for SuperKEKB and Belle II operations, is not of concern during Phase 1 [25].

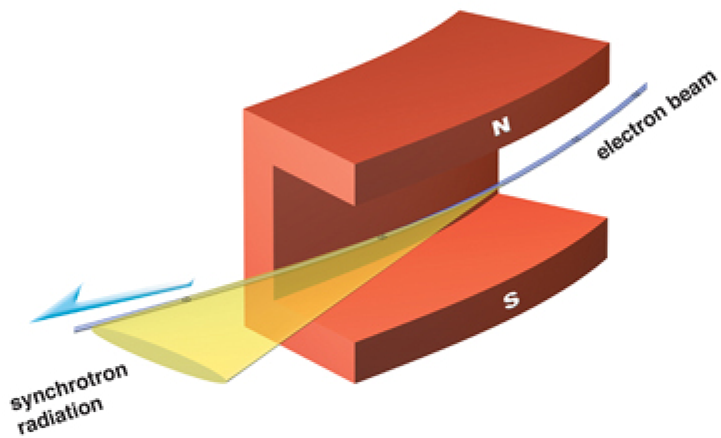

Figure 6.4: Illustration of a synchrotron radiation created from an electron beam traversing through a bending dipole magnet.

6.3 Neutron production from beam backgrounds

Beam-loss processes in an electron-positron collider such as SuperKEKB predominantly produce showers of electromagnetic particles as the electrons and positrons from the beams interact with the beam-pipe. However, neutrons, while less common, can also be produced via nuclear effects. Neutrons can be produced in large numbers by high-energy electrons and/or positrons traverse materials—such as a beam particle traversing through the beam-pipe. This can cause excitations of nucleons, which can then result in emission of neutrons. The primary mechanism for this process is known as *Giant Resonances*, which include the *Giant Dipole Resonance* (GDR) [31] and *Giant Quadrupole Resonance* (GQR) [32].

In general, the Giant Resonances describe a collective motion of nuclear protons against their neutron counterparts within an atomic nucleus due to interactions with photons of specific frequencies. Specifically, in electron and positron beams, the GDR is well-known to produce neutrons in materials from aluminum to lead ($12 < Z < 82$)—a range comprising most of the materials typically used in accelerator design and construction. This type of neutron production occurs by photonuclear reactions via bremsstrahlung photons and by electroproduction via virtual photons. GDR neutrons are produced by photons with energies within the range of $7 < E_\gamma < 40$ MeV. A detailed discussion of the subject, including an analytical formulation of rate of neutron production per incident electron can be found in [33]. The energy spectra for neutrons produced by GDR interactions is typically within the $\mathcal{O}(1)$ MeV and above range, and is described in detail in [34].

Table 6.2: BEAST II Phase 1 detector system names, detector types, and unique measurement or capability provided of each system.

System name	Detector Type	Unique measurement or capability
PIN	PIN diodes	Instantaneous dose rate at many positions
Diamond	Diamond Sensors	Near-IP fast dose rate, beam abort prototype
Crystal	CsI(Tl), CsI, LYSO crystals	Electromagnetic energy spectrum, injection backgrounds
BGO	BGO crystals	Electromagnetic dose rate
CLAWS	Plastic scintillators	Injection backgrounds
^{3}He	^{3}He tubes	Thermal neutron rate
TPC	Time Projection Chambers	Fast neutron flux and directionality
QCSS	Plastic scintillators	Charged particle rates

6.3.1 Analysis of fast neutrons at SuperKEKB

From February to July, 2016, the BEAST II collaboration performed a series of measurements of the SuperKEKB beam backgrounds using a system of detectors and sensors for the purposes of commissioning the SuperKEKB accelerator [25]. A listing of the detectors used in Phase 1 is shown in Table 6.2 and CAD drawing and photograph of the Phase 1 BEAST II apparatus is shown in Figure 6.5. Among those detectors were two of TPCs described in Chatper 5 with the goal of providing measurements of fast neutrons produced by the present beam background processes in order to test the validity of current beam background simulations.

The TPC subsystem was designed to measure the compare the following quantities for Monte Carlo and experimental data:

- Nuclear recoil energy spectrum.
- Neutron production from Touschek beam losses and beam-gas, separately.
- Angular distributions of nuclear recoils.

Additionally, we aim to distinguish incoming neutrons from outgoing neutrons using head-tail measurements, as described in Chapter 5.

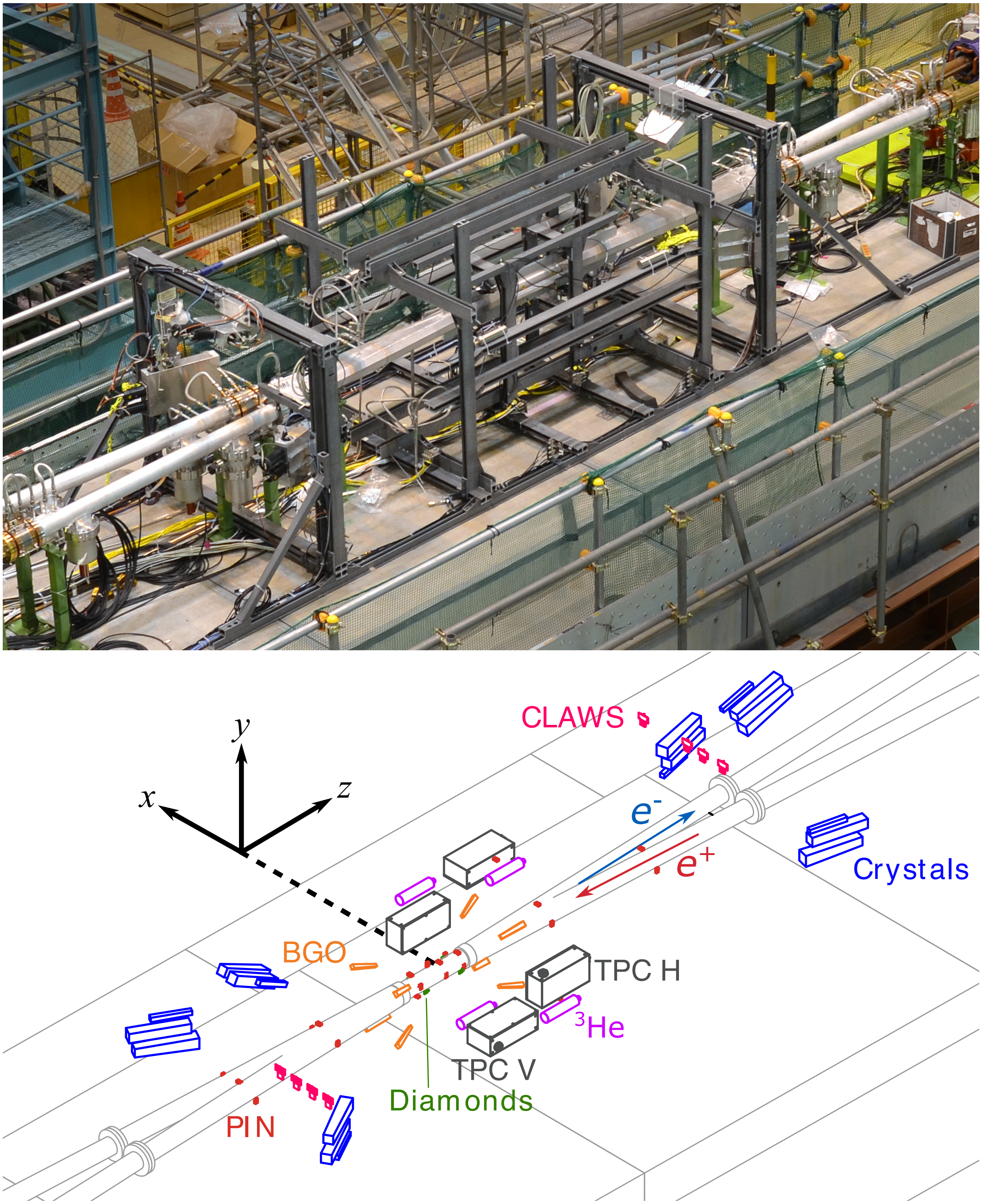

Figure 6.5: A photograph (top) of, with a CAD rendering (bottom) from the same perspective of the BEAST II Phase 1 detector system [25].

6.3.2 Simulation of BEAST II Phase 1 TPCs

The details of the procedure of the production of the BEAST II Phase 1 Monte Carlo pipeline are described in detail in Reference [25]. However, the general production pipeline, as described in [25], is as follows*:

1. Generation of primary particles from beam-induced backgrounds.

2. Modeling of the setup and the interaction and transport of primary and secondary particles.

3. Simulation of the detector response and digitization.

4. Scaling of the detector response with accelerator conditions present during experimental runs.

The Strategic Accelerator Design (SAD) software framework [35] performed step 1) and Geant4 [36] performed steps 2) – 4). In step 1), the SAD simulation is performed such that the beam loss rates correspond to 1 s of simulated beam time for the SuperKEKB accelerator. The primary particles are then passed through the remaining steps in the simulation framework. The simulated TPC data contains digitized events that replicate the data format produced by the FE-I4b chip output, which is processed through the event reconstruction procedure described in Chapter 5. In turn, this translates to a simulated rate of nuclear recoil events that pass event selections at given set of beam parameters. However, due to the low interaction probability of neutrons in the TPCs, it is necessary to provide longer simulation times to provide a sufficiently large simulated data sample. This is done by simulating each neutron that passes the simulated TPC volume 18000 times—resulting in 5 hours-equivalent beam simulation, corresponding to 13011 simulated events for fast neutron analysis.

6.4 Simulation reweighting procedure

In order to compare the observations in experimental data to the predictions from simulation, the event rate in the simulated data must be *reweighted* from the beam conditions in Table 6.3 to the measured conditions during the experimental data runs. This is done by normalizing the rate in each TPC to one second by dividing by a factor of 18000 (5 hrs) from the total

*This list closely follows the list presented in the simulation section of Reference [25]

Table 6.3: Machine parameters used for the BEAST II Phase 1 Monte Carlo simulation data [25].

Machine parameters	HER	LER
Beam current I [A]	1.0	1.0
Number of bunches N_b	1000	1000
Bunch current I_b [mA]	1.0	1.0
Vertical beam size σ_y [µm]	59	110
Emittance ratio $\varepsilon_y/\varepsilon_x$	0.1	0.1
Pressure P [nTorr]	10	10

number of events. The Touschek and beam-gas backgrounds are then scaled independently. The Touschek background is scaled by ratio of the experimentally measured value of I^2/σ_y to the value obtained in Table 6.3. The beam-gas background is scaled by the ratio of experimentally measured value of IPZ_e^2 to the value obtained in Table 6.3.

6.5 Event selections

All selections and their cumulative efficiencies on beam-background simulations and experimental data that will be used to obtain event samples for all analyses in this chapter are shown in Tables 6.4 and 6.5. The selections come from the studies done in Chapter 5. Each analysis in this chapter will use at least the first three selections, which are necessary for recoil selection and background rejection. The upcoming recoil energy spectra and the event rates of Touschek from beam-gas backgrounds use only these first three selections, as the remaining selections are only required to isolate helium recoils, as was shown in Section 5.5, and we wish to include all nuclear recoils for these analyses. The directional analyses at the end of this chapter utilize all selections in Tables 6.4 and 6.5. The motivations for the selections on the angle ϕ will be detailed in the later sections of this chapter in the discussion of the analyses. The HCF variable is the *head-charge fraction* variable from Section 5.5. A more detailed discussion of this selection and its application the directional analyses of helium recoils will be presented in Section 6.9.

Table 6.4: Full event selections to be used for selecting signal events, along with each selection's cumulative efficiency in MC Touschek, MC beam-gas, and experimental data in TPC H.

	MC Touschek	MC Beam-gas	Exp
Edge veto	0.46	0.48	0.0444
$dE/dx > 0.04$ keV/µm	0.31	0.32	0.0426
$E > 50$ keV	0.23	0.25	0.0419
$dE/dx < 0.162$ keV/µm	0.12	0.13	0.0027
$abs(\phi) > 160°$	0.03	0.12	0.0007
HCF < 0.5	0.02	0.02	0.0005

Table 6.5: Full event selections to be used for selecting signal events, along with each selection's cumulative efficiency in MC Touschek, MC beam-gas, and experimental data in TPC V.

	MC Touschek	MC Beam-gas	Exp
Edge veto	0.48	0.46	0.1333
$dE/dx > 0.04$ eV/µm	0.30	0.31	0.1265
$E > 50$ keV	0.24	0.25	0.0052
$dE/dx < 0.162$ ev/µm	0.12	0.12	0.0030
$70° > \phi > -110°$	0.03	0.03	0.0008
HCF < 0.5	0.02	0.02	0.0005

Table 6.6: Number of total events detected compared to the Monte Carlo prediction for the HER run.

	TPC H	TPC V
MC Beam-gas	3 ± 0	4 ± 0
MC Touschek	3 ± 1	4 ± 1
Experiment	48 ± 7	35 ± 6

Table 6.7: Number of total events detected compared to the Monte Carlo prediction for the LER run.

	TPC H	TPC V
MC Beam-gas	340 ± 7	272 ± 6
MC Touschek	536 ± 16	412 ± 10
Experiment	567 ± 22	640 ± 80

6.6 Experimental runs for fast neutron analysis

For the fast neutron measurements in experimental data,, we performed dedicated, longer duration runs specifically to accumulate a sufficient sample of nuclear recoils in the TPCs. A run for the HER occurred on May 23, 2016 for approximately 1.5 hours at an average beam size of approximately 40 μm with initial beam current of 500 mA. Table 6.6 shows the number of detected events that pass the first three selections in Tables 6.4 and 6.5 compared to the reweighted number of Monte Carlo events passing the same selections for this run. While the total number of detected events in this HER sample is small enough that statistical uncertainties are larger than desired, we find that the Monte Carlo underestimates the observed number of events recorded by the TPCs by approximately a factor of five in both TPCs, with a very large uncertainty due to limited statistics.

Due to the fact that the Touschek contribution to beam backgrounds is predicted to be far more problematic in the LER than in the HER and given the very low detection rate of the TPCs, it was decided to devote substantially more experiment time to collecting data from the LER than for the HER for fast neutron analysis. The resulting larger statistics allow us to perform more detailed investigations for the neutron background from the LER, including studies of directional distributions and separating the beam-gas and Touschek contributions to the background in experimental data. Dedicated LER runs occurred on May 29, 2016 for approximately 5.5 hours at a beam current of approximately 600 mA, topping off the beam as required. Using the emittance control knob, the beam size was set at three specific values where each run corresponded to one set beam size. The beam size was measured using the X-ray monitors [25], and was measured to be approximately 40 µm, 60 µm, and 90 µm for the three runs, respectively. Each run is further divided into sub-runs. A sub-run is defined as a period of time of stable beam conditions at the desired settings as defined above, specifically excluding injection times. Table 6.7 shows the number of detected events compared to the reweighted Monte Carlo prediction for this run. We find that for the LER the agreement between simulation and experimental data is better. On average, the observed number of events is within a factor of two lower than predicted.

6.7 Nuclear recoil energy spectra

Figures 6.6 and 6.7 show the recoil energy distributions for all neutron candidates collected in experimental data and the reweighted Monte Carlo simulation for the LER run. The recoil energy distributions are fit with a decaying exponential of the form Ae^{-bE}, where E is the recoil energy in keV. The fit results are shown in Table 6.8. From these parameters, we note that the spectral shapes of the simulated backgrounds in each TPC—parameter b in the fit—are consistent within errors. However, the same parameter in experimental data for both TPCs is significantly larger than in the simulated data.

Table 6.8: Results of fitting the recoil energy spectra for TPCs 3 and 4 for Monte Carlo and experimental data for the LER runs.

	A	b	χ^2/ndf
TPC H MC beam-gas	328.9 ± 28.7	0.0027 ± 0.0002	0.41
TPC H MC Touschek	497.6 ± 34.5	0.0026 ± 0.0001	0.50
TPC H MC Total	824.8 ± 44.0	0.0027 ± 0.0001	0.52
TPC H Exp. data	629.0 ± 42.4	0.0031 ± 0.0002	1.27
TPC V MC beam-gas	179.1 ± 17.2	0.0026 ± 0.0002	0.37
TPC V MC Touschek	295.8 ± 22.5	0.0028 ± 0.0002	0.97
TPC V MC Total	473.0 ± 28.3	0.0027 ± 0.0001	0.50
TPC V Exp. data	537.2 ± 34.3	0.0033 ± 0.0002	0.88

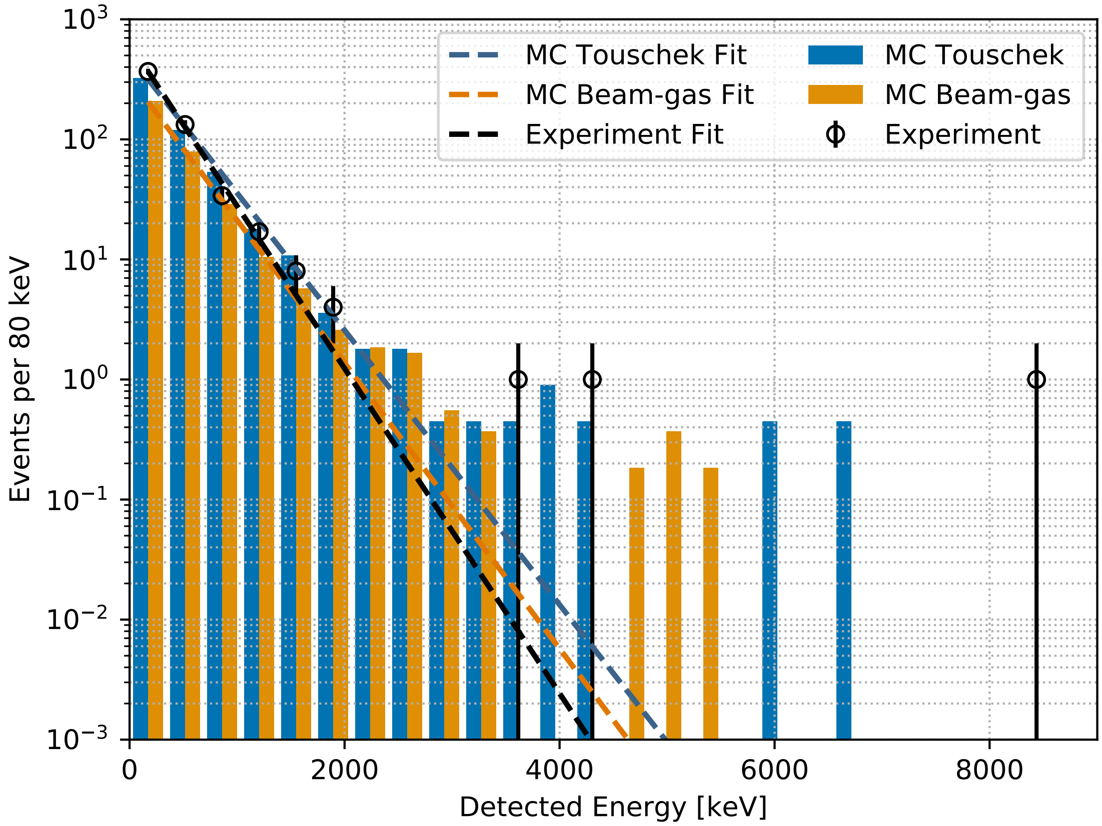

Figure 6.6: Detected energy distribution for nuclear recoil candidates in TPC H for the LER run. The blue and orange bar histograms show the expectations for Touschek and beam-gas (Coulomb and bremsstrahlung) contributions obtained via the reweighted simulation, respectively, and the black points show the measured values in experimental data. The distributions are fit to a decaying exponential. The dashed lines show the returned fit functions for the Monte Carlo and experimental data. The parameters of the fit are shown in Table 6.8.

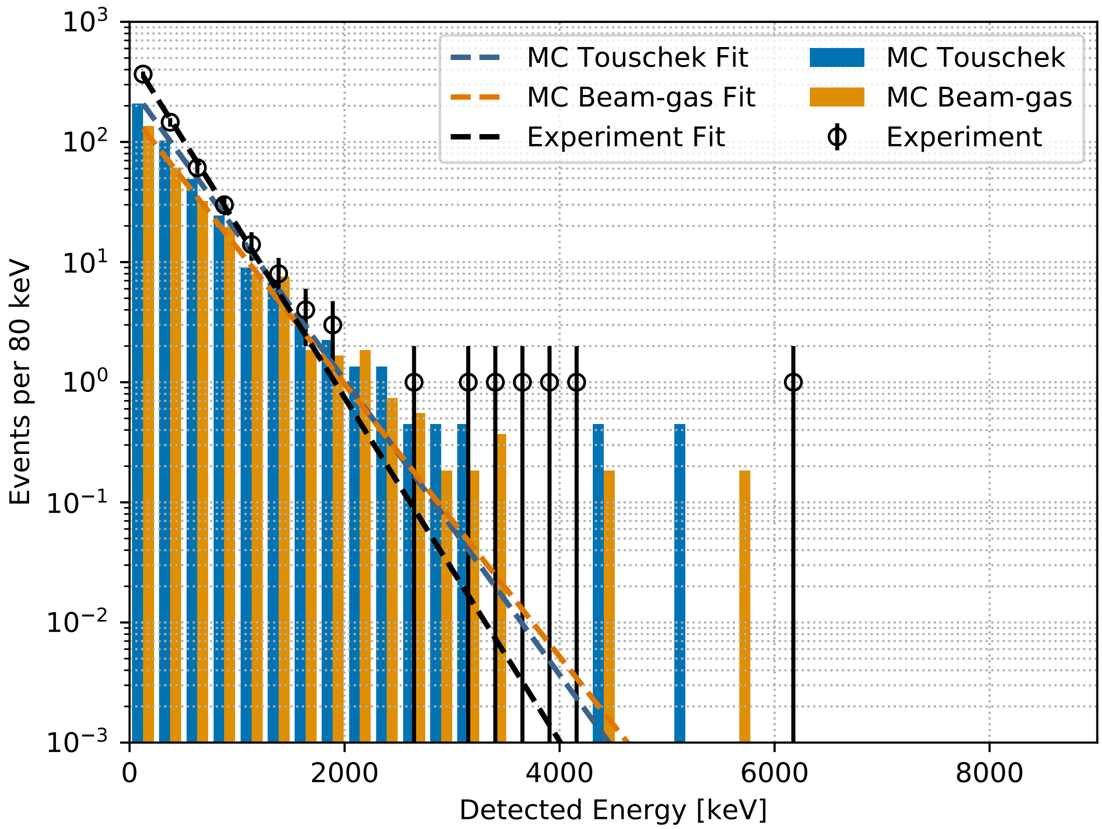

Figure 6.7: Detected energy distribution for nuclear recoil candidates in TPC V for the LER run. The blue and orange bar histograms show the expectations for Touschek and beam-gas (Coulomb and bremsstrahlung) contributions obtained via the reweighted simulation, respectively, and the black points show the measured values in experimental data. The distributions are fit to a decaying exponential. The dashed lines show the returned fit functions for the Monte Carlo and experimental data. The parameters of the fit are shown in Table 6.8.

Table 6.9: Table of values of corrected dQ/dx in TPC H, TPC V, and Monte Carlo simulation and resulting conversion factors. A mean value of dQ/dx, obtained from averaging the dQ/dx of each of the two ^{210}Po calibration sources in Monte Carlo, TPC H, and TPC V, shown in Figure 5.17, is calculated separately and shown in the second column of the table. The third column shows the ratio of the obtained mean in each TPC to the mean calculated from the Monte Carlo simulation. This ratio is then used as a multiplicative correction to the detected recoil energies presented in Chapter 6.

	Average dQ/dx [e/µm]	Correction Factor
Simulation	3227	1.00
TPC H	2172	1.49
TPC V	1657	1.95

The same analysis can be done for the HER run. In order to perform this analysis, we must first calibrate the energy scale following the procedure outlined in Section 5.3.2 for the HER run period†. In short, the calibrated dQ/dx curves are shown in Figure 6.8 and the correction factors are shown in Table 6.9. As can be seen, the gain is significantly lower in both TPCs during this run. This is due to the fact that the volumetric flow rate of the gas was set to the maximum value for the LER run and approximately a factor of 5 lower in the HER run. Finally, the energy recoil spectra for the HER run are shown in Figures 6.9 and 6.10, and the fit results are shown in Table 6.10. Here we find that the parameter b is consistent within errors in the simulated data, but the value in simulated data differs significantly from the value in experimental data.

Because the spectral shapes—parameter b of the fits—of simulated background components shown here do not differ strongly from each other, the spectral shape cannot be used to separate the different background components. Instead, we attempt to achieve this separation by two other methods: by utilizing the background rate dependence on accelerator beam size, and by utilizing the recoil angle distribution.

†For the sake of clarity, it should be stated that the calibration procedure outlined Section 5.3.2 was done precisely for the LER run described in this chapter.

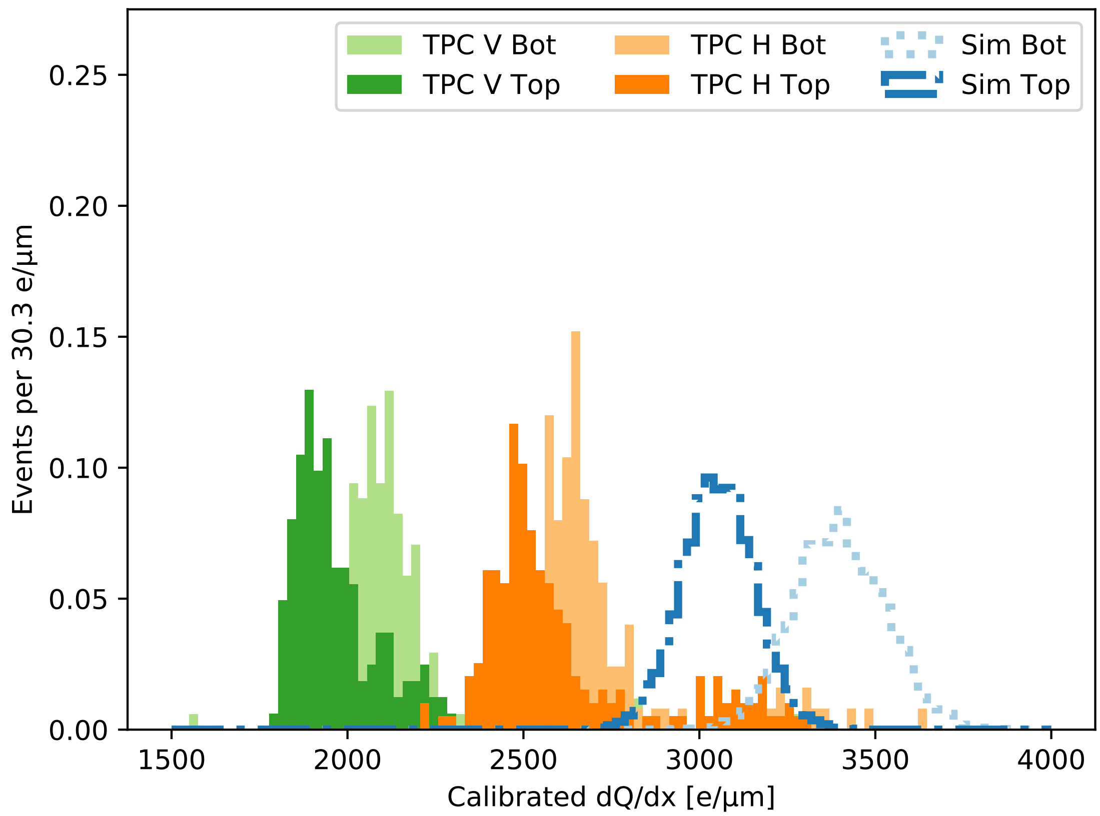

Figure 6.8: Histograms of the reconstructed detected charge divided by track length during the time of the HER run, after correcting for pixel saturation and charge below the pixel threshold, shown in Figures 5.13 and 5.16, respectively, for events from internal ^{210}Po calibration alpha sources in experimental and Monte Carlo data. The vertical axis shows the total number of events from both sources, normalized to 1, for TPC H, TPC V, and Monte Carlo separately. The mean value of each peak is then used as an input in calculating the correction factor.

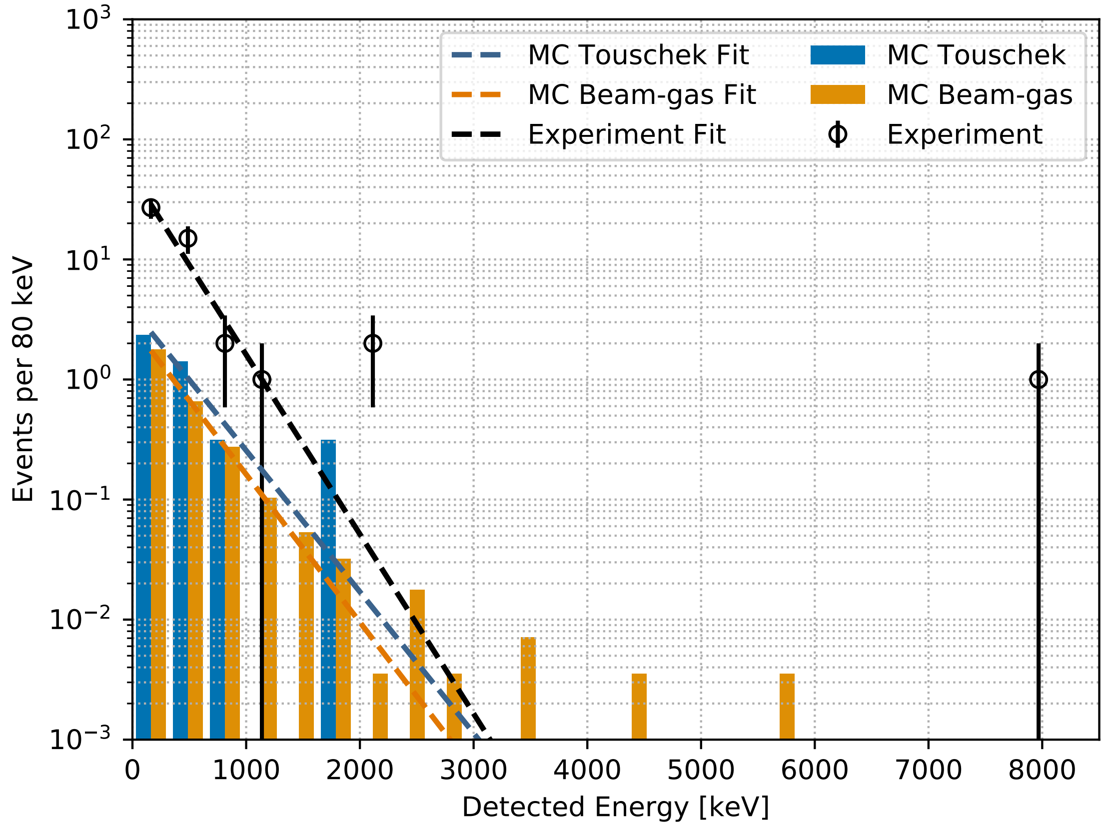

Figure 6.9: Detected energy distribution for nuclear recoil candidates in TPC H for the HER run. The blue and orange bar histograms show the expectations for Touschek and beam-gas (Coulomb and bremsstrahlung) contributions obtained via the reweighted simulation, respectively, and the black points show the measured values in experimental data. The distributions are fit to a decaying exponential. The dashed lines show the returned fit functions for the Monte Carlo and experimental data. The parameters of the fit are shown in Table 6.10.

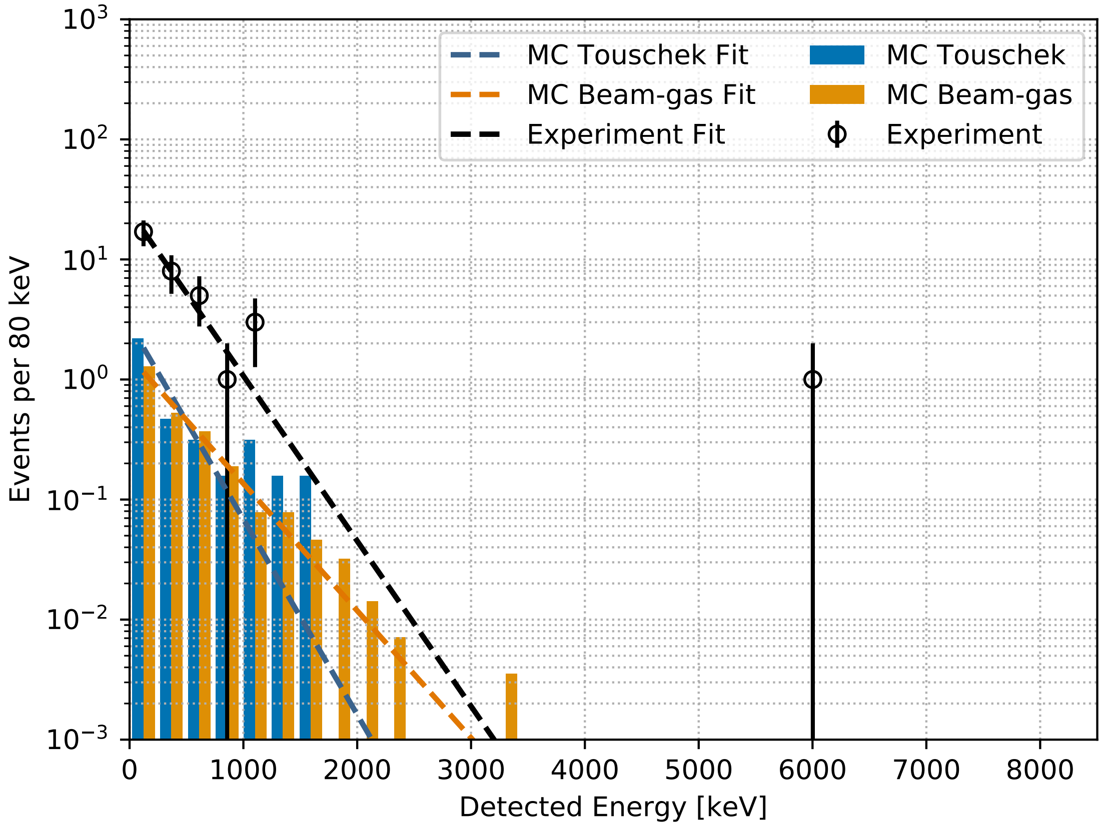

Figure 6.10: Detected energy distribution for nuclear recoil candidates in TPC V for the HER run. The blue and orange bar histograms show the expectations for Touschek and beam-gas (Coulomb and bremsstrahlung) contributions obtained via the reweighted simulation, respectively, and the black points show the measured values in experimental data. The distributions are fit to a decaying exponential. The dashed lines show the returned fit functions for the Monte Carlo and experimental data. The parameters of the fit are shown in Table 6.10.

Table 6.10: Results of fitting the recoil energy spectra for TPCs H and V for Monte Carlo and experimental data for the HER run.

	A	b	χ^2/ndf
TPC H MC beam-gas	2.8 ± 2.5	0.0028 ± 0.0019	0.01
TPC H MC Touschek	3.9 ± 3.2	0.0027 ± 0.0020	0.22
TPC H MC Total	7.01 ± 4.3	0.0028 ± 0.0015	0.04
TPC H Exp. data	50.2 ± 11.5	0.0034 ± 0.0006	1.46
TPC V MC beam-gas	1.6 ± 1.6	0.0024 ± 0.0019	0.01
TPC V MC Touschek	2.9 ± 3.3	0.0037 ± 0.0050	0.14
TPC V MC Total	3.61 ± 3.02	0.0024 ± 0.0018	0.07
TPC V Exp. data	25.5 ± 7.0	0.0031 ± 0.0007	0.91

6.8 Analysis of fast neutron rates versus beam size

By utilizing how beam-gas and Touschek rates are expected to change with beam parameters, as discussed in Sections 6.2.1 and 6.2.2, measuring how the nuclear recoil event rate changes with accelerator beam-size and comparing the measurement to the rate predicted from simulation provides a useful method for testing the validity of the beam background simulations. According to Sections 6.2.1 and 6.2.2, the rate due to beam-gas scattering should linearly increase with IPZ_e^2 and Touschek backgrounds should linearly increase with I^2/σ_y. Analytically, the rate of nuclear recoils in the TPCs can be described as‡:

$$R \propto S_{bg} IPZ_e^2 + S_T \frac{I^2}{\sigma_y}$$

where S_{bg} and S_T represent the TPC *sensitivities* to beam-gas and Touschek backgrounds, respectively. [25]. Dividing by IPZ_e^2 gives:

$$\frac{R}{IPZ_e^2} \propto S_{bg} + S_T \frac{I^2}{\sigma_y IPZ_e^2} \tag{6.14}$$

This provides a description of the change-in-rate of nuclear recoils, R, versus the inverse of the beam-size, $1/\sigma_y$. The beam-size during the experimental runs is configurable, as described previously, and occurs on a time scale of a few minutes. As such, the first term on the righthand side of Eq. 6.14 can be treated as constant, since the change in pressure levels at constant beam-current occurs on the time-scale of many hours. This allows for a simple, linear fit for the observed rate of nuclear recoils in the TPCs versus $1/\sigma_y$ to separate beam-gas and Touschek backgrounds, which can be applied to both experimental and Monte Carlo data for a direct comparison.

The measured nuclear recoil rates in the TPCs versus LER beam size for the experimental runs described in Section 6.6 are shown in Figure 6.13. The obtained sensitivities can be integrated to directly obtain the measured and predicted rates to give a yield, denoted as N_T for the yield of Touschek events and N_{bg} for beam-gas events. The observed yields are shown in Table 6.11. The most striking disagreement is between the predictions from the reweighted Monte Carlo and the experimental data in the horizontal plane of the beam-pipe, or in TPC H, in the beam-gas component, where the Monte Carlo is approximately three times larger than the measured amount in experimental data. The Touschek background is

‡This description follows the heuristic model presented in Ref. [25]. We note that Ref. [25] also presents our measurements of this same TPC subsystem. However, here we present new results using updated selections and energy measurement corrections presented in this dissertation.

Table 6.11: Calculated yield from the measured rates of nuclear recoils from beam-gas and Touschek backgrounds shown in Figure 6.13 for both experimental data and Monte Carlo in each TPC.

	N_{bg}	N_T
TPC H MC	340 ± 19	580 ± 22
TPC H Exp.	129 ± 22	496 ± 24
TPC V MC	261 ± 17	445 ± 19
TPC V Exp.	257 ± 24	424 ± 27

also overestimated in the simulation by approximately 25% In TPC V, the predicted and observed rate of beam-gas and Touschek events are equal within errors, with the central values differing at the order of 10%.

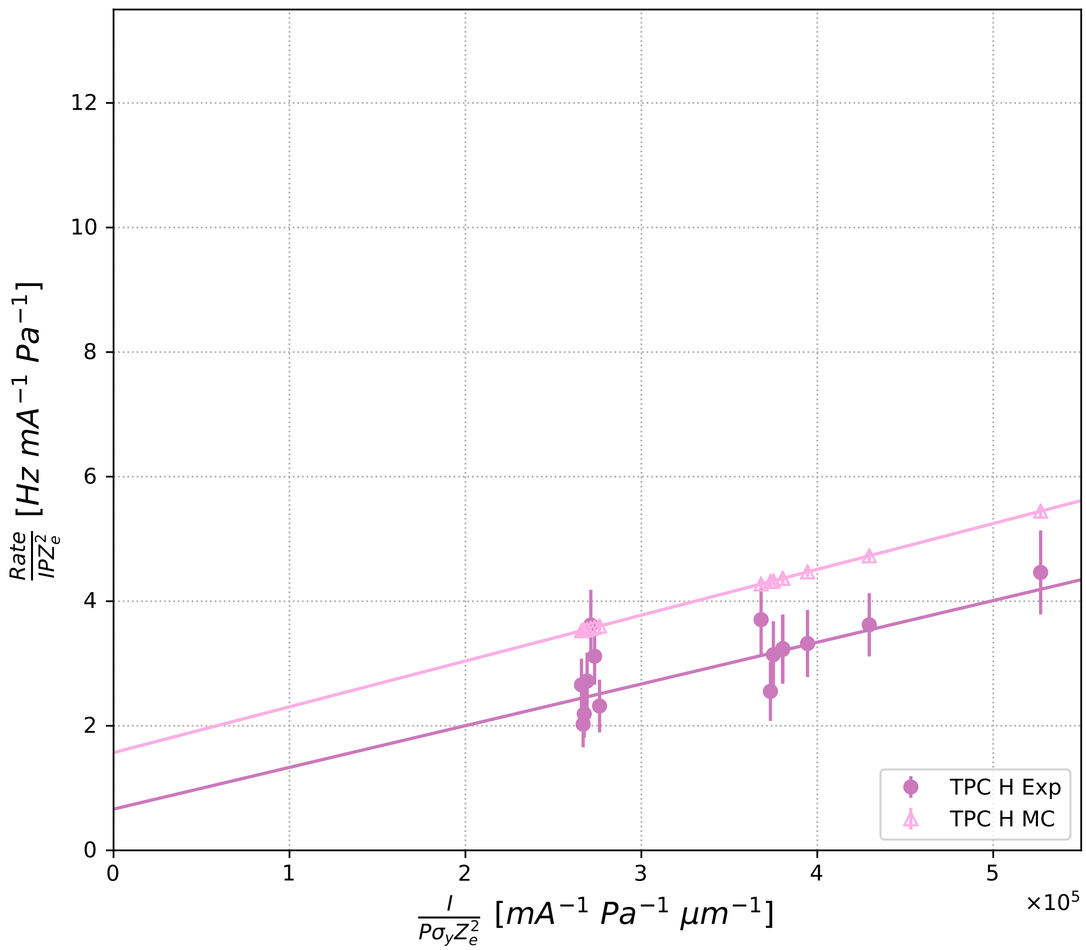

Figure 6.11: Plot of the LER beam-gas and Touschek fast neutron rates in TPC H. The dark pink circles correspond to the results from experimental data, and the light pink triangles correspond to the results from Monte Carlo.

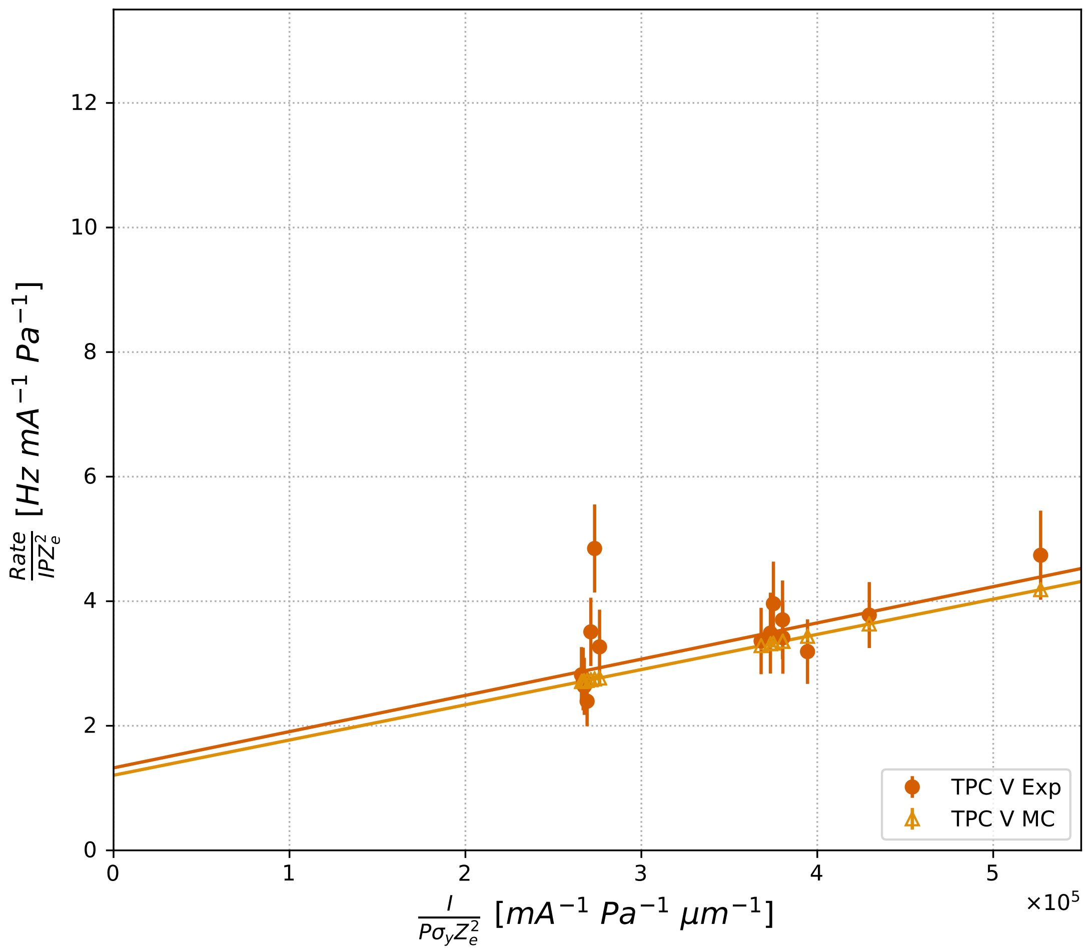

Figure 6.12: Plot of the LER beam-gas and Touschek fast neutron rates in TPC V. The light orange circles correspond to the results from experimental data, and the dark orange triangles correspond to the results from Monte Carlo.

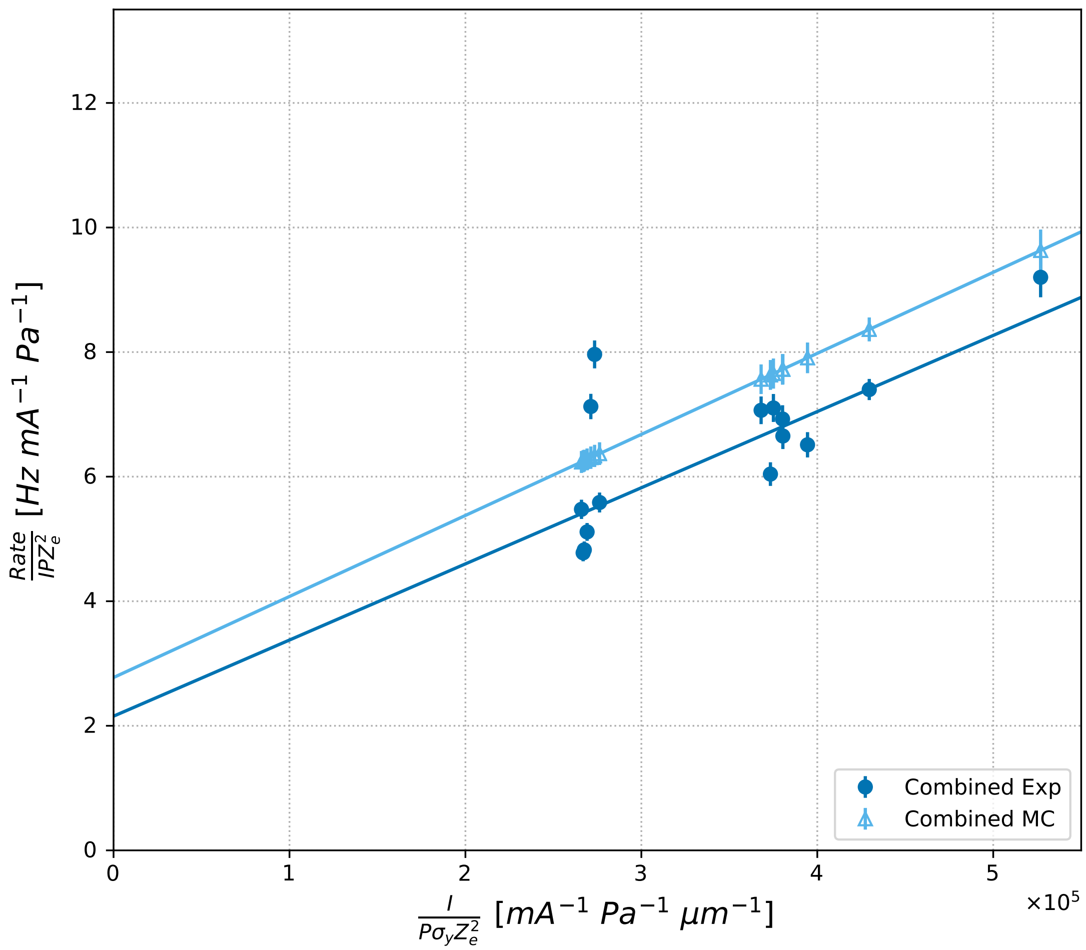

Figure 6.13: Plot of the LER beam-gas and Touschek fast neutron rates in the TPC detector system. The blue circles correspond to the results from experimental data, and the blue triangles correspond to the results from Monte Carlo.

6.9 Directional analysis of fast neutron backgrounds

Lastly, we seek to provide directional measurements of detected nuclear recoils utilizing the directional performance of the TPCs outlined in Section 5.5. First, we seek to discriminate neutron events that originate from the direction of the beam from neutron events originating elsewhere. Secondly, we will attempt to fit for the fractional contribution of Touschek and beam-gas events within the angular distribution of events in experimental data.

To do this, we utilize the 3D directionality of the TPCs demonstrated in Section 5.5. In each TPC, we select events with an axial track fit along an axis between the TPC and the beam-pipe. Utilizing the head-charge fraction (HCF) variable from Section 5.5—corresponding the fractional amount of the total detected charge in an event that is in the forward-traveling half of the recoil event—we fit for the number of events with vector directionality pointing away from the beam-pipe, referred to as *outgoing* events, as well as the number of events with vector directionality in the opposite direction, referred to as *incoming* events. The templates for these events are built from histograms of the HCF distributions of simulated outgoing and incoming events utilizing the truth information in the simulated data. Using these templates, we then fit for the yield of each template to the histogram of experimentally measured HCF distributions.

To fit for the yield of incoming and outgoing events, an assumption must be made about the angular information for each event. Since the 3D vector information that the track fitting algorithm converges to is random, we impose an "outgoing-hypothesis" such that all reconstructed events are described by vectors pointing radially outward from the beam-line in order to eliminate randomness introduced by the track reconstruction. In TPC H, this corresponds to a ϕ for all detected events such that $90^\circ < abs(\phi_{reco}) < 180^\circ$[§]. The axis connecting the IP and TPC H, or *Line-of-Sight (LoS)*, falls along the $-x$-axis, corresponding to an angle of $abs(\phi_{reco}) = 180^\circ$ and $\theta = 90^\circ$ in Belle II coordinates, shown in Figure 6.5. In TPC V, this corresponds to a ϕ for all detected events such that $-180 < \phi < 0$, with the *LoS* of TPC V falling along the $-y$-axis, corresponding to an angle of $\phi = -90^\circ$ and $\theta = 90^\circ$. We then define an event acceptance of $\pm 20^\circ$ in ϕ from the *LoS*. This corresponds of $160^\circ < abs(\phi_{reco}) < 180^\circ$ in TPC H and $-70^\circ < \phi < -110^\circ$ in TPC V. These selections and the resulting cumulative efficiencies are shown in Tables 6.4 and 6.5 for TPCs H and V, respectively, corresponding to all except the last selection in those tables applied to events

[§]We note that neither ϕ nor θ is explicitly *constrained* by the fitter. Rather, if the fitter returns a vector with *phi* outside of this range, the full vector is reversed in direction, with the resulting angular information saved.

in this analysis, which are needed to isolate helium recoils. This is done because, as shown in Section 5.5, the HCF of carbon and oxygen recoils, on average is symmetric about HCF = 0.5, which limits the effectiveness of this analysis method.

The results of these fits are shown in Figures 6.14 and 6.15 for TPCs H and V, respectively. The top plot in these Figures corresponds to using a log-likelihood fit of the HCF of reconstructed events in the simulation (black points) to the sum of two template histograms of the true outgoing and incoming HCF distributions (blue and orange, respectively). The template histograms are scaled to the fitted fractional composition of each event type as given by the log-likelihood fit. The green line shows the sum of the orange and blue histograms in each bin. In the top plots of both of these figures, the green line matches exactly with the value of the black points in all bins. This implies that fitting the Monte Carlo distributions with the truth templates, also from the Monte Carlo, works perfectly and validates our methodology. This same procedure is applied to the experimental data in the bottom plots.

The fitted fractional yields are given in Table 6.12. We find that in TPC H, the fitted incoming and outgoing fractional yields are equivalent to the prediction from Monte Carlo, within errors, at a composition of 75% outgoing to 25% incoming recoils. For TPC V, we find that there is a disagreement worth noting. The Monte Carlo also predicts 75% outgoing to 25% incoming events in TPC V, but the fits to experimental data show 50% composition of outgoing and incoming events at about 2.5σ. However, we note that TPC V has a substantially higher amount of backgrounds that are not present in TPC H nor present in the simulated data for TPC V, as seen in Section 5.4. This is noticeable when comparing Figures 5.30 and 5.31, which shows E versus L for selected recoil events in TPCs H and V, respectively. These extra background events may be contaminating the HCF distributions, possibly introducing bias to the fit presented here. The alternative explanation could be that the component of incoming neutron-induced nuclear recoils is a factor of 3 larger in experimental data, but only seen in the *vertical* plane of the SuperKEKB beam-line. A future study with higher statistics samples of experimental and simulated data, with higher statistics of electron background simulations could provide further insights into this effect.

In the next analysis, we attempt to fit distributions of the polar angle θ, specifically the distributions of $cos\theta$, in experimental data to templates obtained from simulated recoils from beam-gas and Touschek backgrounds. The angle θ for both TPCs corresponds to a location along the SuperKEKB beamline¶. For this analysis, we select outgoing helium in both

¶The TPCs have the same z-axis as the global Belle II coordinate system

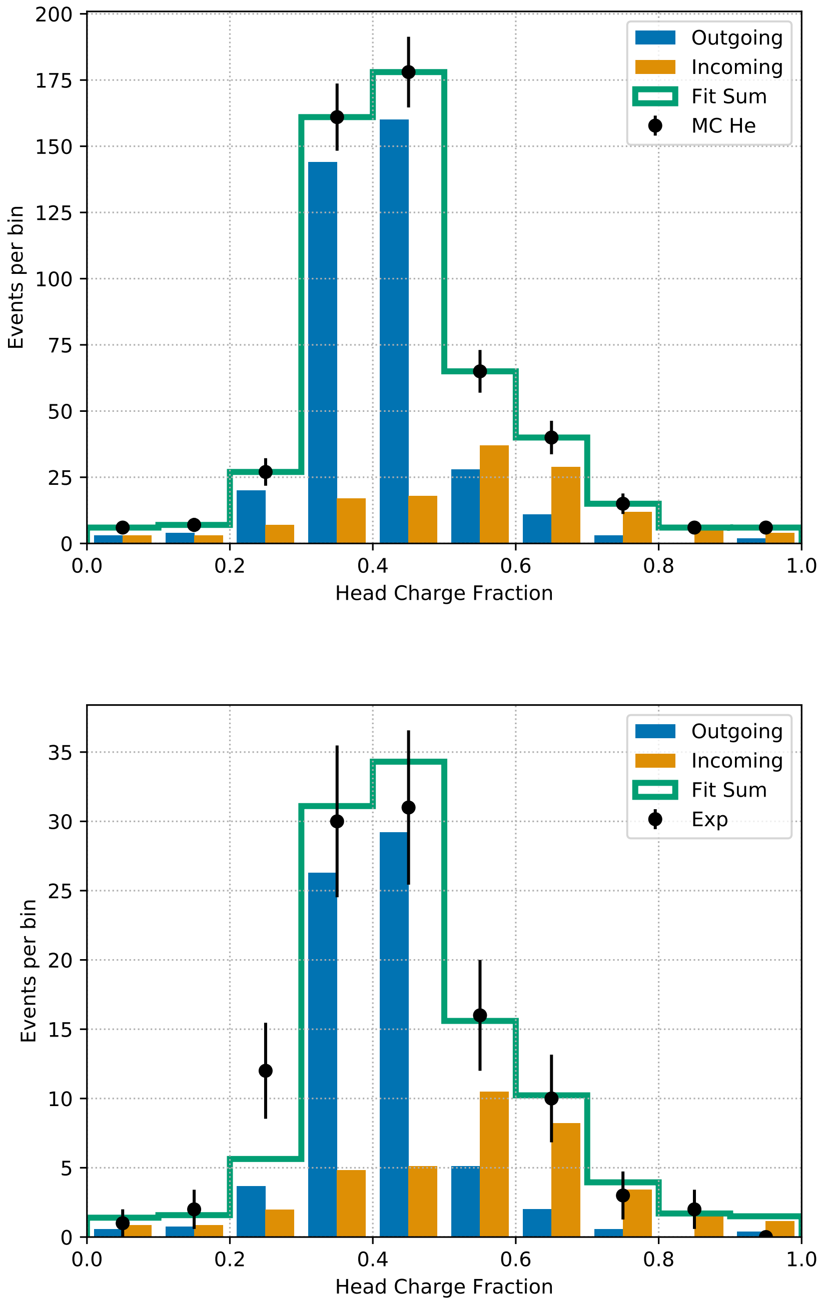

Figure 6.14: Distribution of fractional charge for simulated (top) and experimental (bottom) data in TPC H. The black points correspond to the HCF distribution of the reconstructed events in simulated and experimental data with an assumed outgoing-directionality that are within the ϕ acceptance. The blue and orange bars correspond to the yields from fitted templates of the true HCF for outgoing and incoming recoils within the ϕ acceptance, as given by the simulated data. The green line represents the sum of the two templates and the corresponding number of events of each bin.

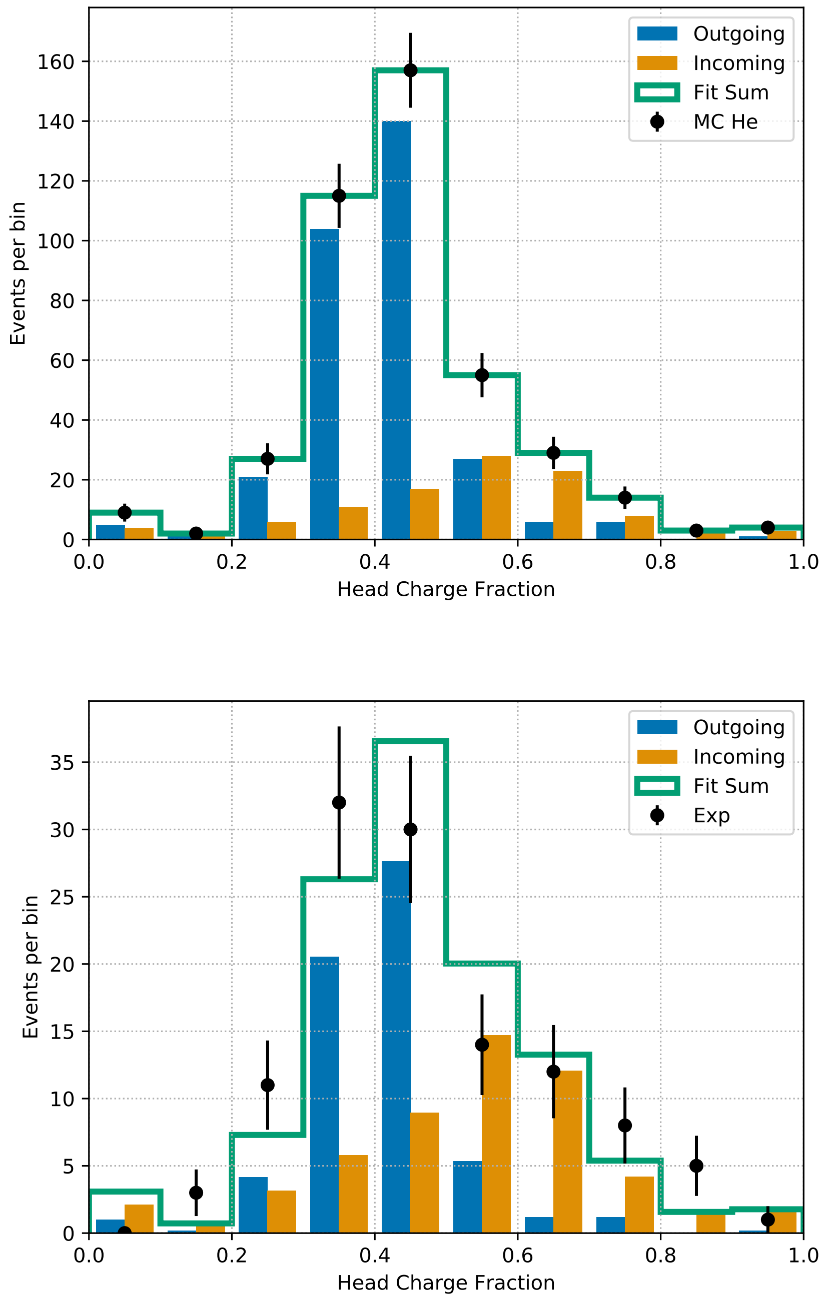

Figure 6.15: Distribution of fractional charge for true incoming and outgoing recoils in the Monte Carlo simulation of TPC V (top), which are in turn used as templates to obtain fractional yield in TPC H experimental data (bottom).

Table 6.12: Fraction of outgoing and incoming events predicted in simulation and from fitting yields to simulated and experimental data in TPC H. N_{out} corresponds to the fraction of outgoing events and N_{in} corresponds to the fraction of incoming events. Errors on the truth values correspond to the square-root of the number of events, whereas remaining errors are the errors obtained from the log-likelihood fit.

	N_{out}	N_{in}
Truth	0.73 ± 0.04	0.27 ± 0.02
MC Fit	0.73 ± 0.05	0.27 ± 0.04
Exp Fit	0.64 ± 0.10	0.36 ± 0.09

Table 6.13: Fraction of outgoing and incoming events predicted in simulation and from fitting yields to simulated and experimental data in TPC V. N_{out} corresponds to the fraction of outgoing events and N_{in} corresponds to the fraction of incoming events. Errors on the truth values correspond to the square-root of the number of events, whereas remaining errors are the errors obtained from the log-likelihood fit.

	N_{out}	N_{in}
Truth	0.75 ± 0.06	0.25 ± 0.02
MC Fit	0.75 ± 0.05	0.25 ± 0.04
Exp Fit	0.52 ± 0.09	0.47 ± 0.09

simulated and experimental data in both TPCs. As the previous analysis in Figures 6.15 and 6.14 show, outgoing events, on average have HCF < 0.5. We apply this selection, meaning that we use all selections listed in Tables 6.4 and 6.5. As can be seen, the remaining number of events after applying all of these selections is small, thereby likely introducing uncertainty introduced by Poisson statistics in the individual bins of the template histograms, which are not considered in standard fitting algorithms using histogram templates as probability density functions (PDFs). As such, we will use the *TFractionFitter* class as part of the ROOT data analysis framework [37] for this analysis.

The templates and result of the fits are shown in Figures 6.16 and 6.17 for TPCs H and V, respectively, and the fitted fractional compositions are shown in Table 6.14. Also included in Table 6.14 are interpreting the results of the heuristic analysis from Section 6.8 for direct comparison with this method of fitting $cos\theta$. As can be seen, the results of this method are consistent with the results of the heuristic method. Furthermore, both TPCs measure a higher rate in $cos\theta < 0$. This region is the in the direction of the LER beam, with respect to the IP. Considering that these data samples are taken from only the LER beam, this indicates that we are likely seeing forward showers from the LER interacting with the beam-pipe downstream of the IP, with respect to the LER beam-direction. However, these results are noticeably statistics limited, which results in large error-bars for the bin contents, which in turn affects the fitted fractional compositions. Despite that, this method demonstrates a possible decoupling of Touschek backgrounds from beam-gas backgrounds without the need for time-consuming, dedicated experimental runs where accelerator parameters are systematically varied. In principle, should this analysis method be verified, this could allow for analyzing fast-neutron backgrounds *in-situ* in symbiotic running during the later stages of Belle II operation.

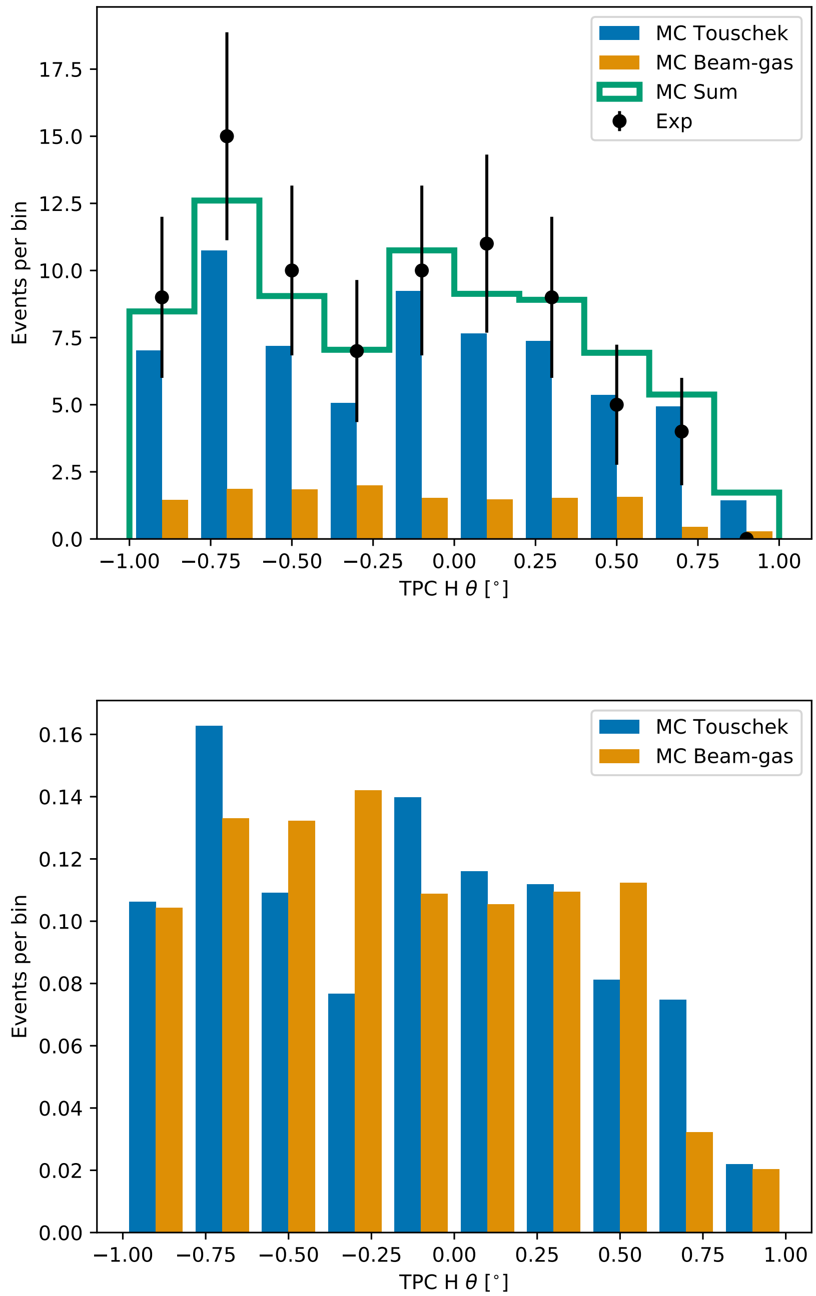

Figure 6.16: (Top) Distribution of $cos\theta$ in experimental data in TPC H (black points) with fractional yields of Touschek (blue) and beam-gas (orange) events in simulated data. The green line corresponds to the sum of the templates. This fit uses the TFractionFitter class in order to account for Poisson statistical fluctuations in individual bins in the histogram templates [37]. The bottom plot shows the normalized templates used for fitting to the black points by the TFractionFitter algorithm.

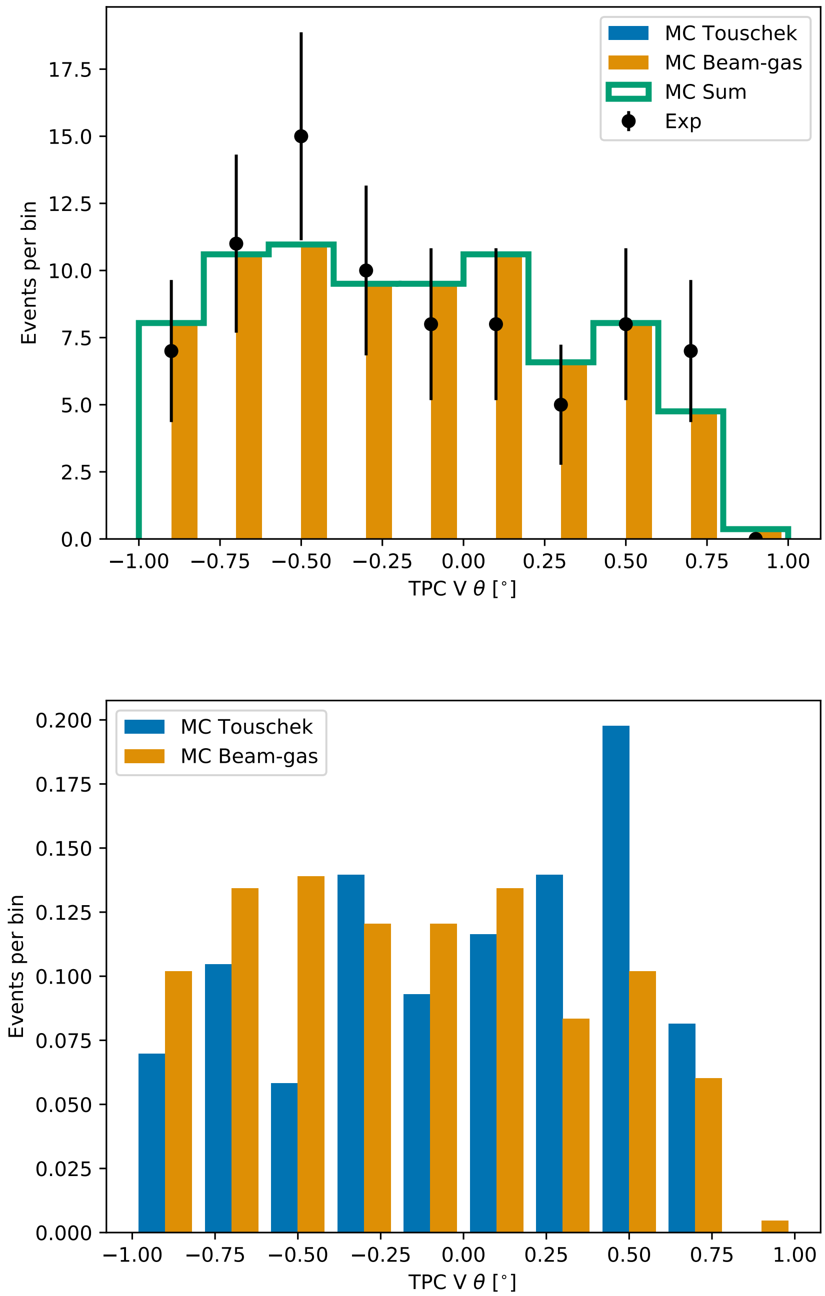

Figure 6.17: (Top) Distribution of $cos\theta$ in experimental data in TPC V (black points) with fractional yields of Touschek (blue) and beam-gas (orange) events in simulated data. The green line corresponds to the sum of the templates. This fit uses the TFractionFitter class in order to account for Poisson statistical fluctuations in individual bins in the histogram templates [37]. The bottom plot shows the normalized templates used for fitting to the black points by the TFractionFitter algorithm.

Table 6.14: Calculated yield from the fits of $cos\theta$ both TPCs, as shown in Figures 6.16 and 6.17, compared to the results of the Touschek and beam-gas backgrounds measured in each TPC using the heuristic method in Sectin 6.8. N_{bg} corresponds to the fractional composition of Touschek events, and N_T corresponds to the fractional composition of beam-gas events. The uncertainties are those returned by the fitter. We note that in the $cos\theta$ analysis, the total yields have an upper limit of the number of detected events in the data samples, whereas no such constraint was imposed on the results in the heuristic analysis.

	N_{bg}	N_T
TPC H ($cos\theta$)	$0.18\pm^{0.53}_{0.18}$	$0.83\pm^{0.16}_{0.83}$
TPC H (Heuristic)	0.21 ± 0.03	0.79 ± 0.04
TPC V ($cos\theta$)	$1.0\pm^{0.0}_{0.78}$	$0.00\pm^{0.66}_{0.00}$
TPC V (Heuristic)	0.38 ± 0.03	0.62 ± 0.03

6.10 Conclusions

In conclusion, we have provided the first measurements of the rate, energy spectra, and directional composition of nuclear recoils induced by fast neutron backgrounds during Phase 1 of SuperKEKB commissioning and we have compared those measurements to predictions from dedicated beam background simulations down to recoil energies of 50 keV. Specifically, we note the following high-level results about the Phase 1 beam-background analyses presented here:

- The HER beam-background simulations systematically underestimate the measured rates in the TPCs by as much as an order of magnitude. Longer dedicated runs in future experiments, such as Phase 2 of SuperKEKB commissioning, should be performed in order to more accurately test the HER beam-background simulations.

- The LER beam simulations systematically overestimate the measured rates in TPC H, particularly in the beam-gas component. The LER simulations accurately estimate the measured rates in TPC V.

- We have demonstrated the first application of 3D directionality of nuclear recoils using the unique measurements of the charge profile of nuclear recoils tracks.

- The recoil energy spectra in simulated and experimental data disagree at the levels of significance varying from 2–4 σ, thereby warranting further study with more data.

- The Monte Carlo prediction and the experimental measurement agree that the fractional amount of incoming events in TPC H is 25% of the total yield.

- The directional analysis shows a marginally significant disagreement between the Monte Carlo prediction and the experimental measurement of outgoing and incoming events in TPC V. We find that 50% of the yield are incoming events at a significance of $\sigma = 2.44$. While it is possible that this could be explained by higher background event rates in this TPC, this result warrants further study with more data.

- The distributions of observed events versus $cos\theta$ are consistent with simulation in both TPCs. This means that predicted neutron production points along the beam-line near the TPCs for the LER match the observed rates.

- We have presented a new analysis method for discriminating Touschek backgrounds from beam-gas backgrounds using 3D directional measurements of nuclear recoils. The results of this method, using the polar angle θ, are consistent with the results of the standard heuristic method shown in Ref. [25]. While the precision and accuracy of the results are currently limited by statistical uncertainty, validation of this analysis technique could provide a method of analyzing fast-neutron backgrounds at Belle II without the need for time-consuming machine studies requiring systematic variation of beam parameters, thereby eliminating the need to interrupt other operations.

- Alternatively, a more sophisticated analysis combining the beam-size dependence, relative rates between TPCs, and the angular information of each TPC could have the best sensitivity for analysis beam-background induced fast-neutrons at SuperKEKB.

- More generally, we presented the performance of a 3D nuclear recoil detector optimized for measuring fast-neutrons. We find excellent performance for this application down to the 50 keV level. Further tuning of target-gas choice, operational pressure, and gain settings could lead to broad application in other fields, such as direct detection of dark matter.

REFERENCES

[1] M. Tanabashi et al. "Review of Particle Physics". In: *Phys. Rev. D* 98 (3 2018), p. 030001. DOI: 10.1103/PhysRevD.98.030001. URL: https://link.aps.org/doi/10.1103/PhysRevD.98.030001.

[2] Glenn F. Knoll. *Radiation Detection and Measurement*. 4th ed. John Wiley & Sons, Inc., 2010. Chap. 2:IA, pp. 30–31.

[3] Ziegler James. *Stopping and Range of Ions in Matter*. URL: http://www.srim.org/.

[4] Glenn F. Knoll. *Radiation Detection and Measurement*. 4th ed. John Wiley & Sons, Inc., 2010. Chap. 2:IB, pp. 31–32.

[5] Helmut Paul. *Bragg Curve for Alphas in Air*. URL: https://commons.wikimedia.org/wiki/File:Bragg_Curve_for_Alphas_in_Air.png.

[6] James Ziegler. "Stopping of energetic light ions in elemental matter". In: 85 (Feb. 1999), p. 1249.

[7] G. Sciolla and C. J. Martoff. "Gaseous dark matter detectors". In: *New Journal of Physics* 11.10, 105018 (Oct. 2009), p. 105018. DOI: 10.1088/1367-2630/11/10/105018. arXiv: 0905.3675 [astro-ph.IM].

[8] J. Lindhard, M. Scharff, and H. Schiott. "Kg. Danske Vadenskab". In: *Selskab, Mat. Fys. Medd.* 33.14 (1963).

[9] Joel Holdsworth. *Negative Beta Decay*. URL: https://commons.wikimedia.org/wiki/File:Bragg_Curve_for_Alphas_in_Air.png.

[10] National Neutron Data Center. *Total neutron interaction cross section for* ^4_2He. URL: http://www.nndc.bnl.gov/sigma/getPlot.jsp?evalid=14964&mf=3&mt=1&nsub=10.

[11] Jerome I. Friedman and Henry W. Kendall. "Deep inelastic electron scattering". In: *Ann. Rev. Nucl. Part. Sci.* 22 (1972), pp. 203–254. DOI: 10.1146/annurev.ns.22.120172.001223.

[12] Glenn F. Knoll. *Radiation Detection and Measurement*. 4th ed. John Wiley & Sons, Inc., 2010. Chap. 15:IIIA1, pp. 570–571.

[13] G. Hinshaw et al. "Five-Year Wilkinson Microwave Anisotropy Probe (WMAP) Observations: Data Processing, Sky Maps, and Basic Results". In: *Astrophys. J. Suppl.* 180 (2009), pp. 225–245. DOI: 10.1088/0067-0049/180/2/225. arXiv: 0803.0732 [astro-ph].

[14] Gerard Jungman, Marc Kamionkowski, and Kim Griest. "Supersymmetric dark matter". In: *Physics Reports* 267.5 (1996), pp. 195 –373. ISSN: 0370-1573. DOI: https://doi.org/10.1016/0370-1573(95)00058-5. URL: http://www.sciencedirect.com/science/article/pii/0370157395000585.

[15] P.F. Smith and J.D. Lewin. "Dark matter detection". In: *Physics Reports* 187.5 (1990), pp. 203 –280. ISSN: 0370-1573. DOI: https://doi.org/10.1016/0370-1573(90)90081-C.

[16] Andrzej K. Drukier, Katherine Freese, and David N. Spergel. "Detecting cold dark-matter candidates". In: *Phys. Rev. D* 33 (12 1986), pp. 3495–3508. DOI: 10.1103/PhysRevD.33.3495. URL: https://link.aps.org/doi/10.1103/PhysRevD.33.3495.

[17] F. Sauli. "GEM: A new concept for electron amplification in gas detectors". In: *Nucl. Instrum. Methods Phys. Res., Sect. A* A386 (1997), pp. 531–534. DOI: 10.1016/S0168-9002(96)01172-2.

[18] I. Jaegle, S.E. Vahsen, et al. "Design and production of the BEAST micro-TPC directional neutron detectors". Publication in preparation (2018).

[19] The FE-I4B Collaboration. *The FE-I4B Integrated Circuit Guide*. 2012. URL: https://indico.cern.ch/event/261840/contributions/1594374/attachments/462649/641213/FE-I4B_V2.3.pdf.

[20] Stephen Biagi. *Magboltz, v. 10.0.1.* URL: http://consult.cern.ch/writeup/magboltz/.

[21] *USBpix — USB based readout system for ATLAS FE-I3 and FE-I4*. URL: http://icwiki.physik.uni-bonn.de/twiki/bin/view/Systems/UsbPix.

[22] T. Uchida and M. Tanaka. "Development of TCP/IP processing hardware". In: *2006 IEEE Nuclear Science Symposium Conference Record*. Vol. 3. 2006, pp. 1411–1414. DOI: 10.1109/NSSMIC.2006.354165.

[23] Glenn F. Knoll. *Radiation Detection and Measurement*. 4th ed. John Wiley & Sons, Inc., 2010. Chap. 5:IC, pp. 133–134.

[24] I. Jaegle. "Simulation of a gaseous Time Projection Chamber with a pixel ASIC readout". to be submitted to NIMA.

[25] P. M. Lewis et al. "First Measurements of Beam Backgrounds at SuperKEKB". In: (2018). arXiv: 1802.01366 [physics.ins-det].

[26] Yukiyoshi Ohnishi et al. "Accelerator design at SuperKEKB". In: *Progress of Theoretical and Experimental Physics* 2013.3 (2013), 03A011. DOI: 10.1093/ptep/pts083. eprint: /oup/backfile/content_public/journal/ptep/2013/3/10.1093/ptep/pts083/2/pts083.pdf. URL: http://dx.doi.org/10.1093/ptep/pts083.

[27] KEK. *Schematic drawing of the SuperKEKB/Belle II facility.* URL: https://www.kek.jp/ja/imagearchive/images/20180320_superkekb_002.png.

[28] T. Abe et al. *Belle II Technical Design Report.* Tech. rep. 2010. arXiv: 1011.0352 [physics.ins-det].

[29] Søren Pape Møller. *Beam-Residual Gas Interactions.* CERN Technical Report. Jan. 1999.

[30] National Synchrotron Radiation Research Center. *How a Synchrotron Light Source Works.* 2010. URL: https://www.nsrrc.org.tw/english/img/about/c-lightsource-3-1.jpg.

[31] G. C. Baldwin and G. S. Klaiber. "Photo-Fission in Heavy Elements". In: *Phys. Rev.* 71 (1 1947), pp. 3–10. DOI: 10.1103/PhysRev.71.3. URL: https://link.aps.org/doi/10.1103/PhysRev.71.3.

[32] Ph. Chomaz. "Collective excitations in nuclei". In: *Joliot-Curie School of Nuclear Physics* (1997).

[33] Xiaotian Mao, Kenneth R. Kase, and Walter R. Nelson. "Giant Dipole Resonance Neutron Yields Produced by Electrons as a Function of Target Material and Thickness". In: *Health physics* 70 (Mar. 1996), pp. 207–14.

[34] D.B. Gayther and P.D. Goode. "Neutron energy spectra and angular distributions from targets bombarded by 45 mev electrons". In: *Journal of Nuclear Energy* 21 (Sept. 1967), pp. 733–747.

[35] *Strategic Accelerator Design.* URL: http://acc-physics.kek.jp/SAD/.

[36] The GEANT4 collaboration. *Geant4 User's Guide For Application Developer.* URL: http://geant4.web.cern.ch/geant4/UserDocumentation/UsersGuides/For-\\ApplicationDeveloper/html/index.html.

[37] ROOT collaboration. *ROOT Reference Guide: TFractionFitter*. URL: https://root.cern.ch/doc/master/classTFractionFitter.html.